

POLITECNICO DI TORINO

Master degree in Energetic and Nuclear Engineering

Master Thesis

3D-printing of optimized catalyst's support geometries for syngas-synthetic chemicals conversion in fixed bed reactors



Tutors:

Prof. Federico Smeacetto

Prof. Monica Ferraris

Supervisors:

Dr. Julián Puszkiet

Dr. Marc Nuñez Eroles

Candidate:

Dario Miceli

20 March 2020

Abstract

The storage of renewable energy is an important point in the roadmap of the European energetic plan, following a development strategy of low-carbon technology. In this context the development of flexible power-to-liquid (P-to-L) and power-to-gas (P-to-G) processes for energy storage is one of the most promising solutions for the smooth transition from a driven fossil fuel society to a driven renewable sources society. In this regard, Fischer-Tropsch (FT) synthesis is used to obtain valuable chemicals from syngas (H₂/CO mixture) through a catalytic reaction. The syngas can be obtained from renewable sources such as the co-electrolysis of CO₂ + H₂O in a SOEC electrolyzer. Therefore, in this way it is possible to contribute to the CO₂ reduction and the renewable synthesis of valuable chemicals. In order to design energy conversion devices, 3D-printing as additive manufacturing (AM) technique has been recently gaining relevance. The 3D-printing technique offers more advantages respect to the classical way of production by extrusion, such as the capability to increase shape complexity while reducing waste material and manufacturing cost.

In this work, an efficient cobalt (Co) based catalyst for the Fischer-Tropsch synthesis is developed by using modelling software, called CAD (Computer-Aided-Design), 3D-printing technology and an impregnation method. As catalyst's support and 3D-printing material, α -Al₂O₃ is employed because of the low cost of this ceramic material and its positive effects on Co based catalyst for FT synthesis. Moreover, the addition of small amount of rhenium (Re) as promoter of the Co improves the availability of Co active sites.

In order to reach a trade-off between the effectiveness of the catalyst and the conditions to evaluate the catalyst in a fixed bed reactor (FBR), an eggshell Co-promoted Re-3D-printed supported α -Al₂O₃ with a diameter of about 1 mm and active catalytic layer of 20 μ m is designed. Characterization techniques such as X-ray diffraction (XRD), scanning electron microscopy (SEM), Specific Surface area (BET), Thermal programming reduction/oxidation (TPR/TPO), among the most relevant ones, are applied in order to characterize the materials during the design and synthesis process of the catalyst, after thermal treatment in different conditions as well as after the FT reaction. The designed catalyst is tested in a fixed bed reactor (FBR). Finite elements modelling (FEM) is performed to determine the temperature and pressure conditions to carry out the evaluation of the catalyst and to compare the performance of the modelled catalytic bed with the experimental results. Experimental results show that the designed eggshell Co-promoted Re/3D-printed supported α -Al₂O₃ catalyst provides a conversion of syngas of around 55 % and a selectivity toward C⁵⁺ of about 81 % at 210 °C and 20 bar with a gas hourly space velocity (GHSV) of 993 NmL/(h*g_{cat}) and syngas composition of H₂:CO ratio equal to 1.7. The experimental results are in agreement with the FEM simulations.

1 INDEX

2	Introduction	2
2.1	General overview of energy demand and CO ₂ emission trends	2
2.2	Chemical processes for the production of synthetic fuels and chemicals.....	3
2.3	Fischer-Tropsch synthesis	4
2.4	3D-printing technology in the energy sector	6
2.5	Goal and objective of the work	6
3	Experimental methods	8
3.1	3D-Printing process: production of pellets	8
3.1.1	Pellets CAD design and preparation of the 3D-printing machine.....	8
3.1.2	Cleaning process	9
3.1.3	Thermal treatments.....	10
3.2	Catalyst preparation	11
3.2.1	Mechanical Milling.....	12
3.2.2	Centrifuge of the slurry.....	14
3.2.3	Rotary vacuum dryer.....	15
3.2.4	Calcination process	15
3.3	Characterization techniques	16
3.3.1	X-ray diffraction (XRD)	16
3.3.2	Differential scanning calorimetry (DSC).....	18
3.3.3	Thermal diffusivity measurement.....	20
3.3.4	Scanning electron microscope (SEM).....	22
3.3.5	TPR/TPR-TPO	22
3.3.6	Physisorption of nitrogen (BET).....	24
3.4	Reactor setup	24
3.5	Finite Element models	26
4	Results and Discussion	28
4.1	Studies on the structural, microstructural and engineering properties of Al ₂ O ₃ (3d-printed support).....	28
4.1.1	Phase, Microstructural and morphological characterization upon the 3D-printing process.....	28
4.1.2	Determination of engineering properties	32
4.1.3	Conclusions.....	37

4.2	Tuning the geometry of a single pellet based on 3D-printed support for Co-Re promoted catalyst for FT synthesis	38
4.2.1	Printing strategy of the spherical pellets	38
4.2.2	Capabilities of the 3D-printing technique	39
4.2.3	Conclusion	42
4.3	Impregnation and characterization of Co-Re promoted- Al_2O_3 supported catalyst based on 3D-printed support	42
4.3.1	Catalyst impregnation over Al_2O_3 spherical pellets	43
4.3.2	Characterization of the Co-Re/ Al_2O_3 supported pellets	44
4.3.3	Effects of catalyst preparation, promoter and support and comparison with commercialized catalyst	50
4.3.4	Conclusions.....	54
4.4	Evaluation of the performance of the 3D-printed based catalyst.....	55
4.4.1	Optimization of the parameters in the FBR	55
4.4.2	FBR model	59
4.4.3	Model validation.....	66
4.4.4	Conclusions.....	71
5	Conclusions and Prospects	72
6	References	73

Figures list

Figure 1 – Global energy consumption and breakdown by energy since 1900 (https://yearbook.enerdata.net/total-energy/world-consumption-statistics.html)	2
Figure 2 - Annual CO ₂ emissions by world region.....	3
Figure 3 - Various pathways for conversion of renewable energy, water and greenhouse gases into synthetic fuels (endothermic and exothermic processes are marked with blue and red arrows respectively) [1]	4
Figure 4 - Paste of alumina (from Sinto 3DCERAM).....	9
Figure 5 - Debinding process	10
Figure 6 - Oven for debinding (IREC).....	10
Figure 7- Sintering process	11
Figure 8- left) comparison of the dimension with a pen; right) chamber refill with zirconia balls and Co ₃ O ₄ powder	12
Figure 9- Milling machine, Retsch MM 400	13
Figure 10 - Slurry after the Milling process	13
Figure 11 - Centrifuge machine (Eppendorf 5810 R)	14
Figure 12- Rotary vacuum dryer	15
Figure 13- oven for the calcination of the catalyst	16
Figure 14 - Bragg's law, X-ray diffraction	17
Figure 15 - XRD setup: 1) sample holder 2) X-ray tube 3) X-ray detector	17
Figure 16- DSC configuration and typical curve obtained from an analysis.....	18
Figure 17- DSC equipment	19
Figure 18- LINSEIS XFA 600.....	20
Figure 19 - Thermal diffusivity measurement	21
Figure 20 - LINSEIS software and single measurement.....	21
Figure 21 - pathway of the electrons in the SEM	22
Figure 22- typical TPR and TPO profiles	23
Figure 23 - Main elements of the reactor setup.....	25
Figure 24 - Interior of the Microactivity-Reference unit.....	25
Figure 25 - models commonly used for describing catalytic FBR [17]	27
Figure 26 - XRD of the alumina during the 3D-printing and thermal process. XRD reference card from [19].....	29
Figure 27 -SEM photo after 3D-printing.....	30
Figure 28 - SEM photo after debinding	30
Figure 29 - SEM photo after Sintering.....	30
Figure 30 - Density of alumina after each thermal process	31
Figure 31 - α -Al ₂ O ₃ density	33
Figure 32 - DSC graph of the heat flux upon the process	34
Figure 33- Specific heat capacity of α -Al ₂ O ₃	35
Figure 34 - Thermal diffusivity α -Al ₂ O ₃	36
Figure 35 - Thermal conductivity α -Al ₂ O ₃ in comparison with the database and models taking into account the porosity	37
Figure 36 - Strategy adopted to print spherical pellets	39

Figure 37 - 3D-printed sphere of d=1 mm.....	40
Figure 38- BET area of alumina spherical pellets.....	40
Figure 39 - 3D-printed sphere of d=0.3 mm.....	41
Figure 40 - 3D-printed square pellets with different holes size	41
Figure 41 - Eggshell Co-Re/Al ₂ O ₃ supported pellets	43
Figure 42- XRD of Co-Re/ α -Al ₂ O ₃ pellets after impregnation	44
Figure 43 - SEM of catalyst layer where the microstructure of the cobalt oxide and its attachment with the alumina are highlighted	45
Figure 44 - TPR analysis of Co-Re/ α -Al ₂ O ₃ pellets	45
Figure 45- XRD of Co-Re/ α -Al ₂ O ₃ pellets after TPR.....	46
Figure 46 – SEM images of the Co ₃ O ₄ layer after synthesis and metallic Co after TPR.....	47
Figure 47 - TPO measurement of Co-Re/ α -Al ₂ O ₃	47
Figure 48 – XRD of Co-Re/ α -Al ₂ O ₃ pellets after TPO	48
Figure 49 – Isothermal physisorption of Co-Re/ α -Al ₂ O ₃ to determine BET area and pore size.....	49
Figure 50 - TPR comparison between as-purchased Co ₃ O ₄ powder and after milling and drying process	50
Figure 51 - Co ₃ O ₄ particle size: a) as-purchased 24 μ m, b) after drying process 11 μ m	51
Figure 52 - Effect of the support on TPR profile	52
Figure 53 - XRD of the promoter (Re) upon the synthesis process	52
Figure 54 - TPR of catalyst with and without promoter.....	53
Figure 55 - TPR comparison with commercialized catalysts (Johnson Matthey Chemicals: https://matthey.com/en).....	54
Figure 56 - Selectivity and conversion obtained during the experiment.....	56
Figure 57 - Stability of selectivity and conversion with optimized parameters	57
Figure 58 - Stability of the CO rate with the optimized parameters	58
Figure 59 - Specimen with the liquid products of the reaction.....	58
Figure 60 - Geometry and mesh of the model (2D-axial symmetric geometry)	60
Figure 61 - temperature and heat source inside the reactor in the optimized condition	64
Figure 62 - pressure and velocity inside the reactor in the optimized condition.....	65
Figure 63 – Reactants concentration along the axial direction at r=0.....	65
Figure 64 – Products concentration along the axial direction at r=0	66
Figure 65 – comparison model-experiment changing the temperature (200-220 °C)	70
Figure 66 - comparison model-experiment changing the pressure.....	70
Figure 67 - comparison model-experiment changing the GHSV	71

Tables list

Table 1 - Fischer-Tropsch (FT) main data	5
Table 2 - Calculation of the mass of catalyst and promoter over the support after impregnation	43
Table 3 – Determination of the crystallite size of Co_3O_4 and Co°	48
Table 4 - Comparative values of catalyst with and without promoter	53
Table 5 - Results from the liquid chromatography	59
Table 6 - Kinetic parameters of the model obtained after the comparison with the experimental results	61
Table 7 – Parameters for internal diffusion limitations	67
Table 8 - Parameters for internal heat transfer limitations	68
Table 9 – Mears number parameters for external diffusion limitation	68
Table 10 - Mears number parameters for heat transfer limitations	69

2 INTRODUCTION

2.1 GENERAL OVERVIEW OF ENERGY DEMAND AND CO₂ EMISSION TRENDS

Humankind has been using fossil fuels to keep running the energy and economy systems. Therefore, global energy consumption has grown significantly during the last 30 years from about 8500 Mtoe in 1990 to 14000 Mtoe in 2018, as shown in (Figure 1).

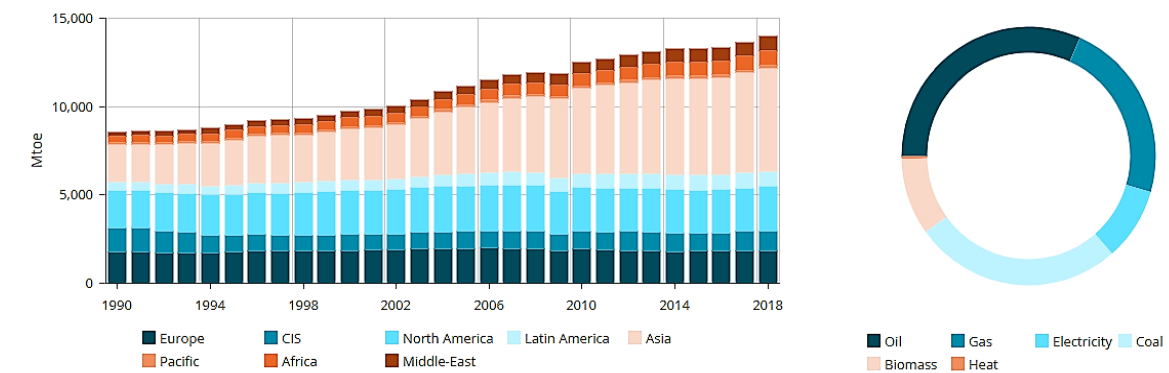


Figure 1 – Global energy consumption and breakdown by energy since 1990 (<https://yearbook.enerdata.net/total-energy/world-consumption-statistics.html>)

Nowadays the energy is mostly produced from fossil fuels that have led to a rapid increase in greenhouse gas emissions (GHG) that are important in sustaining the weather and life in the world. However, if they increase respect to the standard, they can change the equilibrium of the planet. Carbon dioxide (CO₂) is one of the most critical greenhouse gases used as an index to understand climate change and its emission has been notable increasing (Figure 2) causing the increment of the average world temperature . The consequences are glaciers melting, resulting in the increase of the level of the seas, more frequent forest fires, and others. That is why global warming is becoming a more critical problem to be addressed.

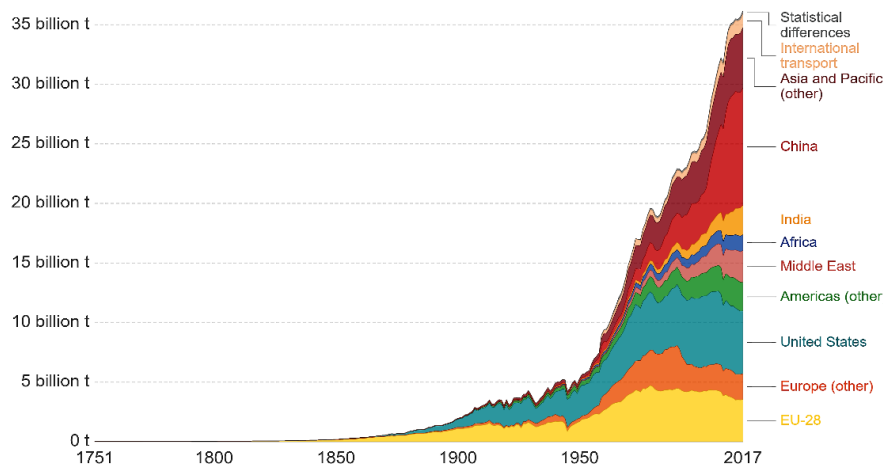


Figure 2 - Annual CO₂ emissions by world region

The production of energy vectors, such as hydrogen and synthetic fuels, from renewable sources is regarded as the best solution to the current environmental problems and the large demand for fuels. Thus, applying this approach CO₂ emissions can be reduced, and the diversification of energy vectors along with an expected reduction of the dependency on fossil fuel markets can be reached. However, this is a transition period where 26% of the total energy demand is covered by renewable sources and their availability is limited. They cannot satisfy the energy demand and, for this reason, the storage of renewable energy vectors is an important issue included in the roadmap of the European Union strategy. This strategy is in agreement with the development of low-carbon technologies. In this context, the development of flexible power-to-liquid (P-to-L) and power-to-gas (P-to-G) processes for the storage of renewable energy vectors is one of the most promising solutions for the smooth transition from a driven fossil fuels society to a driven renewable sources society.

2.2 CHEMICAL PROCESSES FOR THE PRODUCTION OF SYNTHETIC FUELS AND CHEMICALS

The possibility to directly convert carbon into synthetic fuel was discovered many years ago in Germany by Friedrich Bergius in 1913. The most important synthesis processes that have high potential in the industry field for the conversion of CO₂ and the production of valuable chemicals are summarized in (Figure 3).

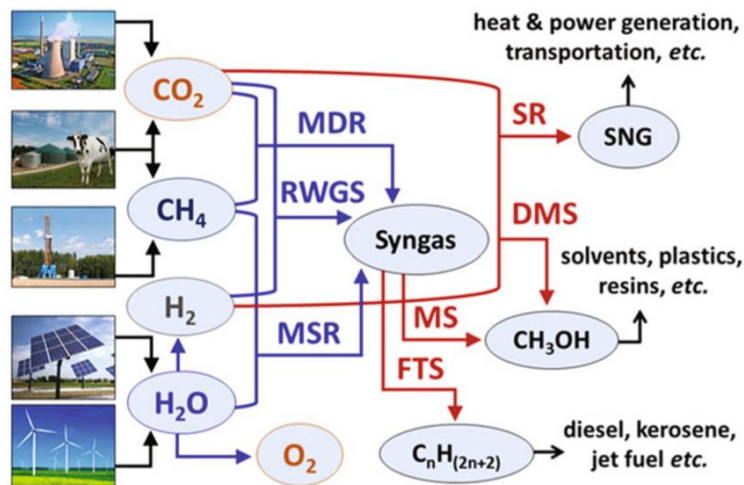


Figure 3 - Various pathways for conversion of renewable energy, water and greenhouse gases into synthetic fuels (endothermic and exothermic processes are marked with blue and red arrows respectively) [1]

During the second world war, a chemical synthesis to convert CO into valuable chemicals was developed by Franz Fischer and Hans Tropsch. Nowadays, the process is very well-known as “Fischer-Tropsch synthesis”. This kind of synthesis is known as an indirect synthesis since they don’t use CO₂ as driven source but syngas, a mixture of carbon monoxide (CO) and hydrogen (H₂). Several thermocatalytic pathways (the combination of high temperature with a heterogeneous catalyst) are available for the production of Syngas [1]. Each of them is an endothermic reaction and, because of the high stability of the CO₂, needs much energy to be converted into syngas. However, if renewable sources provide the energy, the process becomes sustainable. Thus, these powerful technologies can be used to reduce the anthropogenic CO₂, to give more value to waste steam of some processes, and to store energy in the form of renewable synthetic fuels reducing the use of non-renewable fossil fuels.

2.3 FISCHER-TROPSCH SYNTHESIS

Fischer-Tropsch (FT) synthesis is considered a key component because of its capability to provide synthetic green fuels. It involves a catalytic process through which gas, liquid and/or solid hydrocarbons are obtained from syngas (H₂/CO).

The predominant products are paraffins, olefins and alcohols provided by the following chemical reaction:

- $nCO + (2n + 1)H_2 \rightarrow C_nH_{2n+2} + nH_2O$ paraffins synthesis
- $nCO + 2nH_2 \rightarrow C_nH_{2n} + nH_2O$ olefins synthesis
- $nCO + 2nH_2 \rightarrow C_nH_{2n+1}OH + (n - 1)H_2O$ alcohols synthesis

The FT process can be divided into two main categories: high temperature (HTFT) and low temperature (LTFT) processes according to the obtained products. In (Table 1), the most important features of the HTFT and LTFT processes are described. On the one hand, the HTFT process provided light

hydrocarbons, principally CH₄, the process requires temperatures over 300 °C, and Fe is commonly used as the catalyst. On the other hand, the LTFT that leads to the production of heavy hydrocarbons (C⁵⁺), lower temperatures are needed, in general below 240 °C, and Co is the most efficient catalytic species owing to the high selectivity towards C⁵⁺ [2]. For both, HTFT and LTFT, the reactions are highly exothermic ($\Delta H = -165 \text{ kJ/mol}_{\text{CO}}$). Hence, efficient thermal management is required to avoid a decrease in the yields of products and selectivity.

Table 1 - Fischer-Tropsch (FT) main data

TYPE	TEMPERATURE [°C]	PRESSURE [bar]	REACTOR TYPE	PRODUCTION SELECTIVITY	CATALYST
HTFT	300-330	30-60	Circulating fluidized-bed reactor	Light hydrocarbons: methane	Iron (Fe)
LTFT	200-240	20-40	Fixed-bed reactor (FBR) Slurry phase reactor (SPR)	Heavy hydrocarbons: waxes, paraffins	Cobalt (Co) Iron (Fe)

Throughout several investigations, it has been reported that the proper conditions for the production of large hydrocarbon chains (C⁵⁺) is in the range of temperatures from 210 to 230 °C, pressures from 20 to 30 bar and H₂/CO ratios of about 2 [3]. It is important to mention that these conditions are highly dependent mainly on the kind of catalytic species and type of reactor.

The most considered catalysts are based on transition metal like cobalt (Co), iron (Fe), ruthenium (Ru), nickel (Ni). However, ruthenium has a high cost and low availability and nickel promotes methane formation. Given this constraints, commercialized catalysts are based on iron and cobalt.

Iron exhibits water-gas shift (WGS) activity instead of cobalt catalysts does not have this activity leading to the improved hydrocarbon chain. However, cobalt is more expensive than iron, but still a very good alternative to iron catalysts. The reason is that cobalt catalysts demonstrate activity at lower operating pressures.

Nowadays, the reactors commercially available and commonly used at laboratory scale are [4]:

- Fluidized-bed reactor
- Fixed-bed reactor (FBR)
- Slurry phase reactor (SPR)
- Circulating fluidized-bed reactor

Among them, the fixed bed reactors are the most common in large-scale chemical production because the performances are easily predicted from lab-scale. They can operate in continuous condition for a long period without degrading the catalyst. As consequence, annual costs and shutdown costs are enough reduced. Moreover, the separation of heavy wax products from the catalyst doesn't require special equipment since the liquid wax simply drops down the bed and is collected in a downstream vessel.

2.4 3D-PRINTING TECHNOLOGY IN THE ENERGY SECTOR

Nowadays, several manufacturing processes are available for the production of energy devices [5]. However, the 3D printing technology is becoming a new powerful tool in many different applications especially in the energy sector for the design and production of components such as solid oxide fuel cell, storage of hydrogen, micro-reactors, flexible solar cells, wind turbine, etc.

The huge interest in this technology is related to its capability to create custom, complex prototypes in less steps and short time with respect to the traditional manufacturing processes. 3D-printing projects are easy to modify and allow to easily simulate the final device performances before producing them. Moreover, the opportunity to control precisely the material's structure and to create lighter materials with higher performances, reduces waste material and transportation cost.

These advantages can be used in the energy sector that has to solve the problems related to global warming providing high-efficiency devices based on renewable energy, but renewable energy such as solar and wind are not continuously available due to weather related constrains. Thus, to overcome this problem the interest toward the chemical energy storage of green fuels (i.e. hydrocarbons, hydrogen, methanol) and conversion energy devices (i.e catalytic reactors for Fischer-Tropsch synthesis) has increased rapidly in the last years. Most of the components used for these applications are based on ceramics, composite and cermet and specific properties can be gained with 3D printing technology by controlling the microstructure.

During the last decade 3D-printers have been mainly developed and commercialized for polymeric and metallic structural parts. There are few printers and material available for functional and complex shaping ceramic parts and intensive research is involved finding appropriate solutions.

2.5 GOAL AND OBJECTIVE OF THE WORK

This work aims to design and optimize the catalyst for the synthesis of valuable chemicals *via* the low-temperature Fischer-Tropsch synthesis (LFT) in a fixed bed reactor (FBR). For this purpose, the idea is to use 3D-printing technology as a novel tool to produce the catalyst taking advantage of its capability to create complex shapes and reduce waste material and capital cost.

The objective of this work is the design of an eggshell catalyst based on Co as active species, promoted by Re and supported by alumina (Al_2O_3). The support should have a shape to optimize the selectivity towards C^{5+} hydrocarbons, carbon monoxide (CO) conversion no higher than 50%, efficient heat transfer properties and relatively low drop of pressure.

Computer Aided design (CAD) software is employed for the design of the support.

Material science techniques are employed to characterize our support and its properties in the temperature and pressure range of interest. Moreover, the behavior of catalytic activity is studied accordingly. Some of these techniques are here listed and then explained one by one: X-Ray Diffraction (XRD), Scanning Electron Microscopy (SEM), DSC analysis, TPR, TPO and others.

The kinetic and thermodynamic behaviour of the process in the reactor is modelling with a finite element model (FEM) using the software COMSOL Multiphysics 5.5.

The results of the model are compared with the data obtained experimentally with the aim to verify the validity of the model created and obtain the parameters that describe the behaviour of the reactor.

3 EXPERIMENTAL METHODS

3.1 3D-PRINTING PROCESS: PRODUCTION OF PELLETS

The manufacturing sector has reached successful skills with the improvement of three-dimensional printing technologies. They allow to produce pieces with complex shape and very high accuracy, not possible by typical top-down approach. Moreover, the discarded material is considerably reduced together with the capital cost and the design for manufacturing.

All these technologies follow a typical process called Additive manufacturing (AM). Starting from the design of the model using CAD software (Computer Aided Design), 3D geometries are made adding the material layer by layer. However, the way this process is done changes from one technology to another [5]. Among them, a stereolithography method based machine (SLA) was used (Ceramaker made by 3DCeram (Sinto)).

The principle of the SLA is to cure and solidify a photosensitive resins with a high ceramic load with the use of an ultraviolet (355 nm) beam produced by a semiconductor laser.

In the following paragraph the procedure for the design of the pieces, preparation of the machine and cleaning of the printed pieces are explained.

3.1.1 Pellets CAD design and preparation of the 3D-printing machine

The first step was the design of the pieces. For this purpose, **Solidworks** software was employed. It allows to create the geometry of high complexity and to do the assembly of different parts that compose a unique object. CAD design was converted to an appropriate format for the 3D-printing device.

The platform, where the pieces were printed, was cleaned with ethanol and a sticker of magnetic paper and one of white paper are put on top as adhesion surface for the print.

A paste based on alumina particles and monomers was used as 3D-printing material (Figure 4).

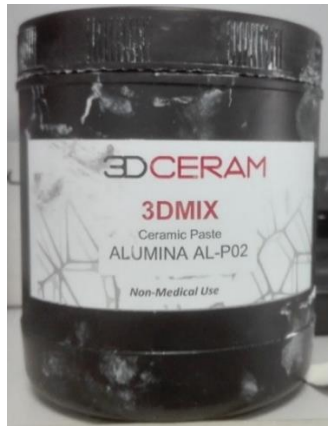


Figure 4 - Paste of alumina (from Sinto 3DCERAM)

The paste was deposited manually over a platform inside the machine. A couple of blades spread the paste and create a homogeneous layer of 50 μm (this step is repeated during the printing for the other layers).

The calibration of the laser power was performed. It is used to photopolymerize the paste. The power set depends on the starting material used as it has to be high enough for the polymerization to take place but not as much as to produce delamination of the pieces.

Once the machine is ready the program is launched and the laser starts to cure the paste.

3.1.2 Cleaning process

After printing, the platform is removed from the machine. Polymerized pieces need to be separated from the uncured paste.

Several steps are applied:

1. The pieces, attached to the platform, are carefully removed. Not all the pieces are able to survive this process due to their extreme fragility. For this reason, more pieces are printed than necessary.
2. They are immersed in a solvent based cleaning solution (ceracleaner from 3d Ceram) for 1 hour. After the use of a brush and paper, the pieces start to show their geometry but they are not ready for the thermal treatments.
3. Another solvent solution is prepared, using 20% Toluene and 80% Heptane. The Toluene is a powerful solvent but, in addition to effectively cleaning the piece, causes the formation of cracks due its fast drying. The addition of Heptane helps to slow down the drying speed.
4. The pieces are immersed in this solution and introduced into the ultrasonic cleaner for 15 minutes. The ultrasounds promote the scrolling of the not cured paste and helps to clean the inner parts.

- The last step consists on a second wash with the ceracleaner and drying the pieces carefully with paper.

3.1.3 Thermal treatments

The printed pellets do not represent the final material. They are structurally made of a polymer with a high load of non-connected ceramic particles.

Two thermal treatments are applied to eliminate the polymer, connect the ceramic particles to form a solid piece and improve the thermo-mechanical properties:

- DEBINDING
- SINTERING

The **DEBINDING** has the aim to vaporize and separate the polymeric part (called binder) of the printed material from the alumina (Figure 5). The evaporation leaves some vacuum spaces inside the material and a reduction of the global density occur. The process was done inside the following oven (Figure 6).

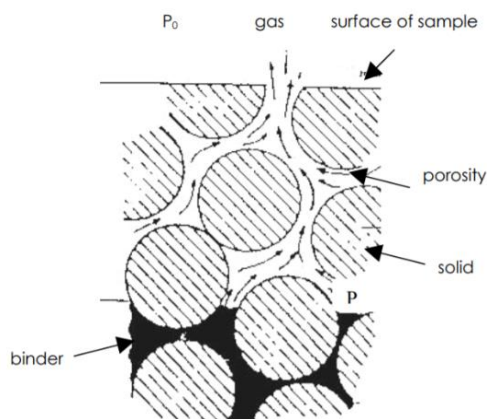


Figure 5 - Debinding process



Figure 6 - Oven for debinding (IREC)

The firing of the pellets involves a temperature increase with a low ramp to allow the binder to vaporize and get out of the sample without damaging it and causing cracks due to its expansion.

During this part of the process, a flow of inert gas was used to prevent vaporized polymers from burning. A very slow ramp from room temperature to a temperature near 1000 °C under N_2 and then synthetic air (SA) flow was programmed. Gas composition was switched gradually from N_2 to SA to avoid bubbles of organic compounds.

After the process, the density is lower, and the sample appears more porous.

The next step of the thermal treatment was the **SINTERING**. It is a process done at a high temperature below the melting point of the material for a certain time inside an oven. In this study, the samples were put in the oven for 90 minutes over 1000 °C. The condition created in the oven allows the growth of the material grains and the reduction of the pore size. The grains merge to each other and form a bigger structures with small pores. The grains merge to each other and form a bigger structures with

small pores (Figure 7). The Sintering allows to obtain material with high density and good thermal and mechanical properties.

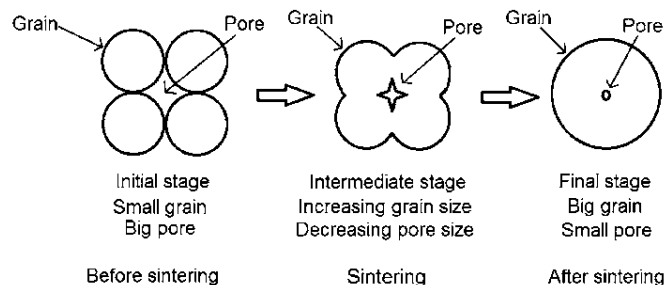


Figure 7- Sintering process

3.2 CATALYST PREPARATION

The catalyst plays a crucial role in Fischer-Tropsch synthesis. When syngas reacts, different reactions can occur and the role of the catalyst is to increase the selectivity of the interesting products (2.3).

A good Fischer–Tropsch catalyst needs high hydrogenation activity in order to catalyze the hydrogenation of CO to higher hydrocarbons. The catalyzers with this ability are the transition metal of the fourth group of the periodic table: iron (Fe), cobalt (Co), nickel (Ni) and ruthenium (Ru). However, ruthenium has a high cost and low availability and nickel favours more the production of methane. Thus, the commercialized catalysts for FT process are iron and cobalt. Between the two catalysts the choice for this study was **cobalt (Co)** that, respect to iron, shows low water-gas shift (WGS) activity and higher CO conversion and selectivity of C^{5+} [6]. Furthermore, a small quantity of a promoter is added to favour the dispersion of the cobalt particles during the preparation of the slurry and to promote the reduction of the cobalt oxide (Co_3O_4) to metal cobalt. The most used promoters for this purpose are rhenium, platinum or ruthenium. The choice for this study was **rhenium (Re)** which is reported in many papers for its high capability to improve the performance of Co/Al_2O_3 catalyst [7].

The impregnation of the catalyst over the support of alumina follows a precise list of steps that will give specific characteristics to the cobalt. Taking inspiration from the preparation proposed in the patent that describes the preparation of iron-based catalyst [8], the recipe has been adapted:

- 1) Mechanical milling Co-precursor in water for 90 min at 25 Hz
- 2) Centrifuging the slurry to separate the beads + washing: 2 times at 4000 Hz for 10 min
- 3) Rotary vacuum dryer for 2 h at 50 °C and 140 mbar
- 4) Calcination at 400 °C for 5 h in air

During each pass a quantity of catalyst was lost. This is why, in general, the production was done in excess.

3.2.1 Mechanical Milling

The first step for the impregnation of the catalyst over the support is the Milling process. The Sigma-Aldrich provides cobalt oxide (III) (Co_3O_4) in the form of powders [9].

The Co_3O_4 was mixed into the milling chamber with distillate water and balls of zirconia ($d = 0.7 \text{ mm}$). The zirconia balls allow good mixing and reduce the size of the grains. The amount needed for each ingredient was calculated taking into account the volume percentage between water and cobalt oxide and the volume of the chamber:

- 80% distilled H_2O – 20% Co_3O_4 powder
- Weight of zirconia balls = $10 \times (\text{weight of the } \text{Co}_3\text{O}_4 \text{ powder})$

The internal volume of the chamber was 25 ml. The three ingredients were weighted in order to refill 3/4 of the total volume permitting a good degree of blending. The density of the water at ambient conditions was considered to be 1 g/cm^3 . The bulk density of the zirconia balls (3.7 g/cm^3) and the apparent density of the Co_3O_4 powder (6.11 g/cm^3) were taken from the datasheet [9] [10]. So, the quantity of each compound is calculated:

- 8 g of H_2O
- 2 g of Co_3O_4
- 20 g of zirconia balls ($d = 0.7 \text{ mm}$)

The chamber is made of a heavy metal and it is internal covered by a layer of zirconia to avoid contamination and possible reaction with the metal (Figure 8).



Figure 8- left) comparison of the dimension with a pen; right) chamber refill with zirconia balls and Co_3O_4 powder

The filled chamber was inserted in the milling machine to mix the ingredients. The milling machine is composed of two arms, where it is possible to put two chambers at the same time (Figure 9).



Figure 9- Milling machine, Retsch MM 400

In order to balance the system, it is usually convenient to put two chambers: one with the solution to be mixed and the other with an empty milling chamber or filled with water until reaching the weight of the chamber containing the sample.

The arms are able to move the chambers at the frequency set and the wide range of the machine ($f = 0.3 - 25.0$ Hz) permit a certain freedom in the choice.

In this study, the frequency chosen was 25 Hz for a time of 90 min to ensure a good degree of blending and uniformity.

The slurry of water and cobalt oxide (Figure 10), obtained after the process, has to be separated from the zirconia balls and the centrifuge machine was used for this purpose.



Figure 10 - Slurry after the Milling process

3.2.2 Centrifuge of the slurry

The slurry obtained after the Milling process was separated from the zirconia balls in the centrifuge machine (Figure 11).



Figure 11 - Centrifuge machine (Eppendorf 5810 R)

The rotation is the fundamental principle of this equipment. Thanks to the different density of the compound in the solution the centrifugal force permits the separation of the slurry from the balls.

The parameters that enable to regulate the process are the angular velocity (ω), the time and the temperature. The following value were used:

- $\omega = 4000$ rpm
- time = 10 min
- $T = 23$ °C

The process was carried out more than one time until the zirconia balls become almost completely clean. Each time the slurry was recovered and inserted into a particular glass ampoule for the next step in the Rotary vacuum dryer.

3.2.3 Rotary vacuum dryer

The Co-slurry produced was dried and stuck to the surface of the support. The slurry and the alumina supports were placed inside a glass ampoule which can be inserted into the **Rotary vacuum dryer** (Figure 12).



Figure 12- Rotary vacuum dryer

The ampoule was located inside a tank with water that was heated at 70 °C to promote the evaporation process of the water.

The arm, to which the ampoule was attached, rotates the ampoule at the rotation velocity of 30 rpm. In addition, a pump creates a vacuum system of about 140 mbar and allows the evaporation at a temperature of 50 °C. The evaporated water is condensed by a spiral-shaped heat exchanger and collected in a second ampoule. The evaporating water can carry out catalyst particles with it. This is a negative effect of the process because a considerable amount of cobalt is lost.

3.2.4 Calcination process

The calcination is the last step and is usually done to stabilize the physical and chemical properties of the catalyst over the support and to eliminate all the impurities coming from the other processes. The starting material is usually an unstable metal salt (nitrates, carbonates, chlorides, etc ...) that during the calcination is decomposed into metal oxide. In this study the precursor is already in the form of metal oxide. Thus, the aim is to obtain a mechanically and thermodynamically stable macrostructure using a temperature slightly higher than the catalyst operating temperature.

The impregnated pieces, coming from the rotary vacuum dryer, were heated up inside an oven (Figure 13) with a ramp of 5 °C/min until reaching the temperature of 400 °C and then are left there at this temperature for 4 hours in air condition.



Figure 13- oven for the calcination of the catalyst

3.3 CHARACTERIZATION TECHNIQUES

In this section, techniques used for the characterization of the phase composition, structural, microstructural and thermal properties of the raw materials, 3D-printing produced materials and synthesized catalysts are first described. Then, the experimental set up for the investigations on the FT reaction is also outline. Finally, the software and conditions for the finite element modelling (FEM) study are reported.

3.3.1 X-ray diffraction (XRD)

X-ray diffraction (XRD) is an experimental technique that allows determining crystalline phases and crystalline size.

X-rays are high-energy photons with a wavelength between 10^{-3} and 10^1 nm, below the atomic distance of most materials we used in this work. Thanks to this characteristic they can diffract a X-ray beam into specific direction and produce a fingerprint of the analyzed material.

When the X-rays are diffracted from the sample, they can produce constructive or destructive interference. The physics behind this method is the **Bragg's law** (Figure 14).

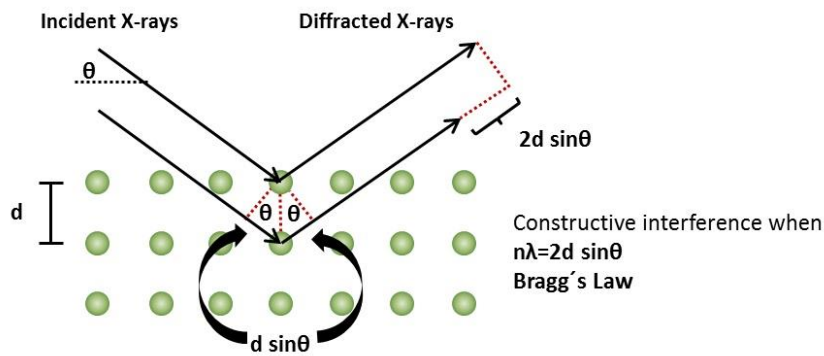


Figure 14 - Bragg's law, X-ray diffraction

Where “*n*” is the order of diffraction, “*λ*” the wavelength of the incident beam, “*d*” the lattice spacing and “*θ*” the angle of the diffracted beam. Constructive interference occurs only if the path difference (given by $2d \sin\theta$) is a multiple ($n=1,2, \dots$) of the used wavelength of the X-ray beam. Since the wavelength in XRD experiments is known and the angles at which constructive interference occurs are measured, the Bragg equation enables the determination of the distance between the lattice planes of the material.

The **diffractometer** is the instrument that allow to measure the intensity of the diffracted beam changing the incident angle between the beam and the surface of the sample. It is composed of three basic elements: a X-ray tube, a sample holder, and a X-ray detector (Figure 15).

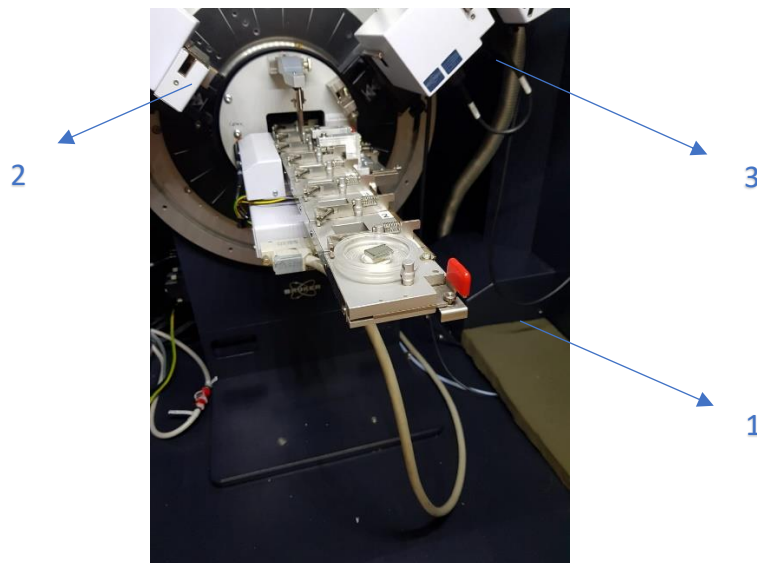


Figure 15 - XRD setup: 1) sample holder 2) X-ray tube 3) X-ray detector

The X-ray tube has the aim to produce the X-ray beam that is directed towards the sample (located in the sample holder). The beam passes through the material and is diffracted.

The X-ray detector collects the diffracted beams and by measuring the intensities of these diffracted beams at different angles, it produces a 2D graph (called **diffractogram**) with the angle 2θ on the x-axis and intensity of the beam on the y-axis.

With the peak position a qualitative phase analysis can be investigated. Based on the peak intensity, information about crystal structure (atomic positions, temperature factor, occupancy) as well as texture and quantitative phase analyses can be obtained. Finally, the peak shape gives information about the crystalline grain size of the sample making a calculation with the **Scherrer equation** [11]:

$$d_{hkl} = \frac{57.3 * K * \lambda}{B_{hkl} * \cos\theta} \quad (3.1)$$

where:

- **57.3** is a conversion factor from radians to degree;
- **d_{hkl}** is the mean grain size;
- **K** is a dimensionless shape factor. Its value is usually around 0.9;
- **λ** is the X-ray wavelength;
- **B_{hkl}** is the pure observed full width at half maximum of a diffraction peak (FWHM);
- **θ** is the Bragg angle where the pick investigated is located.

The observed FWHM was taken as the pure width since the crystalline size was taken as a comparative value.

XRD analyses were performed in a Bruker device with a Bragg-Brentano theta configuration: $\text{CuK}\alpha$ of 1.5406 Å, 40 mA and 40 kV, and polymer as well as low background sample holders. The samples were measured from 10° to 90° of two 2θ with a step of 0.02° per second under room atmosphere. The determination of the crystallite size was done with the following plane families: (311) / 2θ=36.9° for Co_3O_4 , (111) / 2θ=44° for metal Co.

3.3.2 Differential scanning calorimetry (DSC)

DSC is a thermo analytical technique in which the difference of the amount of heat to increase the temperature of a sample and a reference is measured as a function of the temperature. The DSC measurements are carried out under certain heating conditions, i.e. heating ramp as well as isothermal conditions. As seen in (Figure 16), the signals of the heat difference between the sample and the reference (heat flow) are recorded as a function of temperature (and also time).

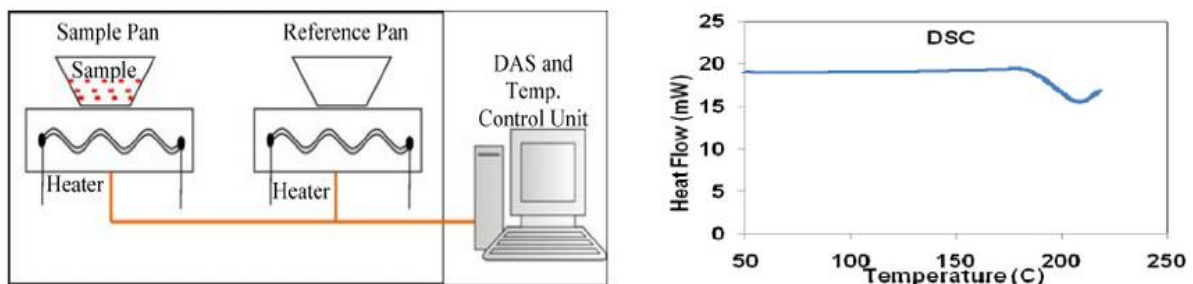


Figure 16- DSC configuration and typical curve obtained from an analysis.

The DSC technique was applied to determine the heat capacity at a constant pressure of the 3D-printed alumina material. The following device (brand: Setaram; model: Sensys evo) was used (Figure 17).



Figure 17- DSC equipment

A sample of 78.12 mg was put in an alumina crucible. As a reference, an empty alumina crucible was utilized. For this purpose, the **linear ramp method** was applied [12]. Before starting the ramp, a short isothermal period is applied to achieve the same steady state condition.

The sample and reference were heated up at 5 °C/min under He flow of 10 ml/min from room temperature to 300 °C. A blank measurement with sample and reference alumina pans empty was done in order to subtract the heat flow of the material of the sample holder.

The isobaric heat capacity is the ratio between the heat energy transferred to the material ΔQ and the temperature variation ΔT caused by this heat energy:

$$C_p = \left. \frac{\Delta Q}{\Delta T} \right|_p \quad \left[\frac{J}{K} \right] \quad (3.2)$$

The heat flux Φ is equal to the heat derivative over time t :

$$\Phi = \frac{dQ}{dt} \Rightarrow \int_{t_{start}}^{t_{end}} dQ = \int_{t_{start}}^{t_{end}} \Phi * dt \Rightarrow \Delta Q = \Phi * \Delta t \quad (3.3)$$

And the heating rate β , fixed as constant value, is defined as the variation of the temperature T over the time t :

$$\beta = \frac{dT}{dt} \Rightarrow \int_{t_{start}}^{t_{end}} dT = \int_{t_{start}}^{t_{end}} \beta * dt \Rightarrow \Delta T = \beta * \Delta t \quad (3.4)$$

By replacing the equation of heat (3.3) and temperature (3.4) within the equation of heat capacity (3.2), the following equation is obtained:

$$C_p = \frac{\Phi}{\beta} \quad \left[\frac{J}{K} \right] \quad (3.5)$$

Moreover, in order to eliminate the possible systematic errors of the machine, the heat flux of the blank/reference material Φ_b has to be subtracted from the one of the alumina sample. It is also necessary to divide the heat capacity by the mass of the sample m_s in order to have the value of the **specific heat capacity**:

$$c_p = \frac{\Phi_s - \Phi_b}{\beta * m_s} \left[\frac{J}{kg * K} \right] \quad (3.6)$$

3.3.3 Thermal diffusivity measurement

The *thermal diffusivity* (α) describes how quickly a material reacts to a temperature change and its value is fundamental for the calculation of the thermal conductivity. The useful device for the determination of the thermal diffusivity is the LINSEIS XFA 600 (Figure 19).

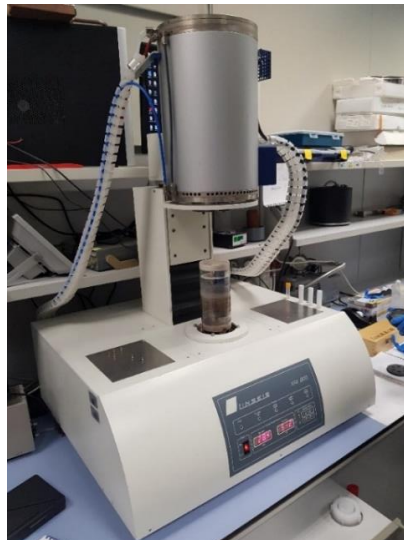


Figure 18- LINSEIS XFA 600

The sample is positioned in a special sample holder in which there are constraints for the size of the piece that can be inserted, pieces of small dimension (square base of 1 cm side) with a thickness in the range of 0.1 - 3 mm. The size constraint is specially made to ensure a more accurate measurement. A furnace takes care of the temperature control allowing the regulation and the possibility to obtain diffusivity values at different temperatures. The measurement is done under vacuum condition to avoid the scattering of the pulse with the air and the deviation of the device from the right value. A power source provides a pulse of energy that irradiate the back side of the sample, passes through it and is detected in the IR-detector producing a signal (Figure 19).

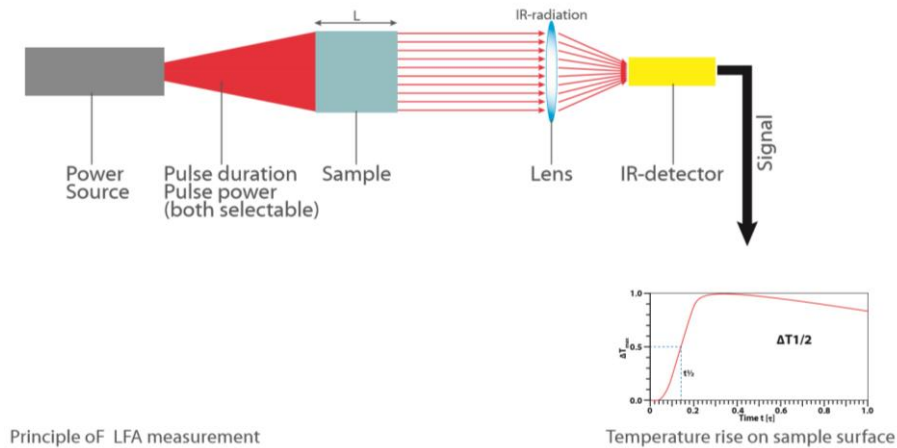


Figure 19 - Thermal diffusivity measurement

The signal is analyzed and fitted with the use of the software provided by the LINSEIS (Figure 20) and It is found the value of the diffusivity corresponding to the temperature applied.

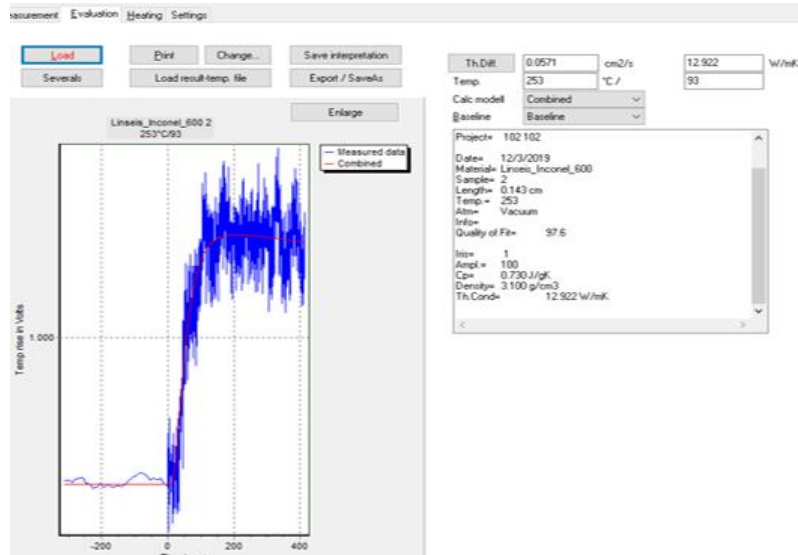


Figure 20 - LINSEIS software and single measurement

The program takes into account the parameter on the curve and the following formula:

$$\alpha = 0.13879 \cdot \frac{L^2}{t_{1/2}} \quad (3.7)$$

where α is the thermal diffusivity, L is the thickness of the sample, $t_{1/2}$ is the time needed to reach half of the maximum temperature rise.

The measurement is programmed for different temperatures until a series of points are obtained on which a trend can be constructed. Sometimes sample with a high value of emissivity or absorptivity has to be covered with a thickness of graphite because it increases the absorption of the energy coming from the laser. This is the case of the material used in this work (Al_2O_3).

3.3.4 Scanning electron microscope (SEM)

The *scanning electron microscope* (SEM) is a powerful technique discovered by *Manfred von Ardenne* that allows seeing the surface of a material down to the nanometric scale. The machine works on the principle of scattering of electrons on the surface of a sample.

The sample is positioned in a sample holder and inserted inside the chamber of the machine where the vacuum is created to prevent the distortion of the measurement due to the scattering of the electron with the air or other volatile particles.

A source provides focused electrons beam on the surface of the sample. They interact with the atoms, some pass through the sample and others are scattered and reflected by the surface in the form of secondary electrons, back-scattered electrons, Auger electrons and X-rays (Figure 21).

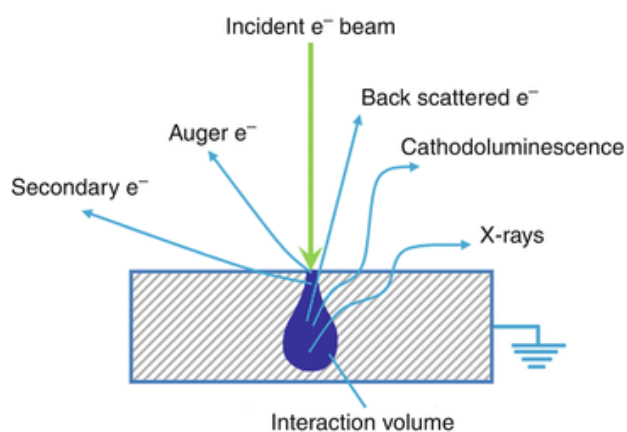


Figure 21 - pathway of the electrons in the SEM

The electron beam scans the object in a raster scan pattern making side by side. Secondary electrons and back-scattered electrons are the ones detected and processed in the SEM to produce the 3D-image.

Due to the high energy of the electron, the material needs a high electronic conductivity because, as the contrary effect, could happen, the piece collects charge causing scanning faults. In order to prevent this effect, the electronic conductivity of non-conductive materials is increased, sputtering a thin coating of a metal on the surface (gold, platinum, graphite, etc.). The alumina, used in this study as support of the catalyst, is an electrical insulator and there was the necessity to sputter the surface with gold.

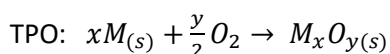
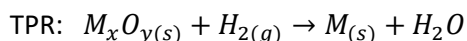
3.3.5 TPR/TPR-TPO

The *temperature programming reduction* (TPR) and *oxidation* (TPO) are techniques used in the characterization of the solid material, especially metal oxide. Transition metal oxides present

interesting redox properties for application in catalysis because of their multiple stable state of oxidation. **TPR technique** is based on the reducibility of the metal oxide when a flow of gas, in general hydrogen, is directed on its surface meanwhile the temperature of the system changes in a predetermined and controlled way, usually a linear temperature ramp is applied. **TPO technique** investigates the oxidation behaviour of the reduced metal through a flow of oxygen.

The parameters set in the analysis are the sample mass, the temperature increasing rate and the flow rate of the reactive gas.

The following reductions are involved:



The TPR/TPO apparatus is composed of three principle parts:

1. Gas line for pre-treatments and analysis
2. Reactor electrically controlled
3. Detector for the valuation of the gas consumed (TCD detector).

The metal oxide is dispersed upon a surface (like the support of the catalyst) and inserted inside the reactor. A reducing/oxidizing gas mixture, for example hydrogen (H₂)/oxygen (O₂), is made to flow across the catalyst under gradually increasing the thermal conditions. The detector produces a signal in voltage (TCD) proportionally to the rate of hydrogen/oxygen consumption that depend on the temperature (Figure 22).

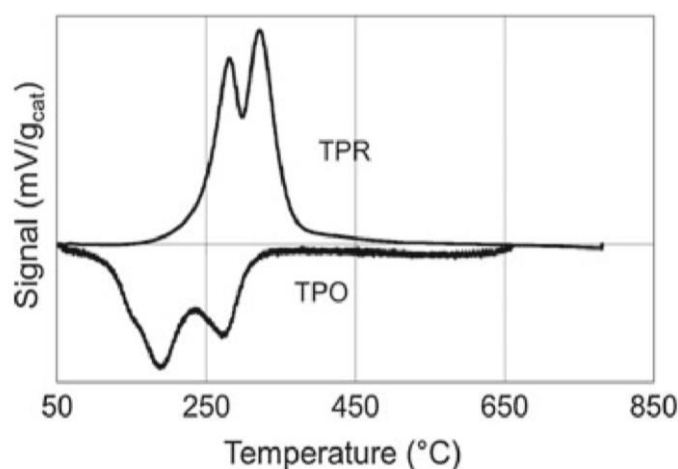


Figure 22- typical TPR and TPO profiles

From the TPR/TPO profiles peaks, the information about the temperature at which the maximum rate of reduction occurs is obtained. The amount of gas consumed to reduces/oxides the catalyst provides information about the degree of reduction/oxidation.

Moreover, if the analysis is performed for a catalyst combined with a support is possible to compare the behaviour or the graph obtained with and without the support to know the effect of the support in the redox reaction.

In this work, the TPR was applied to understand the temperature of reduction of the cobalt oxide into metal cobalt and the role of the support and the promoter. The measurement was performed with a

flow of 50 cm³/min (in STC) with 10% H₂ and 90% Ar. The temperature was kept constant, 25 °C, for the first 30 min and then a ramp of 10 °C/min started until reaching 800 °C in order to obtain results in a broad temperature range.

3.3.6 Physisorption of nitrogen (BET)

The physical isotherm adsorption and consecutively desorption of inert gas molecules (usually nitrogen) on the surface of a solid gives the possibility to calculate the specific surface area, pore size, pore volume and distribution of pores of catalysts.

The BET method, discovered by Brunauer, Emmet and Teller [13] [14], is an accredited way analysis to calculate the specific surface area and it is based on the Langmuir theory [15]. The resulting BET equation is:

$$\frac{1}{v \cdot \left[\left(\frac{p_0}{p} \right) - 1 \right]} = \frac{c - 1}{v_m \cdot c} \cdot \left(\frac{p}{p_0} \right) + \frac{1}{v_m \cdot c} \quad (3.8)$$

where v is the volume of adsorbed gas, v_m is the volume of the adsorbed when a monolayer is formed, p and p_0 are the equilibrium and the saturated pressure of the gas adsorbed in isotherm condition and c is the BET constant that depends on the heat of adsorption of the adsorbed gas over the surface. The analysis provides a trend of the amount of gas adsorbed n_m versus the relative pressure p/p_0 and the specific surface area is expressed as:

$$S_{BET} = \frac{v_m \cdot N_s}{V \cdot a_m} \quad (3.9)$$

where N_s is the Avogadro's number, V is the molar volume of the adsorbate gas, a_m is the mass of the sample.

Pore size, pore volume and distribution of pores of catalysts are obtained from the desorption isotherms applying the method of Barret, Joyner and Halenda (BJH) [16].

In this work the analysis was for the support with and without catalyst to understand the contribution of the catalyst. The analysis was carried out under N₂ adsorption/desorption isotherms at its boiling temperature (T=77) and equilibrium pressure of 780 mmHg using a Micromeritics Tristar-II.

3.4 REACTOR SETUP

The performance of the catalyst was evaluated in a fixed bed tubular reactor (brand: PID Eng&Tech). The main element of the setup (Figure 23) is the Microactivity-Reference unit coupled with a system of local control and another of remote control via PC, used to collect the experimental data.



Figure 23 - Main elements of the reactor setup

The reactor and the other components are located inside the Microactivity-Reference unit (Figure 24). The system consists of a fixed-bed tubular reactor, with the catalyst bed placed inside upon a porous plate. The reactant mixture (60 % syngas, 40% N₂) is fed through the upper part of the reactor and the reaction products are obtained through the lower part. A thermocouple, type K (encased in a 1.5 mm diameter Inconel sheath), is inserted through the upper part and is in contact with the catalyst bed. This allows reading reaction temperatures with comeback times in milliseconds. The reactor is located inside a furnace where the temperature and the pressure are kept constant.

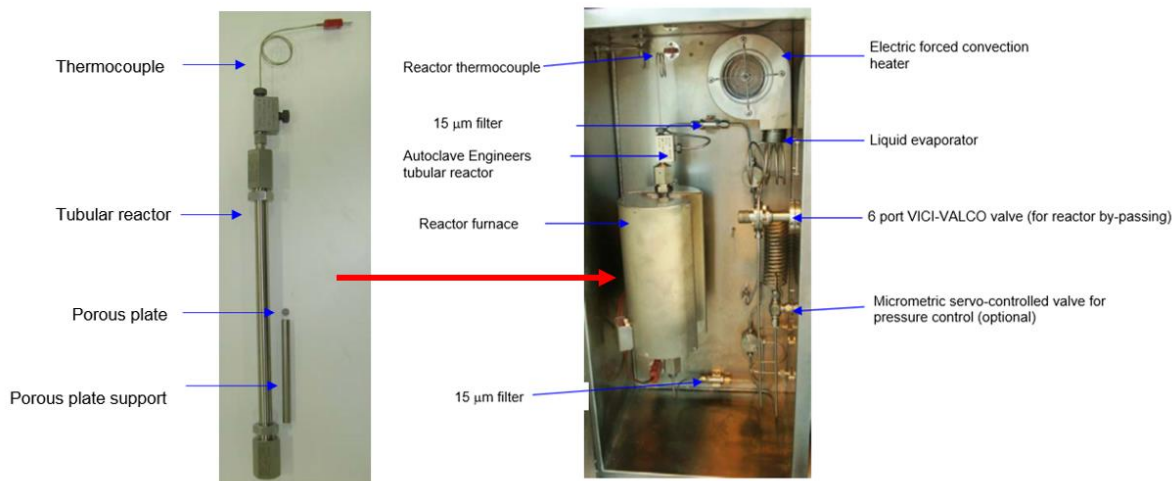


Figure 24 - Interior of the Microactivity-Reference unit

At the reactor outlet, the reaction products pass out of the hot box to the liquid-gas separator. This system provides the condensation of liquids at low temperature. The liquids accumulate inside the condenser and need to be removed manually by the user.

Reactor parameters are:

- Length: 305 mm
- External diameter: 14.5 mm
- Internal diameter: 9 mm

- Material: 316-L Stainless steel
- T_{\max} recommended: 700 °C
- P_{\max} recommended: 1350 bar at 25 °C; 400 bar at 482 °C (P_{\max} reactor: 100 bar)

The system is connected to a gas chromatograph (490 microGC Agilent Technologies equipped with molecular sieve Molsieve 5Å, PoraPLOT Q and AL2O3/KCl columns) where gas products are analysed. Instead liquid products and waxes are analysed by a Gas Chromatograph-Mass Spectrometer, GC-MS, Agilent technologies 7840 GC – 5975C inter XL MSD (Electron energy 70 eV, Emission 929 V; Column DB-5MS (30 m x 0.25 mm ID x 0.25 µm). NIST EI-MS spectral library has been used for the compounds identification.

3.5 FINITE ELEMENT MODELS

The laws that describe the physics of a system are usually expressed in the form of partial differential equations (PDEs) that are differential equations containing more than one variable. In most of the cases, they are non-linear equations, and they cannot be solved analytically. However, it is possible to approximate these non-linear equations with the linear equation by applying a discretization of the domain in finite element. A typical discretization of a system, called mesh, consists of defining components called elements that are connected in points called nodes. The solution of the complete system corresponds to the assembly of each small domain. Finite element method (FEM) is used to compute the solution of the complete system by applying the linear approximation of the equations in the small elements of the domain. In this way, it is possible to describe the behaviour of an engineering system modelling physics such as heat transfer, mass transport, fluid flow, kinetics of the reactions. The convergence and accuracy of the solution depend on the hypothesis done in the model and numbers of element used in the domain. Computing a very fine mesh can be difficult for high computational time. For this reason, it is usually applied to a refinement of the mesh. After computing the first solution, it is created a denser mesh in the zone of the domain with higher error.

FEM method can be applied to model the fixed bed reactor and study the performance of the catalyst. The typical modelling approaches widely used for an accurate description of the reactor are shown in (Figure 25). The main difference is in the types of assumption used in pseudo-homogeneous model and heterogeneous model. The pseudo-homogeneous model is applied if the heat and mass transfer limitations between the fluid phase and the solid phase are negligible. Thus, it is assumed that the bulk fluid and the surface of the catalyst are at the same temperature and the diffusion effect inside the pore of the catalyst are ignored. The heterogeneous model is more complicated because it considers heat and mass transfer limitation and it is applied when these effects carry out considerable resistance to the reaction rate which is not uniform inside the catalyst particles.

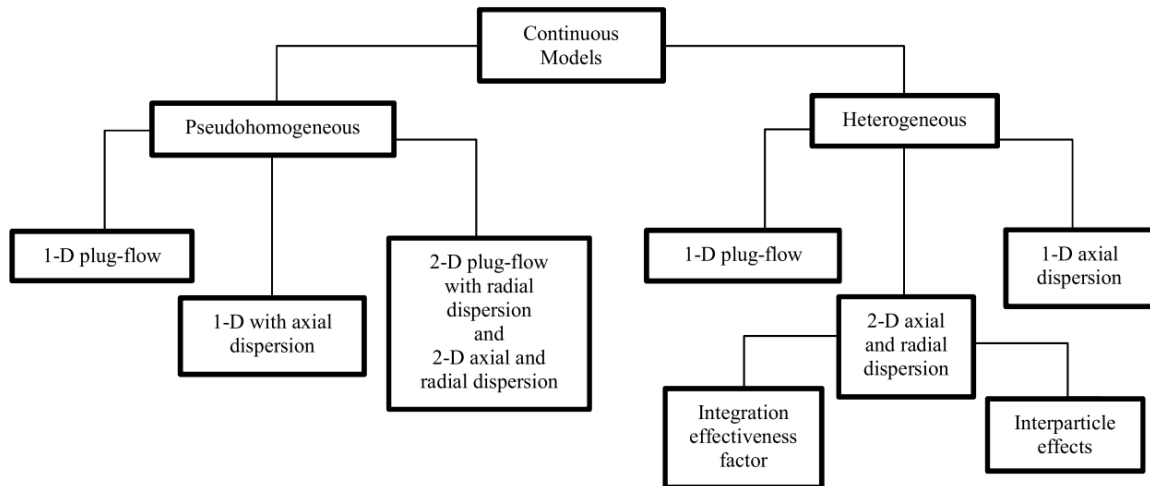


Figure 25 - models commonly used for describing catalytic FBR [17]

In this work, it is developed a pseudo-homogeneous model using as software COMSOL Multiphysics 5.5. An explanation of the model will be done in section 4.4.2.

4 RESULTS AND DISCUSSION

4.1 STUDIES ON THE STRUCTURAL, MICROSTRUCTURAL AND ENGINEERING PROPERTIES OF Al_2O_3 (3D-PRINTED SUPPORT)

In this chapter, the main characteristics of the 3D-printed material used as catalyst's support for the Fischer-Tropsch (FT) process are studied. The support is like the skeleton of the catalyst. Material and structure of the support influence the dispersion and consequently the properties of the FT-catalyst systems. The most frequently used supports described in the literature are alumina, silica and titania [18].

Among them alumina (Al_2O_3) is an electrical insulator with relatively high thermal conductivity ($30 \text{ Wm}^{-1}\text{K}^{-1}$) in comparison with other ceramic materials. A relatively high thermal conductivity is demanding during the process to remove heat generated by the FT process owing to highly exothermal reactions so that hot spots that lower the catalytic efficiency, are avoided. The characterization of the alumina phase is mandatory to understand the interactions between the active catalytic phase and the alumina support. Furthermore, the density, thermal conductivity, and heat capacity of the alumina material after 3D-printing and thermal processes are characterized as a function of temperature in order to apply these data for finite element modelling (FEM).

In order to characterize the properties of the Al_2O_3 used as printing/support material, square pellets of 10 mm side and a thickness of 2 mm are printed for the characterization of the material. This simple geometry consents the use of them in the different apparatus and the measurement of the effective volume after the processes.

4.1.1 Phase, Microstructural and morphological characterization upon the 3D-printing process

4.1.1.1 XRD upon the 3D-printing process

In (Figure 26) it is possible to observe the diffractograms during the 3D-printing and thermal processes. As seen, after the 3D-printing process the pellet is already composed of the alpha-alumina phase and this phase remains stable over all the process. Therefore, the alumina support used for the production of the catalyst is composed only of the α -alumina with a rhombohedral crystallographic structure with a space group (S.G.): *R-3CH*.

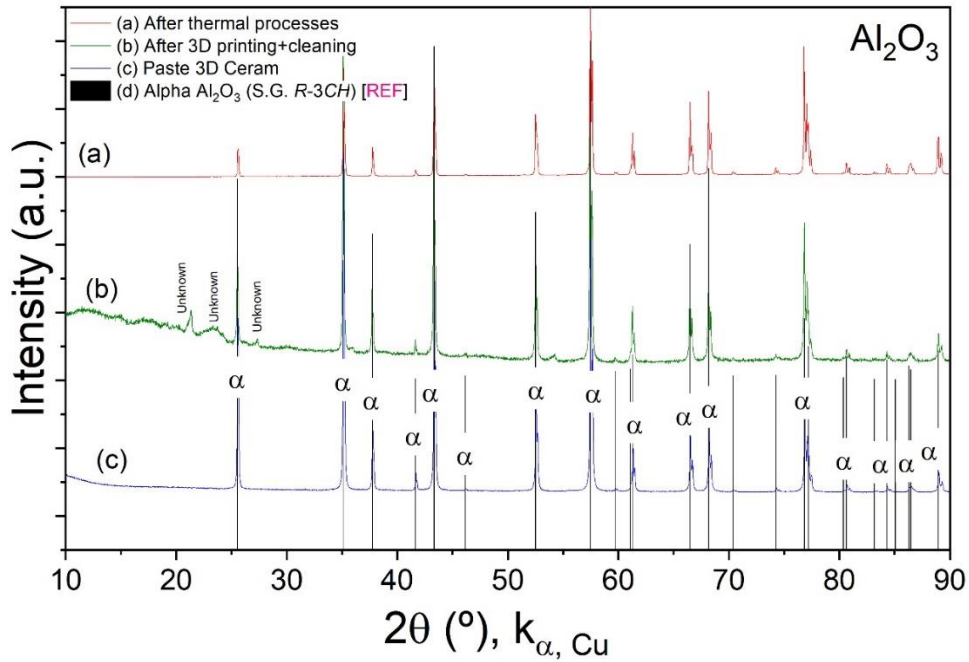


Figure 26 - XRD of the alumina during the 3D-printing and thermal process. XRD reference card from [19]

More than one publication compares the use of the α -alumina with the γ -alumina proving that α -alumina shows higher selectivity [20].

4.1.1.2 SEM upon the 3D-printing process

SEM pictures of the surface of the pellets are performed after each process to study the changes of the microstructure. The rise in porosity after the Debinding can be seen from the more pronounced presence of dark areas in (Figure 28) than in (Figure 27).

Comparing the (Figure 29) and the (Figure 28) the effect of the Sintering is evidenced from the different form of the particle. After the Debinding the particles are well defined then they merge each other forming connections and big particles.

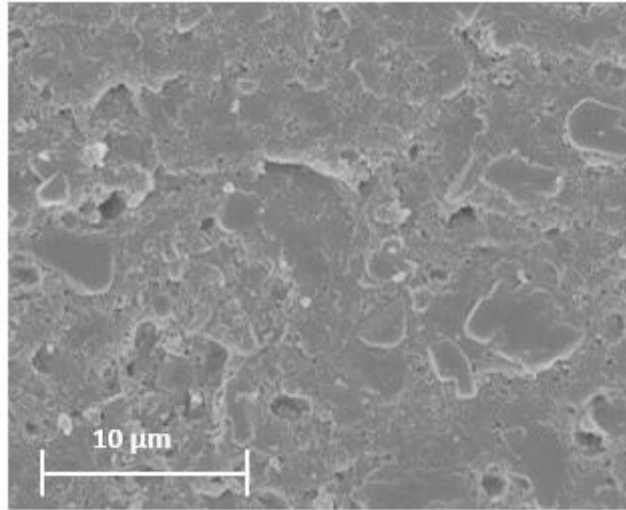


Figure 27 -SEM photo after 3D-printing

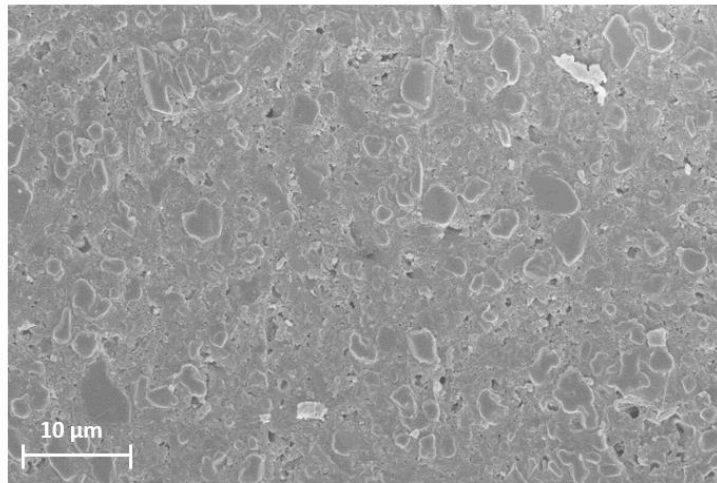


Figure 28 - SEM photo after debinding

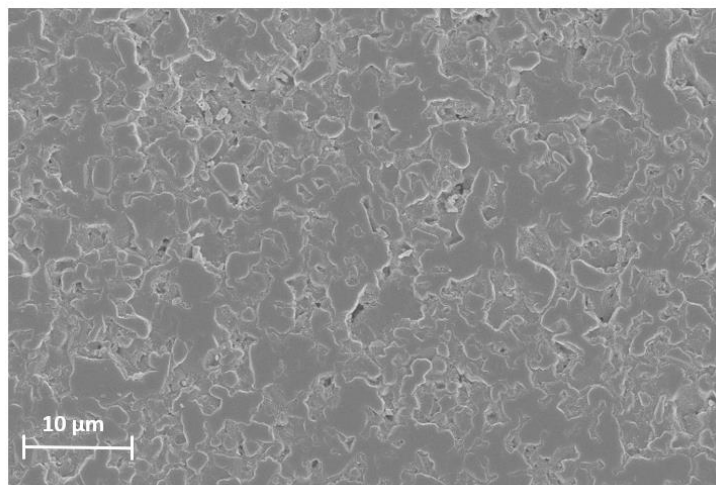


Figure 29 - SEM photo after Sintering

4.1.1.3 Density at room temperature along the 3D-printing and thermal process

The calculation of the density is performed after each thermal treatment with the aim to see its variation during the thermal treatment is in agreement with the SEM observations. Moreover, the determination of the density is needed to correlate it with thermal properties such as thermal conductivity and heat capacity.

The density is one of the fundamental properties to characterize a material. In this study, the density can be considered as the first fundamental property to determine how high the thermal conductivity of the material will be. In this way, it is possible to compare it with the reference properties of the crystalline structure and see how far they deviate from it.

The dimension of square alumina pellets was measured and weighted after printing and after each thermal treatment (3.1.3). The ratio between weight and volume represents the density. Obviously, given the possible measurement errors, more than 20 pellets were compared and the average of the densities was made.

The value of the density, at ambient temperature and at the end of the thermal treatments, had a value of 3155 kg/m³ (bulk density).

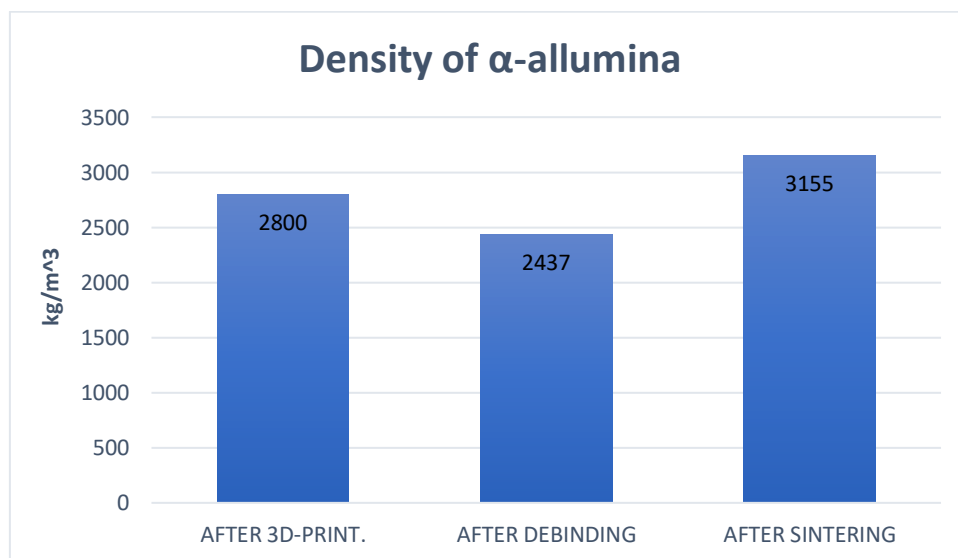


Figure 30 - Density of alumina after each thermal process

(Figure 30) After printing, the material is composed of a mixture of alumina and polymer contained in the starting paste, amounting a density value of 2800 kg/m³. The debinding process allows vaporizing the polymer, thus only the alumina is left. After debinding, the material seems to be slightly more porous than the one after the 3D-printing process (FIG. SEM) and besides, the polymer is gone; hence the density is diminished down to 2437 kg/m³. This fact is mainly attributed to the fact that the weight of the material is lower owing to the absence of the polymer, while the volume is kept almost unchanged. After sintering, the material shrinks and the reduction of the porosity leads to the higher density, i.e. 3155 kg/m³.

4.1.2 Determination of engineering properties

The thermal properties of the sintered support have to be calculated within the range of temperatures of interest for the seek application, i.e. between 25 and 300 °C. The properties to be calculated as a function of temperature are: the **density**, the **specific heat capacity** and the **thermal conductivity**. For each of these properties, experimental data was collected according to the procedures described in section 3.3. The obtained characterizations as a function of the temperature are compared with data from databases in order to verify its validity. Then the equations that describe the variation of the properties along the temperature are set. These equations allow defining the material acting as catalyst's support in the FEM interphase, so that a more accurate model can be created.

4.1.2.1 Density as a function of temperature

From the XRD data the presence of the α -alumina was confirmed. It has a crystalline density of 3900 kg/m³ (particle density). However, in the previous section, we determined the density obtained from the alumina after the 3D-printing and thermal processes, amounting to a value of 3155 kg/m³.

These two values allow to calculate the **porosity** of the material with the following formula:

$$\varepsilon_{Al_2O_3} = \left(1 - \frac{\rho_{bulk}}{\rho_{crystal}} \right) * 100 \quad [\%] \quad (4.1)$$

where ρ_{bulk} is defined as the density of the alumina after 3D-printed+thermal processes (3155 kg/m³), $\rho_{crystal}$ refers to the density of the dense alumina (3900 kg/m³), and $\varepsilon_{Al_2O_3}$ is defined as the porosity of the herein obtained alumina. This calculation provides a porosity of 22 %.

To obtain the variation of the density as a function of the temperature for the alumina after 3D-printing+thermal processes, the FEM database software was used. The polynomial equation of the density as a function of the temperature for the polycrystalline alumina was taken and then the calculated porosity was considered. As a result, the following polynomial equation was determined:

$$\rho(T) = 3122.77 - [0.01874 * T] - [7.18278 * 10^{-5} * T^2] + [3.55662 * 10^{-8} * T^3] - [7.09974 * 10^{-12} * T^4] \quad \left[\frac{kg}{m^3} \right] \quad (4.2)$$

(Figure 31) depicts the difference of the densities as a function of temperature between the polycrystalline alumina from the database and the one here calculated. As seen, as expected, the trend is the same, but owing to the porosity of the alumina obtained after 3D-printing+thermal process, the density over all the temperature range is lower. As seen, the variation of the density with the temperature is not considerable. However, the equation is applied in the model to reduce the error

between the experiment and the model. Moreover, the obtained equation is also useful to obtain a more realistic behaviour of the thermal conductivity as a function of the temperature.

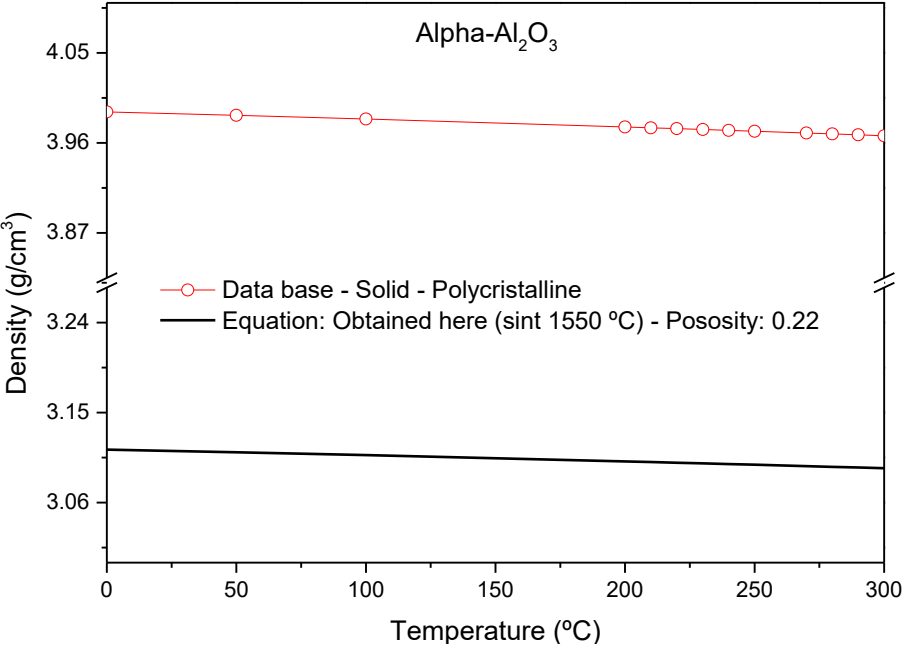


Figure 31 - $\alpha\text{-Al}_2\text{O}_3$ density

4.1.2.2 Specific heat capacity as a function of the temperature

The specific heat capacity of the alumina was obtained with the DSC analysis described in section 3.3.2. (Figure 32) shows the variation of the heat flux needed to increase the temperature of both sample and reference.

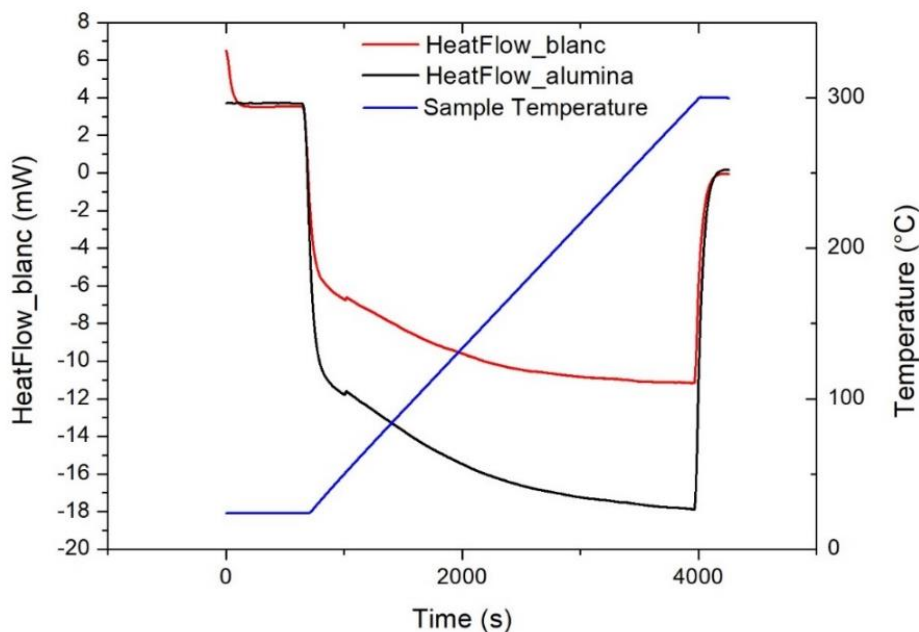


Figure 32 - DSC graph of the heat flux upon the process

As the material absorbs heat, results are negative. Applying the ramp method (3.3.2) it is possible to obtain the heat capacity as a function of the temperature. After subtracting the blanc curve belonging to the sample holder, it is possible to obtain the heat flux of the sample and then applying the equation (3.6), the specific heat capacity in all the temperature range was calculated. Afterward, a polynomial function was fitted to the obtained experimental points, as shown in (Figure 33). It is possible to see that the curve of the cp for polycrystalline alumina from the FEM software database exhibits the same trend in the measured range of temperature.

The results were compared with the database. The translation toward low capacities is easily explained by the lower porosity of our material. The thermal capacity increases with temperature providing a good performance to absorb the heat produced by the reaction.

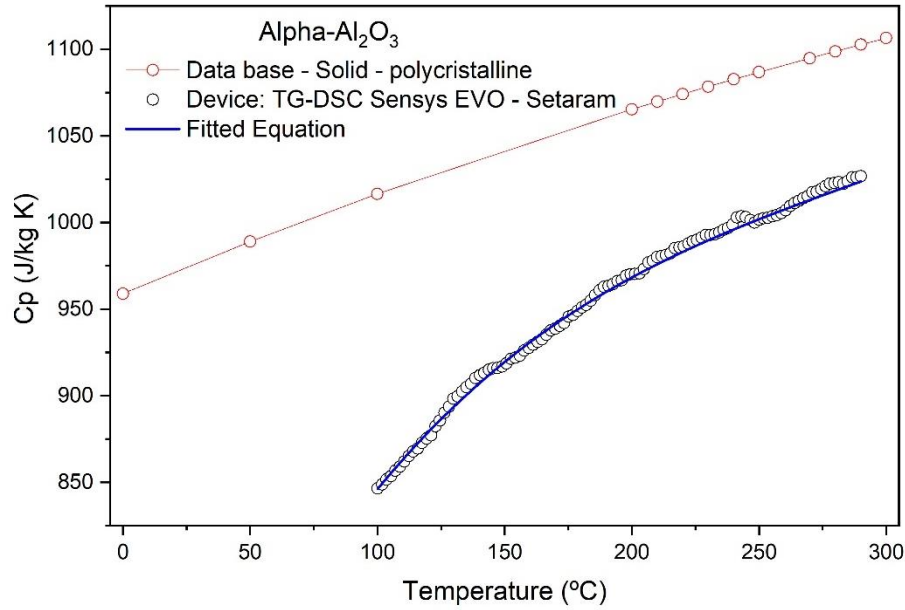


Figure 33- Specific heat capacity of α -Al₂O₃

From the fit of the equation shown in (Figure 33), the following dependence of c_p on the temperature was obtained:

$$c_p(T) = -1560 + [13.4 * T] - [2.53 * 10^{-2} * T^2] + [1.93 * 10^{-5} * T^3] - [3.81 * 10^{-9} * T^4] \quad \left[\frac{J}{kg * K} \right] \quad (4.3)$$

4.1.2.3 Thermal conductivity as a function of the temperature

In the LINSEIS XFA 600 the measurement of thermal diffusivity $\alpha(T)$ at different temperatures was performed applying the pulse method; all the experimental details are described in section 3.3.3. As seen in (Figure 34), the experimental data follow the same trend as the ones obtained from the database. In this case, as it happens with several thermal properties, the porosity reduces the thermal diffusivity of the material. In equation (4.4), it is possible to see that the thermal conductivity is proportional to properties previously measured such as the density and the heat capacity as well as the thermal diffusivity. Therefore, the presence of porosity also reduces the thermal conductivity.

$$\lambda(T) = c_p(T) * \rho(T) * \alpha(T) \quad (4.4)$$

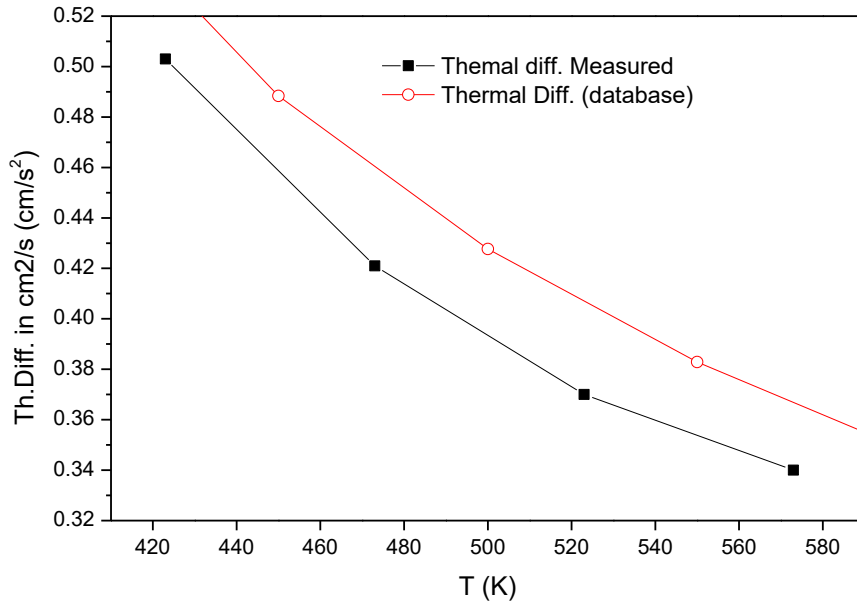


Figure 34 - Thermal diffusivity α -Al₂O₃

In (Figure 35) the behaviour of the thermal conductivity of our material (red line) agrees with the database (black line). As it is expected, the values are lower due to the porosity. This is confirmed by a model that calculates the **effective thermal conductivity** of a material based on its porosity (blue line) [21]:

$$\lambda_{eff} = \varepsilon_{Al_2O_3} * \lambda_{air} + (1 - \varepsilon_{Al_2O_3}) * \lambda_s \quad (4.5)$$

where:

- λ_{eff} effective thermal conductivity
- $\varepsilon_{Al_2O_3}$ porosity of the alumina
- λ_{air} thermal conductivity of air
- λ_s thermal conductivity of the alumina from database

The equation that describes the fitted curve is then used in COMSOL:

$$\lambda(T) = 61.2 - [0.161 * T] + [2.054 * 10^{-4} * T^2] - [1.494 * 10^{-7} * T^3] + [5.0506 * 10^{-11} * T^4] \quad \left[\frac{W}{m * K} \right] \quad (4.6)$$

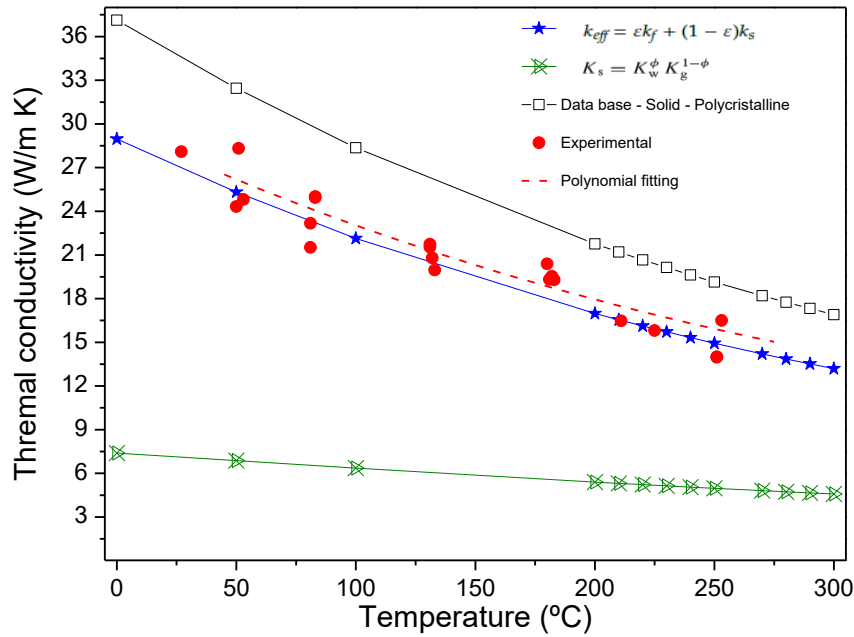


Figure 35 - Thermal conductivity $\alpha\text{-Al}_2\text{O}_3$ in comparison with the database and models taking into account the porosity

4.1.3 Conclusions

The characterizations of the phase composition (XRD), microstructure (SEM), as well as properties of engineering interest as a function of the temperature such as density, heat capacity and thermal conductivity were performed. All these properties are crucial for the present work. On the one hand, the phase composition and microstructure of the support (alumina) are relevant for the design of the catalyst (support + active phase) since the interaction between the support and the active species determines catalytic activity. On the other hand, the properties of engineering interest are demanding at the time to design an efficiently fixed bed reactor with adequate pellet geometry applying FEM design.

The XRD measurement shows that the phase of the alumina doesn't change upon the thermal treatment and is confirmed to be $\alpha\text{-Al}_2\text{O}_3$. Moreover, an increase of the particle size due to the sintering process at high temperatures is evidenced via SEM observations. The calculation of the density upon the processes confirms the variation of the porosity. Finally, the determined equations of the density, heat capacity and thermal conductivity describing their evolution with temperature are useful information for the design by FEM tools.

4.2 TUNING THE GEOMETRY OF A SINGLE PELLET BASED ON 3D-PRINTED SUPPORT FOR CO-RE PROMOTED CATALYST FOR FT SYNTHESIS

In this section, it is explained how the geometry of the pellets is set as well as how the procedure for the applied 3D-printing process to obtain the pellets is developed. Based on the literature [22], a spherical geometry is selected since it provides the possibility to work with eggshell catalyst where Co is located on the pellet surface. Therefore, and according to previous works, the internal diffusion constraints (insider the pores of the catalyst) can be neglected. This hypothesis lays on the fact that with the eggshell configuration the catalytic active phase is located on the surface of the support and not inside the particle. Hence, the limiting step of the reaction falls into the chemical reaction rate control and not into the diffusional regime [23].

The eggshell type shows high performance and selectivity of C^{5+} in the same operating conditions [24] [22], especially when the thickness of the catalytic layer on the support's surface is small enough to avoid the internal diffusion limitations [25].

To tune the spherical geometry, the experimental capabilities of the 3D-printing device are analyzed.

4.2.1 Printing strategy of the spherical pellets

In order to produce the catalyst's support, an additive manufacturing procedure is applied: 3D-printing Stereo Lithography (SLA) of ceramic materials. All the details of the experimental procedure are described in section 3.1. As 3D-printed material, the alpha phase of alumina in the form of paste is used.

A crucial condition during 3D-printing process is the stability of the printed pieces on the printed surface. When the species to be printed are not correctly attached, the scrapping process induces shifts and leads to deformed printed geometries. The sphere is highly influenced by this effect due to the low contact surface with the platform. Therefore, a strategy is adopted to increase the chances of a successful printing process. As seen in (Figure 36), the pellets are flattened in the bottom part, and they are embedded onto a thin platform, procuring an effective attachment of the pellets and avoiding deformations during printing. Moreover, all pieces to be printed are merged all together as unique piece by using the software Soliworks (pellets + platform) in order to minimize the required live memory. This approach allows the production of a larger quantities of pellets in one 3D-printing process.

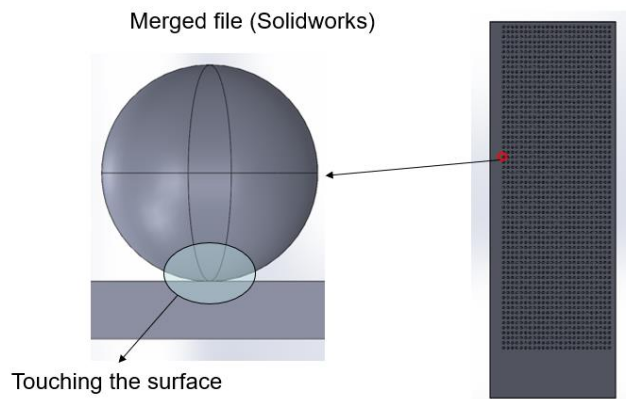


Figure 36 - Strategy adopted to print spherical pellets

This strategy was successfully tested for smaller diameter spherical pellets (1 mm) as shown further on 4.2.2.

4.2.2 Capabilities of the 3D-printing technique

The sphere was chosen as starting geometry but two geometries were printed in order to learn the constraints induced by the 3D-printing fabrication approach and our capability to clean the pieces:

- Spheres with two different diameters ($d=1$ mm; $d=0.3$ mm)
- Square pellets with holes of different diameters

The diameter of a typical spherical pellets used in fixed bed reactors for industrial applications ranges goes from 1 to 3 mm. These diameters allow good catalytic performance (high C^{5+} hydrocarbon selectivity, appropriate reactants conversion and catalyst's stability), low big drops of pressure and good mechanical stability. At a laboratory scale, it was demonstrated that small sphere supports (0.2 to 0.5 mm) with an eggshell catalyst configuration with a catalyst's thickness of less than 0.13 mm appreciably diminishes the internal diffusion limitations, hence promoting higher selectivity distribution towards C^{5+} in FT synthesis [22]. In this case, the relatively large diameter of 1 mm and the fact that the catalytic layer would be located on the surface represents an efficient trade-off between the activity and selectivity of the catalyst and the drop of pressure.

These above-mentioned aspects were considered at the time to carry out the 3D-printing process. In (Figure 37), photos were taken in an optical microscope (A) and in a SEM microscope (B) of the 3D-printed spheres of **1 mm of diameter** are shown. Around 1600 pellets were printed all at once. The successful cleaning allows to see the defined shape of the balls and the layers produced by the machine. The separation of the pellets from the platform was not perfect and part of the platform remained attached to the surface; this detachment issue is further addressed in the section about the catalytic layer deposition.

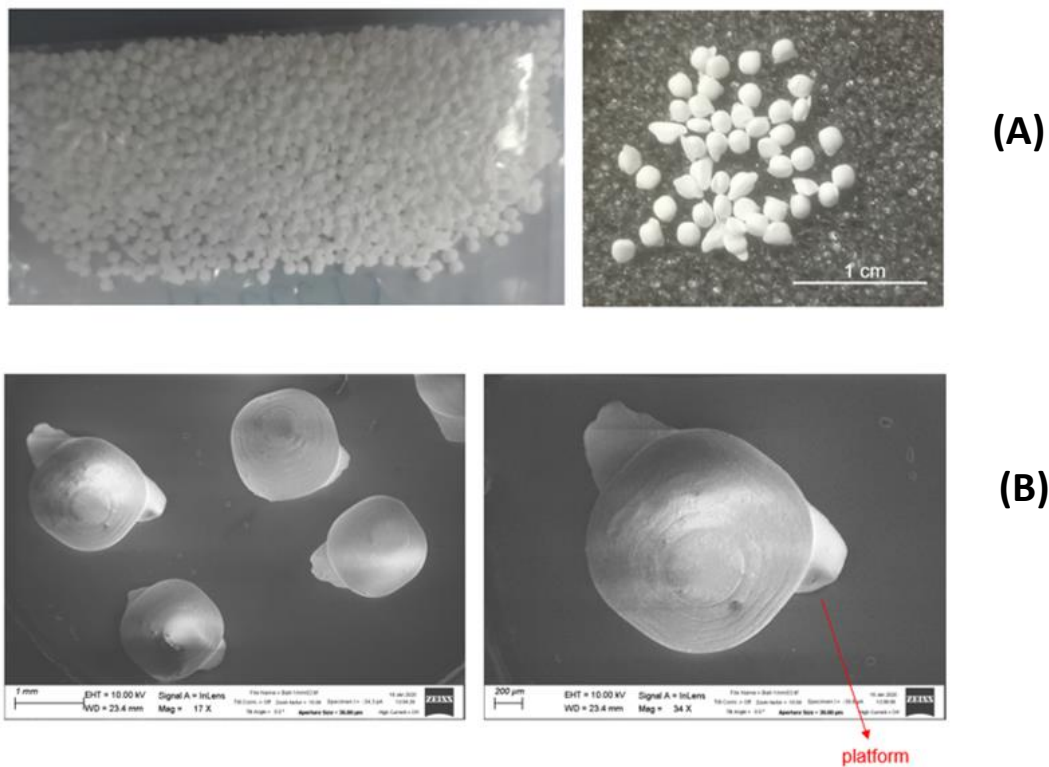


Figure 37 - 3D-printed sphere of $d=1\text{ mm}$

The BET area of the pellets before the deposition of the catalyst was measured to provide a comparison point with the measurement of pellets after the catalyst deposition. (Figure 38) shows the BET area measurement in which it is possible to see that a low amount of hydrogen is adsorbed and from this we evaluate the BET area value at $0.4\text{ m}^2/\text{g}$.

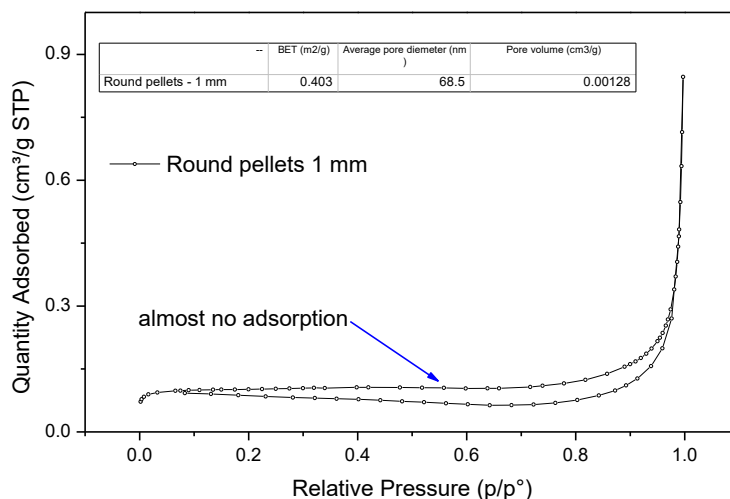


Figure 38- BET area of alumina spherical pellets

Smaller diameter spherical pellets were also designed; the **$d=0.3\text{ mm}$ balls** were programmed in the printer. As this size is below the theoretical resolution limit of the printer, this was used as well as a test to know the minimum diameter that we could obtain using the 3D-printing process. According to the literature, this smaller support should provide with a better selectivity. (Figure 39) shows a good result and confirms the possibility of producing smaller spheres. However, some difficulties have been

encountered during the cleaning process and the measurement of the surface area. The success ratio of printed spheres dropped considerably compared to the first try. Regarding the surface area (BET area), it was not possible to measure because of the low value under the limits of the BET area device. As it is shown in (Figure 39), the shape of the printed pellets is not as spherical, but rather cylindrical with about 0.2 mm of diameter and 0.1 mm of height. Therefore, at this small size, it not possible to control the shape of the pieces upon the 3D-printing process and further thermal process to obtain the final pieces.

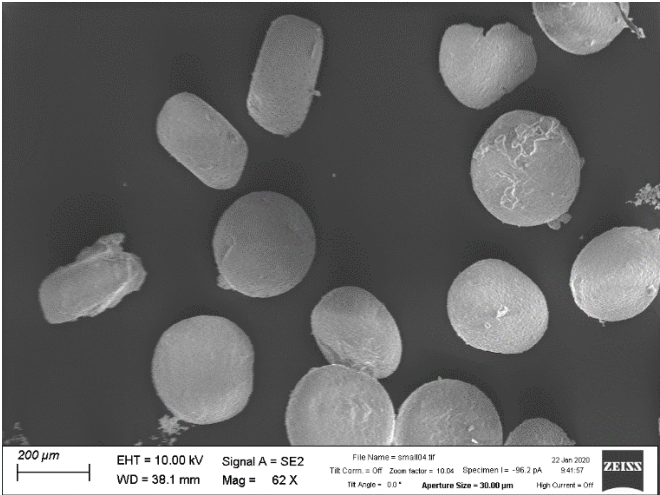


Figure 39 - 3D-printed sphere of d=0.3 mm

Another approach to improve the surface available for the catalyst was devised and the possibility to build a hole across the spheres was considered. Flat square pellets of 5x5 mm in size with different diameters of holes were printed to test once again the capabilities of this technique. As seen in (Figure 40), not all the holes went through the part. The high viscosity of the paste made it difficult to remove it from inside the holes and the minimum hole diameter properly cleaned was **d=0.75 mm**. This value represents a constrain to account for during the design.

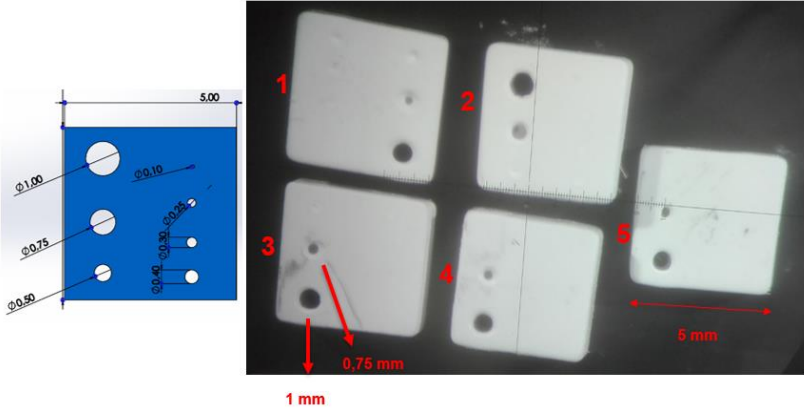


Figure 40 - 3D-printed square pellets with different holes size

4.2.3 Conclusion

The applied printing strategy allows producing 1mm spherical pellets with a manageable shape and the possibility to print a large amount of them at the same time: about 1600 pellets in the case to use a 100 mm x 300 mm platform, and up to 4800 pellets in the case to use the 300 mm x 300 mm platform. The surface area of the printed pieces amounts to 0.40 m²/g. The obtained surface area is quite small for catalyst support, since it is usually over 150 m²/g [26]. However, an eggshell catalyst design does not demand such high surface area because the catalytic layer should lie on the surface. The reduction of the diameter of the pellets by design up to 0.3 mm was adopted in order to further try to tune the geometry of the pellets support. However, that small size leads to an unmanageable shape. Furthermore, this small size presents difficulties at the time to apply the cleaning procedure after the 3D-printing process, leading to a substantial loss of the number of 3D-printed pellets. Moreover, the surface area is not possible to measure since it is smaller than the measurement limits of the BET area device.

The possibility of inserting a hole in the sphere increasing its surface area did not lead to the desired results since the minimum allowed size of a hole is 0.75 mm, which is not small enough to fit a 1 mm sphere considering the printing resolution of the device.

Taking into account the capabilities of the 3D-printing device and the performance of different support's geometries reported in the literature [22], it was possible to reach an efficient compromise between the tuned design, based on CAD and the 3D-printing process, and the catalytic performance by proposing an eggshell configuration with 1 mm spherical pellets support.

4.3 IMPREGNATION AND CHARACTERIZATION OF CO-RE PROMOTED-AL₂O₃ SUPPORTED CATALYST BASED ON 3D-PRINTED SUPPORT

An efficient Fischer–Tropsch catalyst needs high hydrogenation activity in order to catalyze the hydrogenation of CO to higher hydrocarbons. This property is enhanced for transition metals of the fourth group of the periodic table: iron (Fe), cobalt (Co), nickel (Ni) and ruthenium (Ru). However, ruthenium has a high cost and low availability and nickel favours the production of methane. Thus, the commercialized catalysts for FT process are iron and cobalt. For this work we chose cobalt as, respect to iron, it shows low water-gas shift (WGS) activity and higher CO conversion and selectivity of C⁵⁺ [6]. Furthermore, a small quantity of a promoter is added to favour the dispersion of the cobalt particles during the preparation of the slurry and to promote the reduction of the cobalt oxide (Co₃O₄) to metal cobalt. The most used promoters for this purpose are rhenium, platinum and ruthenium. The choice for this study was rhenium (Re) as its high capability to improve the performance of Co/Al₂O₃ catalyst is reported in several papers [3,7,20].

In this section, it is explained the catalyst impregnation procedure on the surface of the round pellets as well as the results obtained from its characterization *via* SEM, XRD, TPR, TPR/TPO and BET area. In addition, the effect of the support and promoter are discussed.

4.3.1 Catalyst impregnation over Al₂O₃ spherical pellets

The preparation of the slurry and subsequent impregnation procedure is described in section 3.2.

The slurry contained the catalyst in its oxide form (Co₃O₄) and the promoter (Re). It was prepared by wet mechanical milling (deionized) to reduce particle and crystalline size, and to reach an homogenous mixture of between the oxide and the promoter. Subsequently, the obtained slurry was centrifugated to separate it from the grinding medium. Rhenium content involved was 0.5 % of weight of the cobalt as the bibliography suggests. It was reported that adding more than 0.5 wt% of Re, respect to the Co active phase, has no further effect [7].

The impregnation with an excess of solution on the support was performed in the rotary vacuum dryer for the evaporation of the deionized water. Then, the impregnated pellets were calcinated in an oven at 400 °C for 4h. The amount of deposited solution cannot be calculated beforehand because part of the catalyst is lost during the impregnation. This method allows the high dispersion of the products on the surface and works well when there is an ion-solid interaction. Extensive restructuring of the surface may occur (loss of surface area, etc.). After the impregnation the pellets appear well covered by the catalyst that has a black colour (see Figure 41).

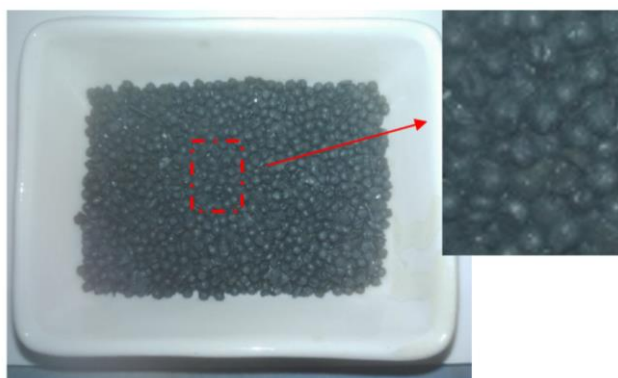


Figure 41 - Eggshell Co-Re/Al₂O₃ supported pellets

By weighting the pellets before and after the impregnation and knowing the stoichiometry of the precursor (Co₃O₄), an approximation of the Co wt.% is calculated (Table 2). Using 2 g of starting powders, less than 0.5 g of catalyst stuck to the support. We estimate the amount of metallic cobalt up to 6%.

Table 2 - Calculation of the mass of catalyst and promoter over the support after impregnation

Mass of starting powders (Co ₃ O ₄)	Mass [g]
Mass of starting powders (Co ₃ O ₄)	2
Mass pellets of α-Al ₂ O ₃	7.451
Mass of powder lost after drying + calcination	1.130
Mass of powder lost during the evaporation	0.337
Mass pellets + catalyst after drying + calcination	7.929
Mass of catalyst (Co ₃ O ₄ + Re) stuck after calcination	0.478
Mass of metal Co	0.475
Mass of Re based on 0.5 % of Co	2.389E-3

4.3.2 Characterization of the Co-Re/Al₂O₃ supported pellets

This section contains the results obtained from the TPR, TPO and BET area analysis. SEM images and XRD measurements were performed before and after TPR and TPO analysis to unveil the variation of the catalyst composition and thickness along the processes.

The X-ray diffraction pattern after impregnation shows peaks allowing the identification of cobalt oxide (Figure 42). Therefore, the calcination process did not change the oxidation state of the cobalt and the support is still α -Al₂O₃.

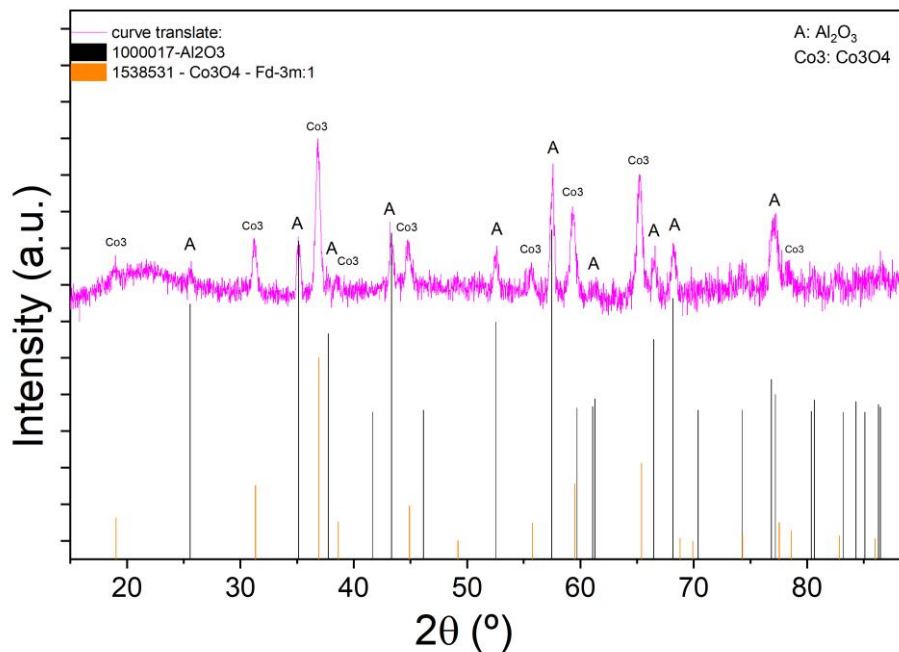


Figure 42- XRD of Co-Re/ α -Al₂O₃ pellets after impregnation

The calcination process induces the diffusion of cobalt oxide molecules inside the alumina, creating a larger contact layer between the two and, as consequence, a better attachment as we observe in the SEM (Figure 43). Moreover, it is possible to notice a well compact microstructure of the catalyst layer that ensures higher diffusion limitation and better performance.

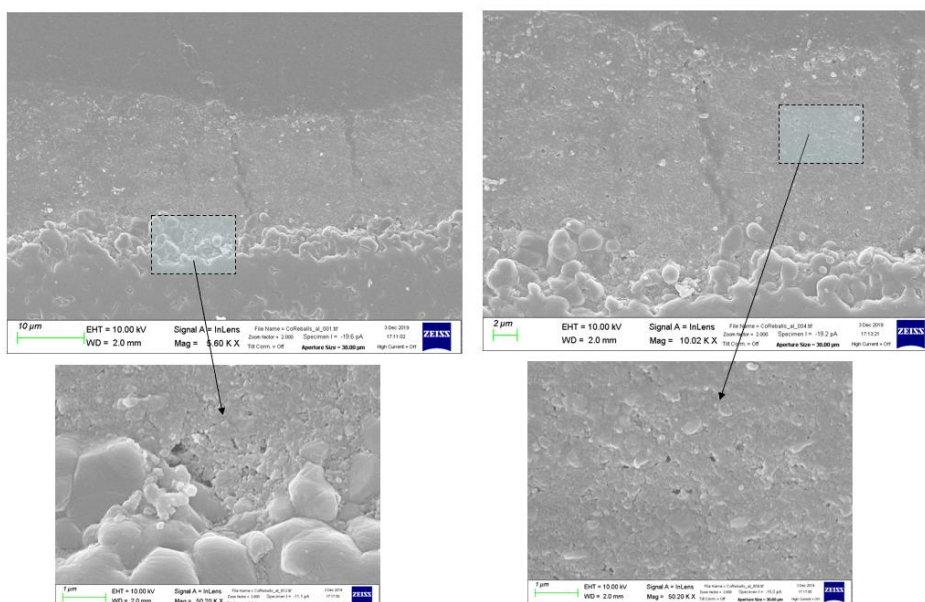


Figure 43 - SEM of catalyst layer where the microstructure of the cobalt oxide and its attachment with the alumina are highlighted

TPR was performed to measure the reduction properties of the cobalt layer with the contribution of support and promoter. We observe that the support enhances the dispersion of the catalyst and, if the alumina has large particle size, improves its reducibility [18]. The Rhenium on the other hand, improves the percentage of reduction of cobalt and lowers the reduction temperature [7]. The condition applied for the analysis are reported in (Figure 44) and in section 3.3.5. Cobalt usually shows a TPR profile with two peaks related to two steps of reduction: from Co_3O_4 to CoO and from CoO to Co^0 , occurring at different temperatures. In our case only one peak was visible (Figure 44) and led to the conclusion that the two reactions were overlapped and they occurred at 338.7°C . The catalyst is expected to be completely reduced beyond 400°C .

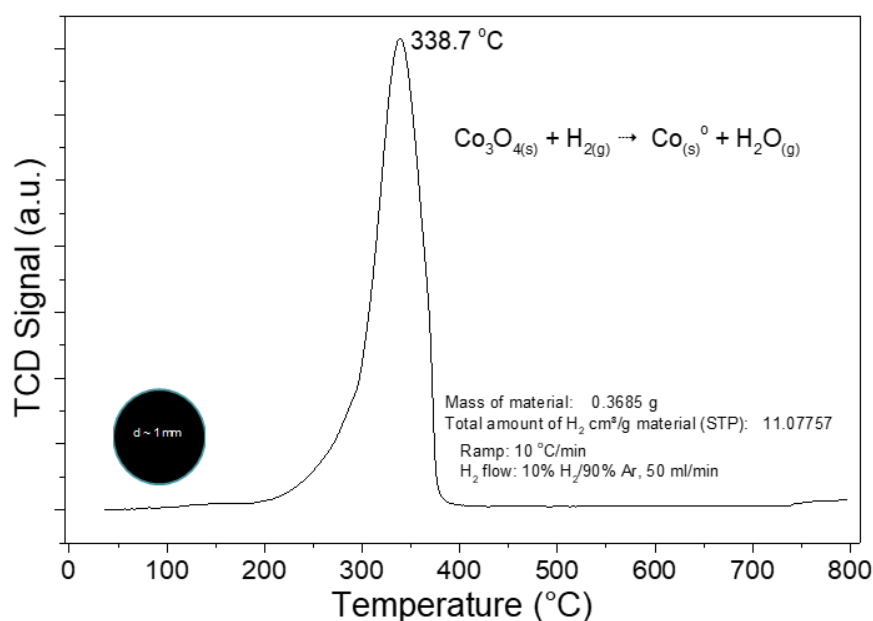


Figure 44 - TPR analysis of Co-Re/ α - Al_2O_3 pellets

The support did not participate in the reduction and was still oxidized. The area below the TPR profile allowed the evaluation of the total amount of hydrogen consumed ($11.07 \text{ cm}^3/\text{g}_{\text{material}}$) that was used to calculate the amount of cobalt reduced taking into account the stoichiometry of the reaction.

Carbon oxide activation depends on the crystalline structure of the metal cobalt obtained after reduction and HCP phase has much higher intrinsic activity respect to FCC [27]. Depending on the reduction temperature and on the composition of the support, different cobalt phases can be formed. However, a higher fraction of FCC cobalt relative to the HCP phase was found in many studies performed with cobalt-alumina catalysts. Therefore, the stability of such a cobalt phase is still under discussion.

The X-ray pattern of the catalyst after the process (Figure 45) confirmed the complete reduction into metal cobalt with FCC phase. The promoter was not considered because of its low concentration, and because Re does not get oxidized upon the milling an impregnation process; this fact is further discussed below. Thus, our catalyst was composed of **4.6 wt.% Co-0.5% Re/ Al_2O_3 supported**. This value is lower than the estimation done in 4.3.1.

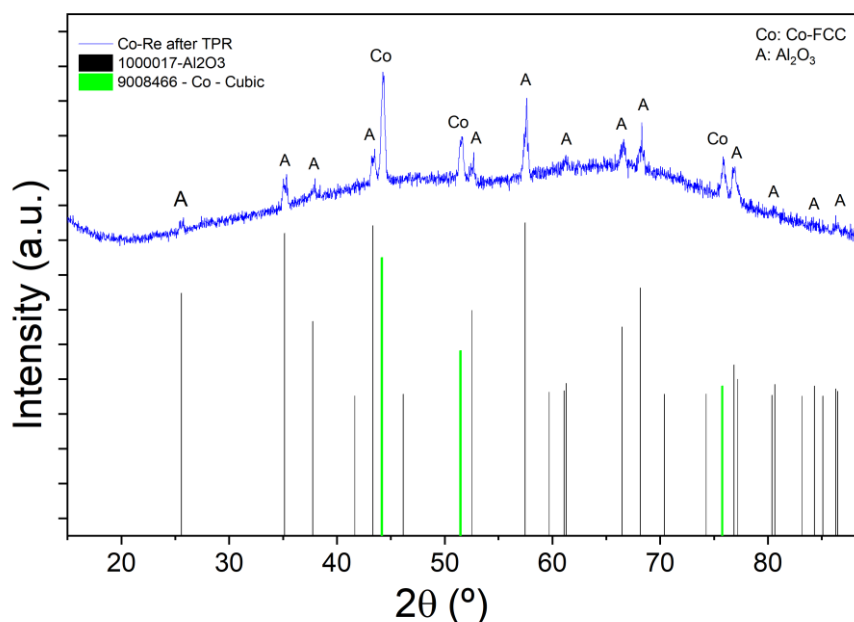


Figure 45- XRD of Co-Re/ $\alpha\text{-Al}_2\text{O}_3$ pellets after TPR

The thickness of the catalyst as seen in the SEM images did not appeared constant (see Figure 46), the average value for the observed pellets was calculated by measuring the thickness in different spots with the i-TEM software (License N^o: A2382500). We obtained a value of 60 μm after synthesis and 20 μm after reduction. The reduction of the thickness is related to the absence of oxygen atoms.

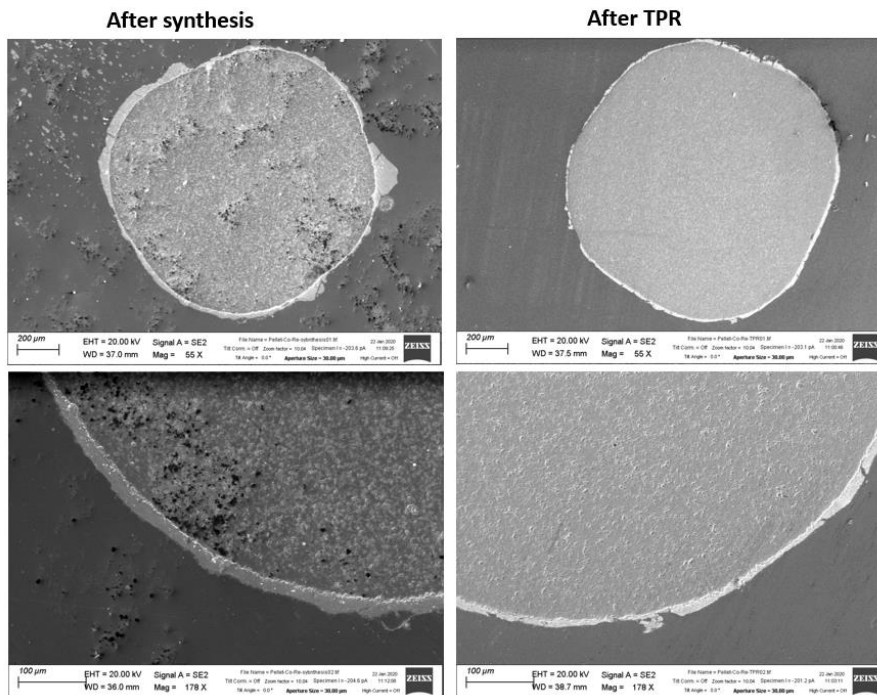


Figure 46 – SEM images of the Co_3O_4 layer after synthesis and metallic Co after TPR

To determine the degree of reduction TPO experiment was performed and compared with the TPR results. TPO measurement was performed giving pulses of O_2 to the sample which was heated at 380°C after reducing the sample under diluted H_2 atmosphere. The TCD signal of each pulse depends on the quantity of gas adsorbed by the sample. During the process a monolayer of cobalt oxide forms on the active surface, as it grows less than at the beginning of the process, and less oxygen is absorbed by the sample increasing the TCD signal until 100% of the injected volume of oxygen is measured. Taking into account the number of pulses and the area below them, the amount of oxygen not consumed is measured, and so the oxygen absorbed by the sample is deduced. Its value was used to calculate the amount of active Co. Considering the 4.6 wt.% of Co calculated from the TPR measurement, we calculate the **degree of dispersion of active sites** (active Co supported in $\alpha\text{-Al}_2\text{O}_3$) (4.7). The result being **47% of dispersion** meaning that **2.2 wt.% of Co** is available as active site.

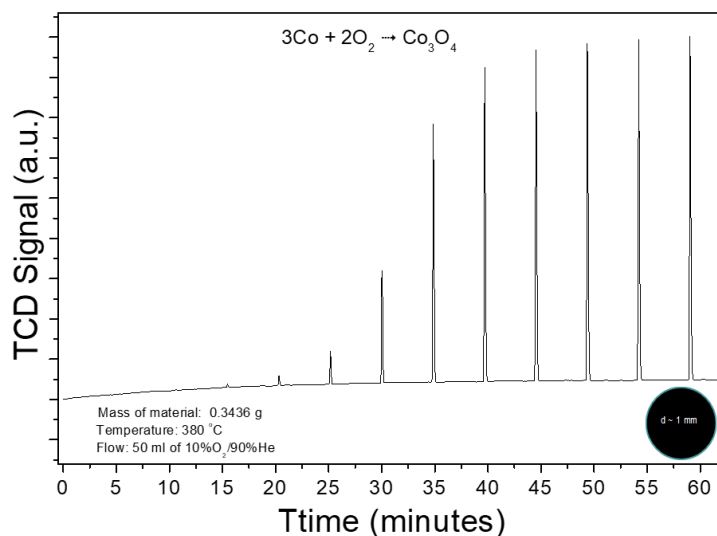


Figure 47 - TPO measurement of Co-Re/ $\alpha\text{-Al}_2\text{O}_3$

$$\% \text{ Dispersion of active sites} = \frac{n^\circ \text{ of Co atoms on surface}}{\text{tot } n^\circ \text{ of Co atoms on sample}} * 100 \quad (4.7)$$

The X-ray pattern performed after TPO (Figure 48) showed that the cobalt content was completely re-oxidized.

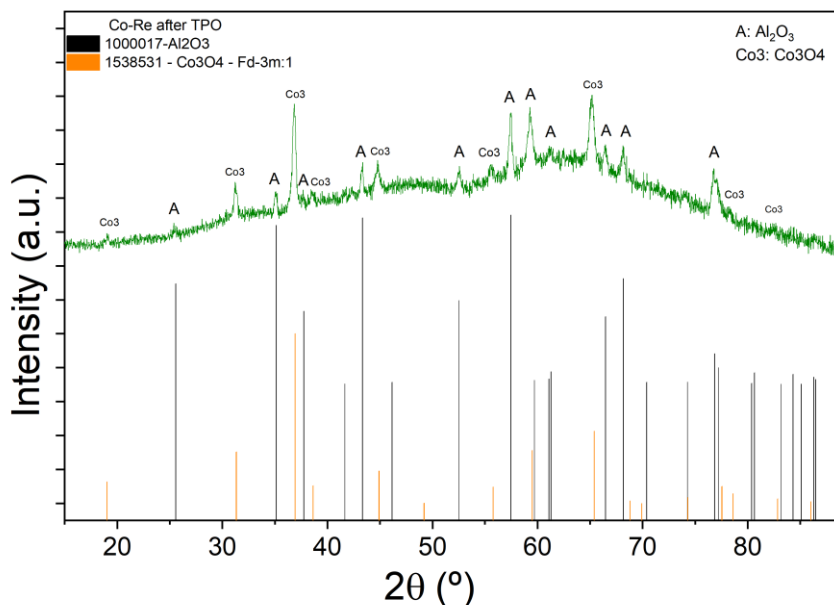


Figure 48 – XRD of Co-Re/ α -Al₂O₃ pellets after TPO

The crystalline sizes were calculated from the full width at half maximum (FWHM) of the selected XRD peaks after synthesis after TPR and after TPO using the Scherrer equation (see 3.3.1). The Scherrer method was applied as a comparative method to analyze the trend of the crystallite size during the characterizations of the catalyst [18]. During the TPR analysis, the temperature increased up to 800 °C, thus the crystallite size grows. This rise in temperature induced an increase in the crystalline mean size as we analyzed it afterwards (Table 3).

$$D_{(hkl)Co^0} = 0.75 * D_{(hkl)Co_3O_4} \quad (4.8)$$

Table 3 – Determination of the crystallite size of Co₃O₄ and Co⁰

State	Compound (plane family)	D_{hkl} [nm]
As purchased	Co ₃ O ₄ (331)	40
After synthesis	Co ₃ O ₄ (311)	20
After synthesis	Co ⁰	15
After TPO	Co ₃ O ₄ (311)	23
After TPO	Co ⁰	17
After TPR	Co ⁰ (111)	24

Co^o dispersion was calculated applying the equation (4.9) and assuming that Co particles are spherical and have a uniform density of 14.6 atoms/nm² [28]. The result is **4% of dispersion**.

$$\% \text{ Dispersion} = \frac{S}{D_{(hkl)Co^o}} \quad (4.9)$$

where S is a constant depending on the catalyst: **96.2** for cobalt [29].

The isothermal physisorption was carried out to calculate the BET area, average pore diameter as well as average volume of the pores:

- BET surface area: 1.58 m²/g
- BJH desorption average pore diameter: 35.76 nm
- BJH desorption cumulative volume of pores between 1.0000 nm and 300.0000 nm diameter: 0.011484 cm³/g

Pores are classified in 3 ranges: macropores (d>50 nm), mesopores (2<d<50 nm), micropores (d<2nm). In our case (Figure 49), the kind of isotherm curve (type II + type IV) indicates that the physisorption occurs in macropores and mesopores adsorbents and the shape is attributed to unrestricted monolayer-multilayer adsorption. Therefore, this kind of hysteresis (H3), located in the multilayer range at high relative pressure p/p₀ in the graph, is given by a pore network consisting of cracks[13].

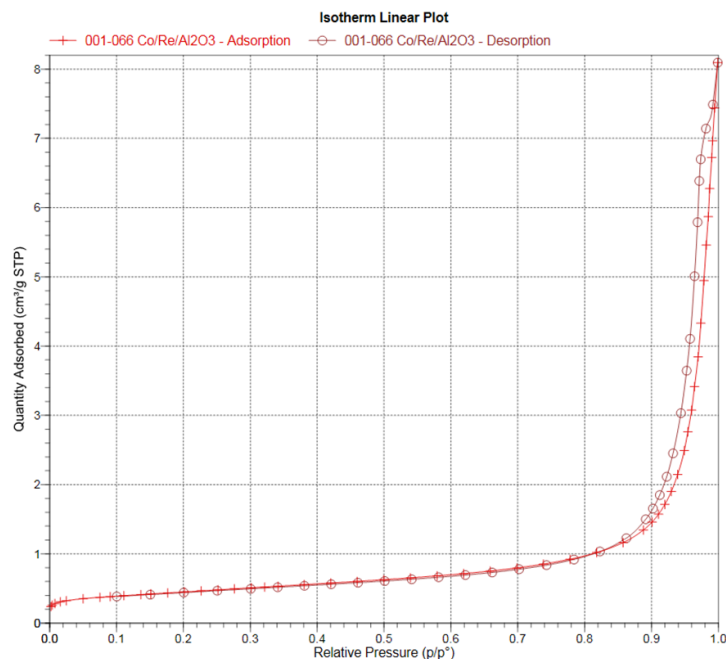


Figure 49 – Isothermal physisorption of Co-Re/ α -Al₂O₃ to determine BET area and pore size

4.3.3 Effects of catalyst preparation, promoter and support and comparison with commercialized catalyst

The active sites of metal cobalt located on the surface of the support formed after reduction influences the activity of FT synthesis. The activity and selectivity of supported cobalt catalysts depend on several factors such as particle size, nature of the support, the presence of promoter and catalyst preparation method. Therefore, a more detailed analysis is needed to understand the effects of such factors. For this purpose, another catalyst without promoter was produced and used for the analysis (4.4% Co/ α - Al_2O_3).

Effect of catalyst preparation:

The used precursor is Co_3O_4 in power form. The applied milling process and, then the impregnation procedure modifies the thermal behaviour of the starting Co_3O_4 .

TPR analyses of the as-purchased Co_3O_4 and Co_3O_4 after milling plus drying in vacuum were done. The TPR curves present similar features (Figure 50). However, the temperature maximum of the main thermal event is lower for the sample after the milling + drying process. Moreover, it appears to be a positive effect of the milling process on the particle size distribution owing to the absence of the shoulder in the main thermal event.

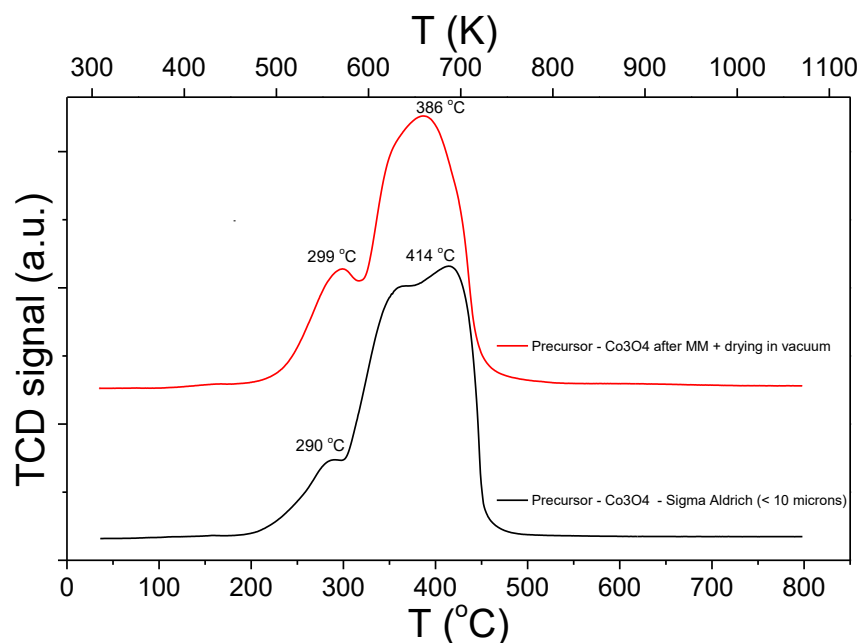


Figure 50 - TPR comparison between as-purchased Co_3O_4 powder and after milling and drying process

SEM images confirmed the reduction of the particle size and their better distribution after drying process (Figure 51). Therefore, the effectiveness of the milling process was verified.

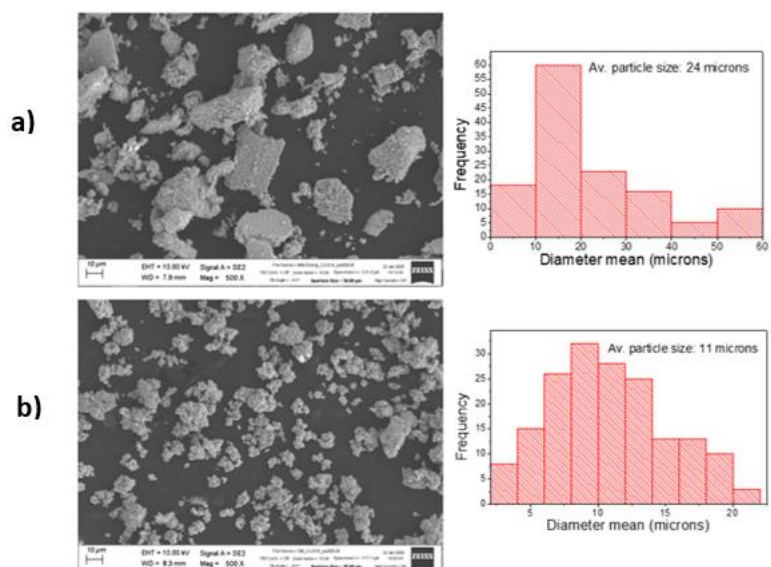


Figure 51 - Co₃O₄ particle size: a) as-purchased 24 µm, b) after drying process 11 µm

Effect of the support (Al₂O₃):

There is a notable effect of the support on the thermal behavior of the Co₃O₄ upon reduction under hydrogen atmosphere (Figure 52). The temperature of the whole process is markedly reduced in about 100 °C (500 to 400 °C). The first thermal event is less pronounced and narrower for the catalyst (Co/α-Al₂O₃). This fact can be only attributed to the partial reduction of the oxide, so not all of it is accessible. As seen before (Figure 46), the catalytic layer of the Co₃O₄ is about 60 µm and then after the reduction is reduced down to 20 µm. As the TPR shows there is a notable temperature decrease after the impregnation of the catalyst on the support with respect to the bulk Co₃O₄ after the same process of milling plus drying in vacuum as the impregnated one. This suggests that the small thickness of the Co₃O₄ layer ease its reduction by making H₂ more accessible and thus leading to the notable reduction of temperature.

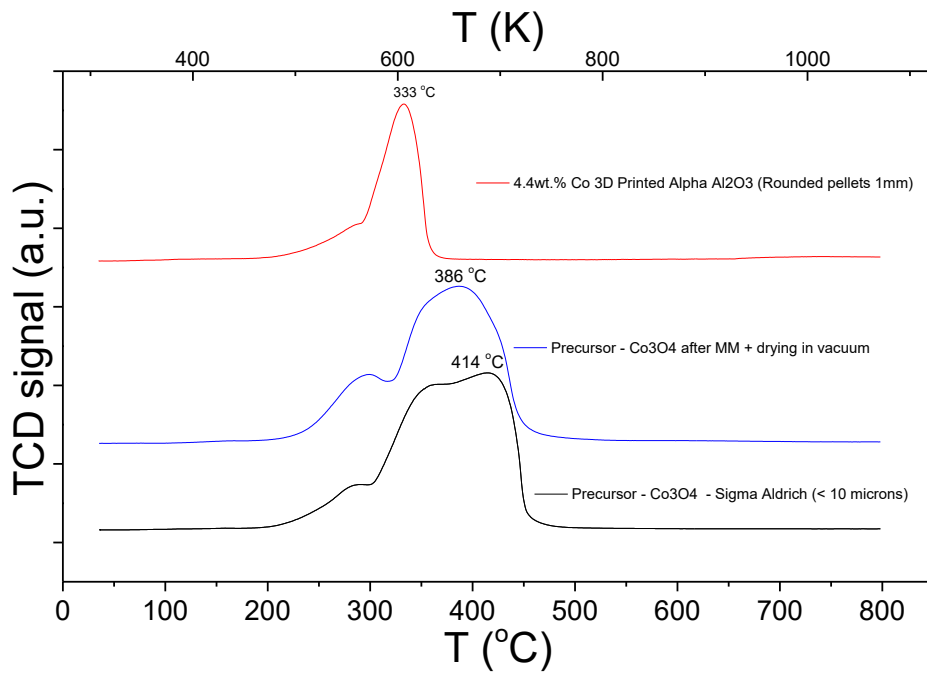


Figure 52 - Effect of the support on TPR profile

Effect of the promoter (Re):

A solution of rhenium and water was prepared as it was done with the catalyst preparation to know possible variations of the rhenium composition. Its composition after the process provides useful information to include in the analysis. As seen in the XRD results (Figure 53), Re remains reduced upon water solution and the rotary vacuum drier process. Re does not get oxidized upon the synthesis process because its oxidation temperature is between 600 and 1400 °C. Therefore, TPR is not influenced by Re reduction because it is already in the reduction state.

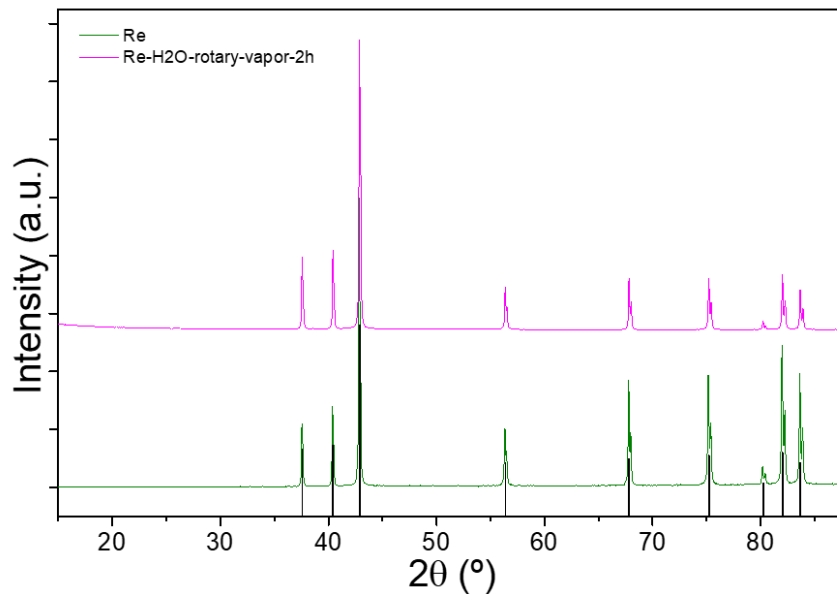


Figure 53 - XRD of the promoter (Re) upon the synthesis process

When comparing TPR profiles of the catalysts with and without the promoter a similar behavior was found (Figure 54). There was not significant difference on the reduction temperature. However, rhenium mainly improves the degree of active species for the catalytic activity (Table 4).

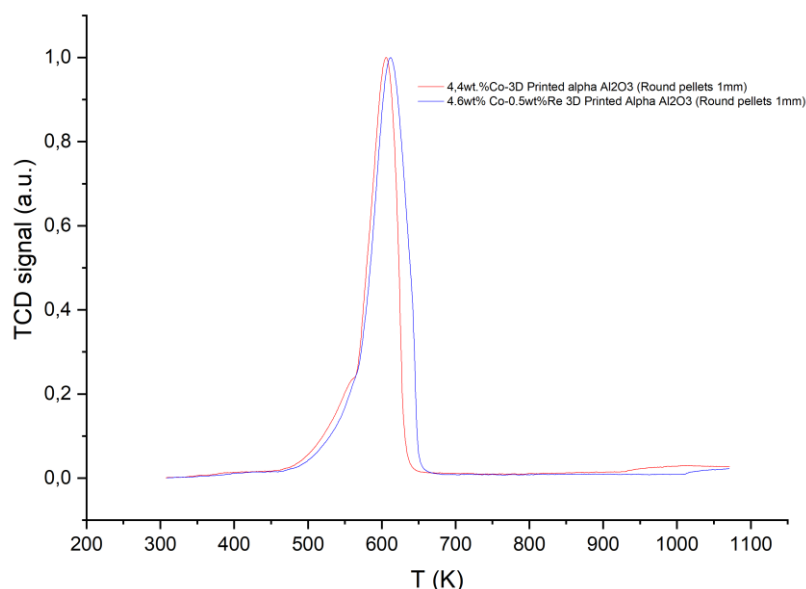


Figure 54 - TPR of catalyst with and without promoter

Table 4 - Comparative values of catalyst with and without promoter

Catalyst	%Dispersion of active species (TPO)	Crystallite size of Co ^o (111) [nm]	BET area [m ² /g]	Pore size [nm]	Pore volume [cm ³ /g]
4.4 wt.% Co/Al ₂ O ₃	34	30	1.6041	40.49	0.0135
4.6 wt.% Co-0.5wt.% Re/Al ₂ O ₃	48	24	1.5807	35.76	0.0115

Comparison with a commercialized catalyst:

TPR profiles of our catalyst and commercialized catalyst (from Johnson Matthey Chemicals) were compared to validate the measurement done. Here follow the four catalysts involved:

- a 16wt.% Co/ γ -Al₂O₃ (Johnson Matthey Chemicals/Round pellets)
- b 16wt.% Co/ α -Al₂O₃ (Johnson Matthey Chemicals/Round pellets)
- c 4.4wt.%Co/3D-Printed α -Al₂O₃ (Round pellets ~1mm)
- d 4.6wt.% Co-0.5wt%Re/3D-Printed α -Al₂O₃ (Round pellets ~ 1mm)

Both commercialized catalysts showed more than one peak (Figure 55). The first peak can be attributed to the precursor used for the synthesis of the catalyst, which presumably would be cobalt nitrate. The impregnation method can form nitric oxide that are reduced during the TPR. The other two peaks are on the other hand related to the cobalt reduction; first into CoO than into Co^o. As we saw previously, in our case the two reductions are overlapped.

However, the reduction temperature range of our catalyst is in agreement with the commercial catalyst supported in α -alumina (below 400 °C). Instead, the catalyst supported in γ -alumina displays higher reduction temperature.

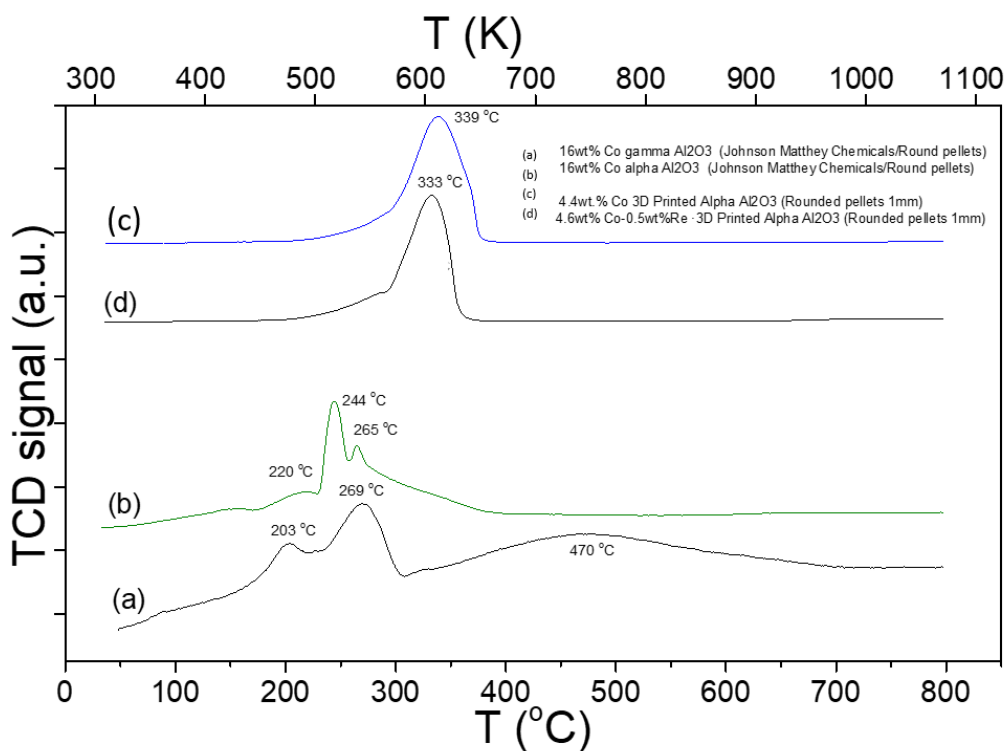


Figure 55 - TPR comparison with commercialized catalysts (Johnson Matthey Chemicals: <https://matthey.com/en>)

4.3.4 Conclusions

An eggshell catalyst was successfully synthesized by impregnation of cobalt catalyst over the alumina support with proper attachment between catalyst and support. The milling process favoured the dispersion of cobalt in the mixture and reduced the particle size. XRD results showed the presence of FCC phase of active metal cobalt Co⁰ with nanometric crystalline sizes and the alumina support did not participate to the reduction. The deposition of the Co₃O₄ on the surface of the alpha alumina pellets in the form of a thin layer influences the temperature of reduction, leading to a complete reduction of Co₃O₄ to Co below 400 °C. Moreover, Re promotes the availability of active site of Co⁰. From TPO analyses it was found an increase of 14 % of active species by adding just 0.5 wt.% of Re.

Finally, the reduction temperature of our catalyst was in agreement with α -alumina commercialized catalyst even if it shows more than one thermal event due to the different precursor used.

4.4 EVALUATION OF THE PERFORMANCE OF THE 3D-PRINTED BASED CATALYST

This chapter is about the experimental test and modelling of the synthesized Co-promoted Re-3D-printed α -Al₂O₃ in a fixed bed reactor for Fischer-Tropsch synthesis of long-chain hydrocarbons. The setup of the reactor setup is described in section 3.4. For the modelling of the reactor based on finite element simulations (FEM), a pseudo-homogeneous model is proposed by using COMSOL Multiphysics software. In a pseudo-homogeneous model, the solid-to-fluid heat and mass transfer resistances are neglected (i.e. the catalyst surface is assumed to be exposed to bulk fluid conditions, and the intraparticle diffusion effects are not considered). The model is validated by comparing them to the experimental results. All taken assumptions for neglecting intraparticle and interparticle heat and mass transfer constraints are validated *via* the application of different criteria.

4.4.1 Optimization of the parameters in the FBR

The reactor was filled with the catalyst rounded pellets forming a porous bed in the middle of the reactor. Taking into account the maximum syngas flow of the setup (140 ml/min of syngas), 80 to 150 mg of catalytic active species is required to have proper signals for the gas chromatography of the light hydrocarbons (< C+5). Based on the TPO analyses shown in chapter 4.3.2, 2.2 wt% of Co active catalytic species is available in the obtained catalyst. Thus, the total amount of catalyst introduced in the reactor was 5 g. Moreover, 5 g of silicon carbide (SiC) was added to assure an homogeneous temperature profile inside the bed of the reactor. SiC has high thermal conductivity and doesn't participate to the reaction because it is quite inert. The amounts of 5 g of catalyst + 5 g of SiC in a 9 mm reactor of internal diameter, a high of the bed of 60 mm was obtained, which represents the maximum height of the bed because of the presence of internal thermocouple.

Before starting the analysis of the catalyst's performance, the reactor was tested and prepared:

1. **Leak test** was firstly carried out under a flow of nitrogen at 20 bar and room temperature for 40 minutes to see the stability of the system.
2. The catalyst, in form of cobalt oxide, was **reduced in Co⁰** as it was done in the TPR. For this purpose, a flow of hydrogen of 100 Nml/min was used first for 4 h at 120 °C and then for 11 h at 380 °C.
3. **Blank test** was carried out with 200 Nml/min of a flow composed by 70% syngas (H₂/CO ratio equal to 1.7) and 30% N₂ to evaluate reference parameters.

After these preparation steps, the measurements begin. In the beginning, several measurements were done changing the temperature, the pressure and the inlet flow to find the most suitable condition to have about 50% of syngas conversion and 80% of C⁵⁺ selectivity. Gas and liquid chromatography were used to know the hydrocarbons compounds and their quantity.

(Figure 56) shows the values obtained from the gas chromatography as a function of the time of stream (TOS). In the upper part of the graph, the applied conditions are exhibit. The flow is expressed as gas

hourly space velocity GHSV, i.e. the ratio between the inlet flow of syngas in normal condition and the mass of catalyst (4.10).

$$GHSV = \frac{\dot{F}_{syngas}}{m_{catalyst}} \quad (4.10)$$

The selectivity of a general product (hydrocarbons from C¹ to C⁴ and CO₂) is calculated as ratio of its concentration and the difference of CO concentration between inlet and outlet (4.11). The hydrocarbons with chain higher than 4 are coupled together as C⁵⁺ (4.12).

$$S_{C^{5+}} = 100 - \sum_{n=1}^4 S_{C_nH_{2n+2}} - S_{CO_2} \quad (4.11)$$

$$S_{product} = \frac{C_{product}}{C_{CO}^{in} - C_{CO}^{out}} \cdot 100 \quad (4.12)$$

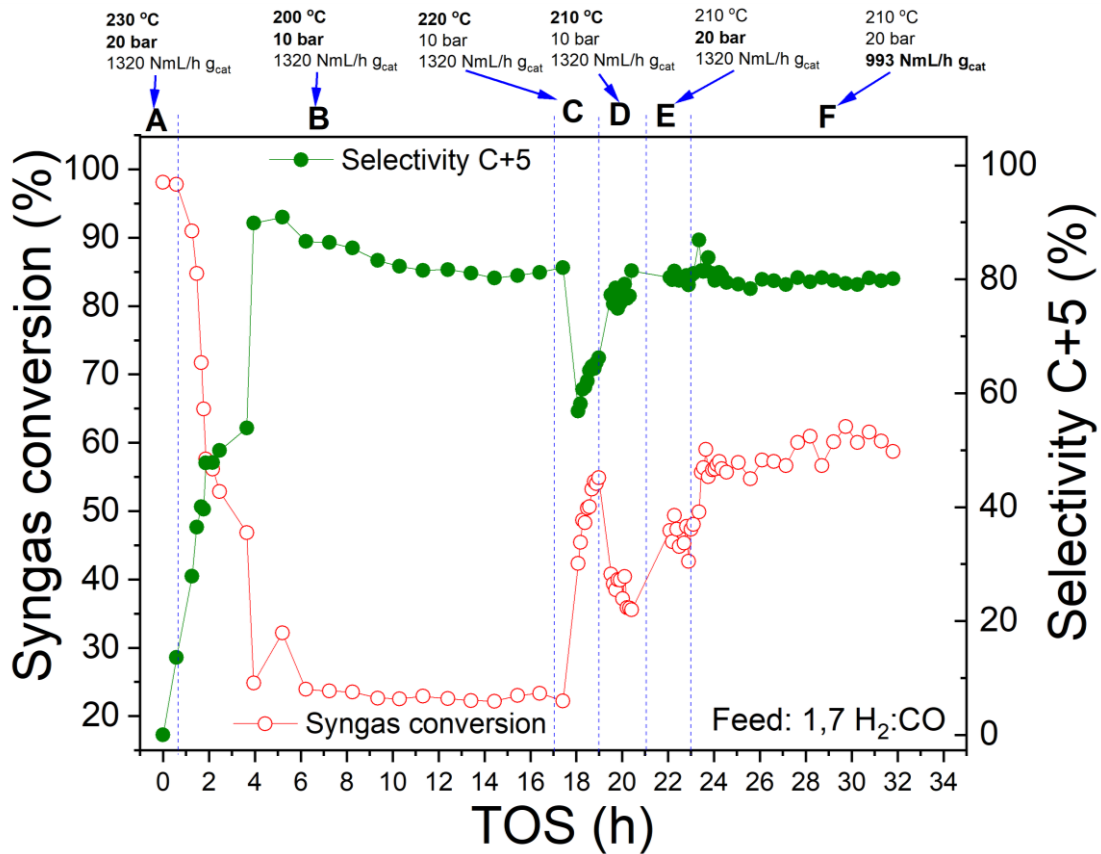


Figure 56 - Selectivity and conversion obtained during the experiment

By varying the parameters, it was observed that:

- Increasing the temperature (B→D→C), the selectivity decreases and the conversion rises, in agreement with the literature [3]. Moreover, the WGS exhibit activity at 220 °C with a small production of CO₂

- Changing the pressure (D→E), it doesn't cause a considerable change in the selectivity, and the conversion shows a slight increment.
- Reducing the flow (E→F), the residence time of the syngas inside the reactor is higher. As a consequence, the conversion of CO increase without altering the selectivity that depend more on the pressure and temperature.

The condition of **210 °C, 20 bar** and **993 Nml/(h*g_{cat})** was selected because the **conversion** was **55%** and the **selectivity** was about **81%** (these values were calculated as average of the last 5 measurements).

Once the suitable parameters were found, the stability of the reactor was controlled leaving the reactor running. In (Figure 57) the trend of selectivity is quite flat after 100 min instead the conversion needs more time to reach a more stable behaviour. This means that the conversion is more affected by the oscillation of the reactor parameters. In any case the conversion remains within in a small range, hence system stability is demonstrated.

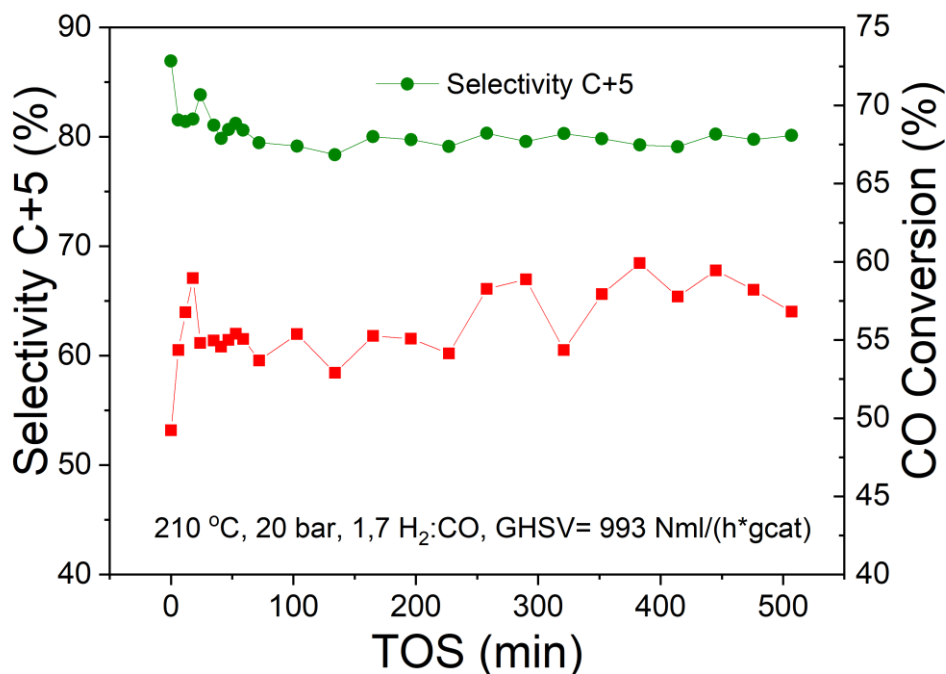


Figure 57 - Stability of selectivity and conversion with optimized parameters

The value of CO rate was calculated under the optimized condition and plotted as a function of the TOS (Figure 58). The following equation was used considering the flow of CO (\dot{F}_{CO}), the CO conversion (X_{CO}) and the catalyst mass ($m_{catalyst}$):

$$r_{CO} = \frac{X_{CO} \cdot \dot{F}_{CO}}{m_{catalyst}} \quad (4.13)$$

The catalyst mass and the flow of CO are constants, so the CO rate follows the same trend of the conversion. After 200 min the trend becomes stable and the average value is **8.7 e⁻⁵ mol_{co}/(min*g_{cat})**.

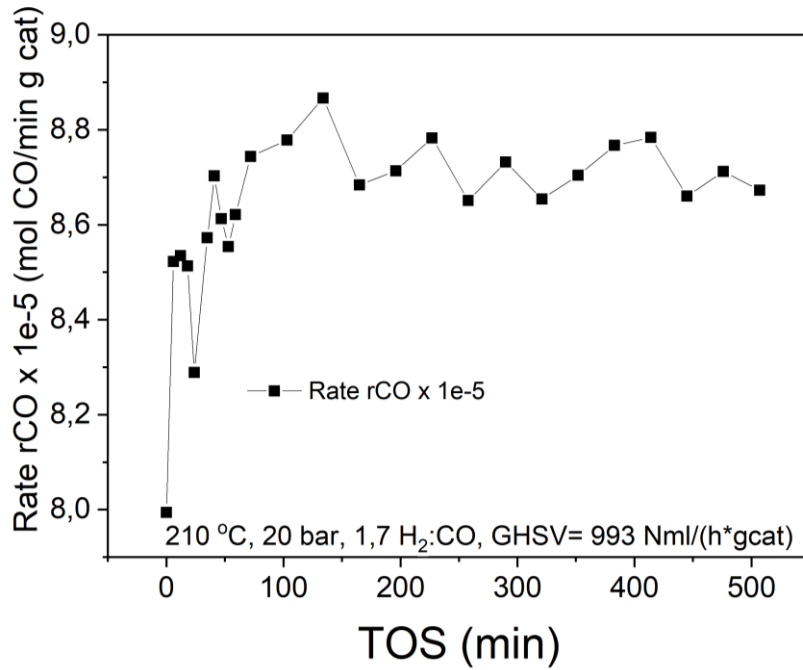


Figure 58 - Stability of the CO rate with the optimized parameters

The setup of the reactor allows to separate the liquid-solid from the gas products and they are recovered into a vessel (Figure 59) used in the liquid chromatography to know the percentage of each compound.

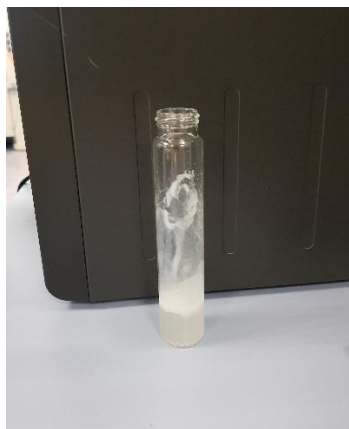


Figure 59 - Specimen with the liquid products of the reaction

(Table 5) shows the weight of each compound and the percentage based on the total amount. The liquid is mainly composed of n-paraffins with 46.43% and 38.43% of diesel and wax respectively. Olefins exhibit a small portion of 6.36 % and alcohols are negligible. These values confirm the high production of heavy hydrocarbon and the proper performance of the eggshell catalyst.

Table 5 - Results from the liquid chromatography

			Weight	wt(%)
PARAFFINS (C _n H _{2n+2})	n-PARAFFINS	Lights (C8-C11)	0.155319	5.17
	90.03 %	Diesel (C12-C18)	1.396033	46.43
		Wax (C19+)	1.155458	38.43
	ISO-PARAFFINS	Lights (C8-C11)	0.107657	3.58
	3.58 %	Diesel (C12-C18)	0.000000	0.00
		Wax (C19+)	0.000000	0.00
OLEFINS (C _n H _{2n})	6.36 %	C8-C11	0.191149	6.36
		C12-C18	0.000000	0.00
		C19+	0.000000	0.00
ALCOHOLS			0.001076	0.04
SUM			3.006691	

4.4.2 FBR model

A pseudo-homogeneous model was developed neglecting internal and external constraints of the catalyst and the reactor. The following assumption were done:

- Eggshell pellets with a thin catalytic layer to neglect the internal diffusion effects
- Homogeneous temperature inside the volume of the pellets
- Appropriate inflow velocity and pellets diameter to enhance the external mass transfer
- Uniform temperature gradient between fluid and surface of the pellets.

The experimental syngas ratio was taken for the simulation: H₂/CO=1.7. The syngas flow reaches the bed after passing through 4 cm of reactor length. Hence, it can be considered that the temperature of the syngas is the same as the desired temperature of the bed. Knowing the condition at the beginning of the bed and the symmetry of the reactor, the model was simplified considering only the catalytic bed and a 2D axisymmetric geometry. A physical controlled triangular extremely fine mesh was set to avoid deviation on the results and satisfy the convergence criterion (Figure 60). The thickness of the reactor wall was not considered as it is composed of stainless steel with high thermal conductivity and neglectable temperature gradient.

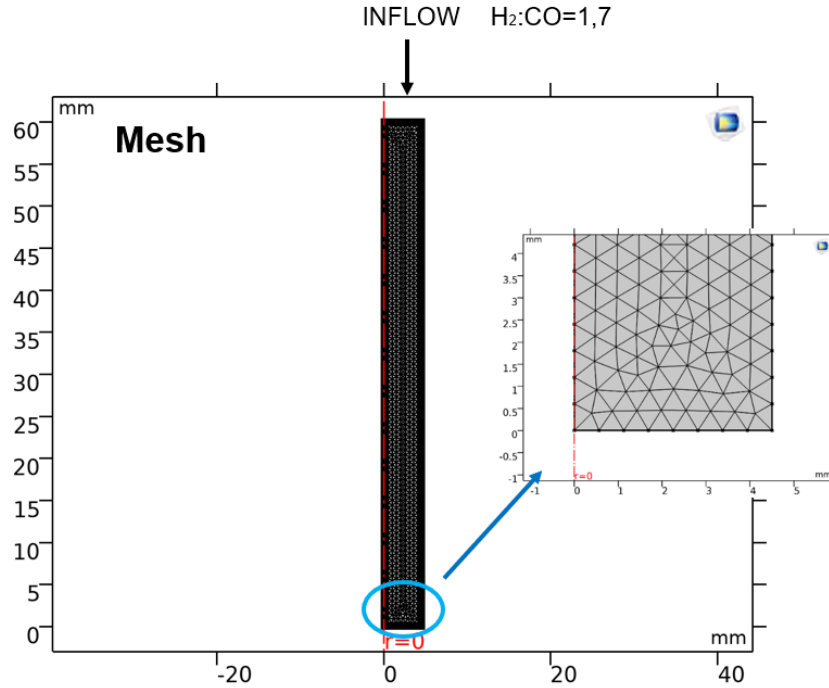


Figure 60 - Geometry and mesh of the model (2D-axial symmetric geometry)

After the definition of the domain, COMSOL interface allows to set the material properties and the physics that describe the model. The **steady state** condition of the reactor was studied applying the following modules: *Thermodynamics, Chemistry, Darcy's law, Transport of diluted species, Heat transfer in fluids and in solids.*

Thermodynamics module:

This module calculates the thermodynamic properties of the gas-liquid mixture inside the reactor using the Soave-Redlich-Kwong model equation:

$$P = \frac{RT}{V - b} - \frac{a}{(V^2 + 2bV - b^2)\sqrt{T}} \quad (4.14)$$

where a and b are parameters of the species mixture and the other are the pressure P , the temperature T , the volume V and the gas constant R .

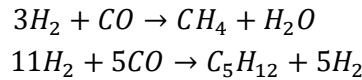
Moreover, this thermodynamic model allows to calculate the gas-liquid equilibrium between the gas reactants and products, and the generated liquid products. The viscosity and density of the whole reactants and products mixtures is also calculated by the thermodynamic package.

Materials:

The domain was supposed to be composed of 50% alumina and 50% SiC without considering the cobalt catalytic layer because of its low amount (20 microns of catalytic layer). This assumption was taken mainly for the heat transfer. The thermodynamic properties of the alumina obtained experimentally (see section 4.1.2) and the ones of the SiC (from the library) are used for the porous bed properties.

Chemistry:

The chemical reactions and their kinetic equations are set in this module. A key issue of any reactor model is chemical kinetics. This is particularly true in the case of the FTS due to the complexity of the reaction mechanism, the very high number of chemical species involved, the multiphase character of the system, the important role of equilibrium and the interplay of chemical and transport phenomena at the catalyst pore level. In this case a simplified kinetic model was applied considering only the reaction of syngas into methane (CH₄) and into pentane (C₅H₁₂) as index of long hydrocarbon chain production (C⁵⁺). Water Gas Shift reaction was not considered because it was considered that cobalt based catalyst exhibits weak activity for the WGS at low temperature.



The rate equation of the FT synthesis (4.15) was simplified taking into account the consumption of H₂ and CO in form of concentration (C_{CO} , C_{H_2}), the kinetic constant k_{FT} and the adsorption constant k_1 of CO. Production rates of the two reactions r_{CH_4} (4.18) and $r_{C_5H_{12}}$ (4.19) are written following two specific Arrhenius laws. All the kinetic parameters and adsorption constant are given in form of Arrhenius law and the activation energy are taken from the paper [30]. The frequency factors (a,b,d,e) are instead gained from the comparison of the model with the experimental result (Table 6). These parameters are in the same range as the ones published in several works about FT reactors modelling [30]

Table 6 - Kinetic parameters of the model obtained after the comparison with the experimental results

Parameters	value	unit		
a	6.3 E+06	m ⁶ /(mol*s*kg _{cat})	$r_{FT} = \frac{k_{FT} C_{CO} C_{H_2}}{(1 + k_1 C_{CO})^2}$	(4.15)
b	39	m ³ /mol		
d	1.9 E+12	-	$k_{FT} = a \cdot \exp\left(\frac{-E_a}{RT}\right)$	(4.16)
e	3.0 E+09	-		
E_a	100	kJ/mol	$k_1 = b \cdot \exp\left(\frac{-\Delta H_b}{RT}\right)$	(4.17)
ΔH_b	20	kJ/mol		
E_d	81	kJ/mol	$r_{CH_4} = d \cdot \exp\left(\frac{-E_d}{RT}\right) \cdot r_{FT}$	(4.18)
E_e	49	kJ/mol		
			$r_{C_5H_{12}} = e \cdot \exp\left(\frac{-E_e}{RT}\right) \cdot r_{FT}$	(4.19)

The selectivity was calculated as the ratio between the concentration of product at the reactor output section without considering the water production (4.20):

$$S_{C^{5+}} = \frac{C_{C_5H_{12}}}{C_{C_5H_{12}} + C_{CH_4}} \quad (4.20)$$

The conversion of carbon monoxide was calculated as the amount consumed over the initial amount of CO (4.21):

$$X_{CO} = \frac{C_{CO_in} - C_{CO_out}}{C_{CO_in}} \quad (4.21)$$

Darcy's law:

The **Darcy's Law** was used to simulate fluid flow through the porous bed. It can be used when the velocity of the flow is low enough to have a Reynolds number less than one. As consequence, the pressure gradient and the gravity field are the main driving force that changes the velocity field in the porous media. The dependent variable is the pressure and the equation is:

$$u = -\frac{k}{\mu}(\nabla P + \rho g \nabla D) \quad (4.22)$$

where u is the fluid velocity, k is the porous bed permeability, μ is the fluid dynamic viscosity calculated by thermodynamics interface, ∇P is the pressure gradient, ρ is the fluid density, g is the gravitational acceleration and ∇D is the direction of the gravity.

In this case the gravity effect was not considered and combining the (4.22) with the continuity equation in steady state the governing equation is given by the (4.23):

$$\nabla \cdot \left(-\rho \cdot \Delta P \cdot \frac{k}{\mu} \right) = Q_m \quad (4.23)$$

where Q_m is the mass source.

No slip condition (4.24) was applied on the reactor wall. The inlet velocity and the outlet pressure were fixed at constant value.

$$-n \cdot \rho u = 0 \quad (4.24)$$

Based on the assumption that the porosity is homogeneous in the bed, the Benyahia and O'Neill empirical equation was used to calculate the porosity of the bed [31]:

$$\varepsilon_{bed} = 0.39 + \frac{1.74}{\left(1.14 + \frac{D}{d_p}\right)} \quad 1.5 \leq \frac{D}{d_p} \leq 50 \quad (4.25)$$

where $\frac{D}{d_p}$ is the ratio between the diameter of the reactor D and the pellet diameter d_p . There are no significant variations for value of this ratio higher than 10 and the minimum porosity that can be obtained reducing the pellet diameter is around 37 %.

With the ε_{bed} and the Carman-Kozeny equation, the permeability of porous bed k was calculated (4.26):

$$k = \frac{\varepsilon_{bed}^3}{180 \cdot (1 - \varepsilon_{bed})^2} \cdot d_p^2 \quad (4.26)$$

180 comes from the assumption of spherical solid pellets with the same surface area.

Transport of Diluted Species:

The **Transport of Diluted Species** interface is used to calculate the concentration field of chemical compounds. The physic is based on the mass transport equation of each species i in porous bed with

the diffusion by Fick's law (4.28), convection mechanism ($u \cdot \nabla C_i$) and the reaction rate R_i as driving forces. Diffusion limitation inside the catalyst occurs and only the surface of the catalyst was considered as reacting domain. This internal constrain is included in the model taking into account the porosity of the bed ε_{bed} in the equation (4.27).

$$\nabla \cdot J_i + u \cdot \nabla C_i = \varepsilon_{bed} \cdot R_i \quad (4.27)$$

$$J_i = -D \cdot \nabla C_i \quad (4.28)$$

As boundary condition the inflow concentration of the species was set constant and the condition of no diffusion transport on the outlet was applied (4.29).

$$-D \cdot \nabla C_i = 0 \quad (4.29)$$

Heat Transfer in fluids and solid:

The temperature distribution inside the reactor is fundamental to discover possible hot spot in the system. A plug flow model with axial and radial dispersion in porous media was applied. The main mechanisms of the heat transport are convection due to the reacting flow and conduction through the porous bed. Radiative transport is negligible for the temperature range at which the system operates. Moreover, the reaction is highly exothermic and generate heat meanwhile the reactants are consumed. Thus, the governing equation can be written as:

$$\rho \cdot c_p \cdot u \cdot \nabla T - \nabla \cdot (k_{eff} \cdot \nabla T) = Q \quad (4.30)$$

The first term account to the convection and depend on the fluid velocity, the second term to the conduction and Q is the heat source produced by the reactions. The heat source is provided by the reaction and depend on the rate and enthalpy of the reactions (4.31).

$$Q = -(r_{CH_4} \Delta H_{CH_4} + r_{C_5H_{12}} \Delta H_{C_5H_{12}}) \quad (4.31)$$

The domain was considered as homogeneous body with mixture properties of the solid and liquid. Thus, density ρ , specific heat capacity c_p and thermal conductivity k_{eff} are calculated as weighted average of each material property (4.32).

$$k_{eff} = (1 - \varepsilon_{bed}) \cdot (0.5 \cdot k_{Al_2O_3} + 0.5 \cdot k_{SiC}) + \varepsilon_{bed} \cdot k_{fluid} \quad (4.32)$$

The reactor is located inside an oven to control the temperature of the wall. For this reason, external natural convection with air was applied as boundary condition of the wall:

$$k_{eff} \cdot \frac{\partial T}{\partial r} \Big|_{r=R} = h_{air} \cdot (T - T_{air}) \quad (4.33)$$

where h_{air} is the heat transfer coefficient between air and wall.

Danckwerts boundary condition (4.34) is applied at inlet knowing the upstream temperature of the flow. This inflow condition is often similar to a temperature condition. However, the low velocity allows heat transfer in the opposite direction of the flow and a small variation of the temperature occurs. This boundary condition estimates the heat flux through the inlet boundary calculating the enthalpy (4.35):

$$-n \cdot q = \rho \cdot \Delta H \cdot u \cdot n \quad (4.34)$$

$$\Delta H = \int_{T_{upstream}}^T c_p \cdot dT \quad (4.35)$$

At the outlet boundary the only heat transfer occurring is by convection. The temperature gradient in the normal direction is zero:

$$-n \cdot q = 0 \quad (4.36)$$

Results:

The optimized condition found experimentally (see paragraph 4.4.1) were applied to the model giving the following results. (Figure 61) shows the temperature and heat source generated inside the reactor. The heat generated by the reaction is higher at the beginning due to the high concentration of reactants. Nevertheless, the presence of the SiC guaranties a radial and axial homogeneity of the system temperature avoiding hot spots. Therefore, the system has isothermal behaviour.

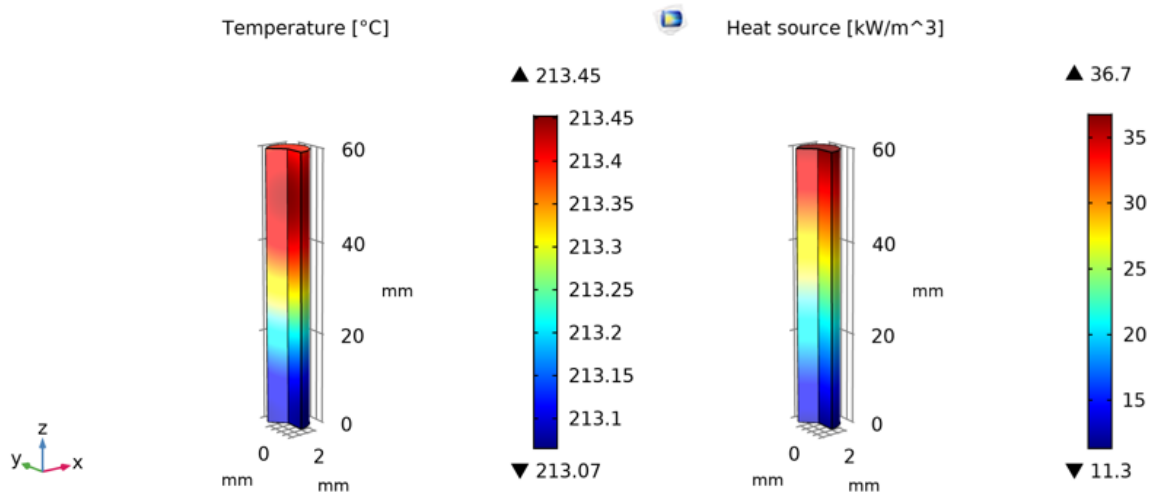


Figure 61 - temperature and heat source inside the reactor in the optimized condition

The Pressure and velocity field are reported in (Figure 62). The reactions increase the number of mole and, as consequence, the resulting drop of pressure is very low. Moreover, the dynamic viscosity of the fluid increases due to the production of liquid hydrocarbons. Thus, the mixture has more difficulty to pass through the porous bed and the axial velocity decreases from the inlet to the outlet.

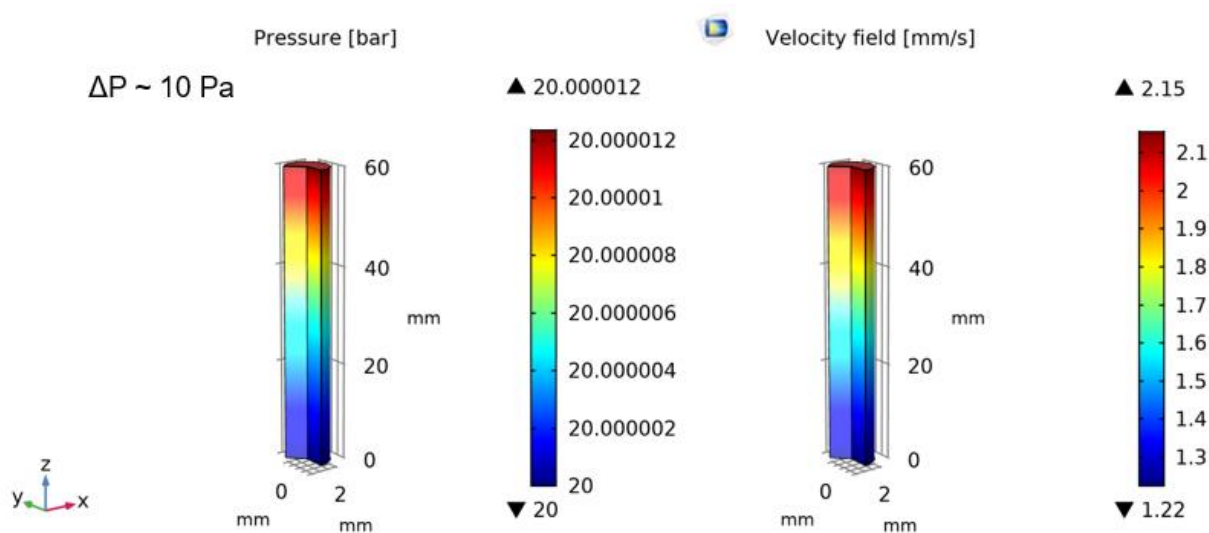


Figure 62 - pressure and velocity inside the reactor in the optimized condition

The concentration of the reactants along the reactor length is shown in (Figure 63). The stoichiometry of the reaction provides a consumption of hydrogen higher than the carbon monoxide. Starting from 15 mol/m^3 of H_2 and 9 mol/m^3 of CO , the concentration of the two reactants at the outlet of the reactor is nearby 4 mol/m^3 . These values provide a **conversion of CO of 55%**.

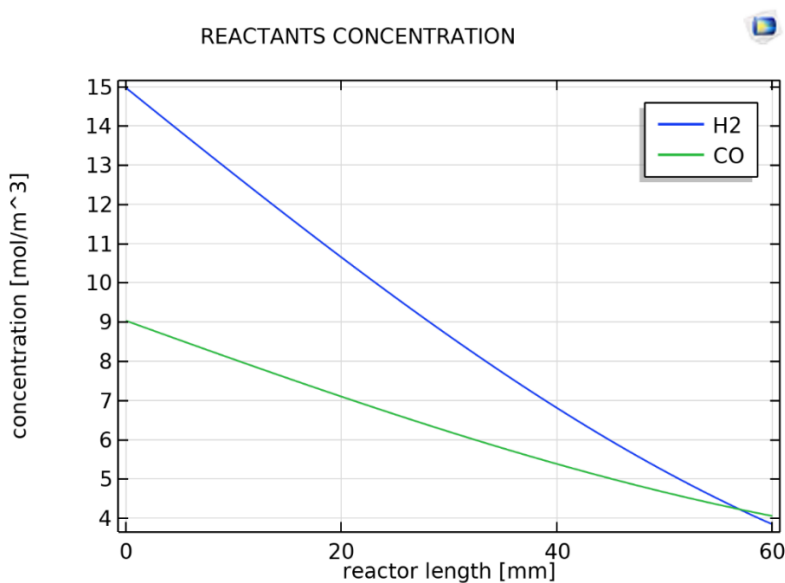


Figure 63 – Reactants concentration along the axial direction at $r=0$

Due to the absence of the WGS reaction the water is the main product in the reactor with an outlet concentration of 5 mol/m^3 (Figure 64). Water exhibits a positive effect in the hydrogenation of primary olefins into secondary paraffins providing high selectivity of C^{5+} [32]. The outlet CH_4 concentration 0.22 mol/m^3 and the one of C^{5+} 0.95 mol/m^3 give a **selectivity of 81 %**. Both conversion and selectivity are coherent with the experimental data.

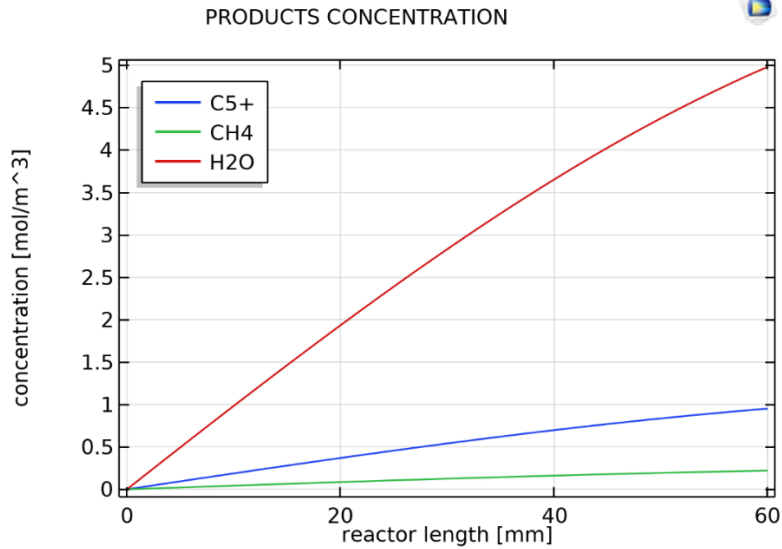


Figure 64 – Products concentration along the axial direction at $r=0$

4.4.3 Model validation

Mass transport and heat transfer assumptions were taken in order to simplify the model. Therefore, it is important to verify the validity of these hypothesis to avoid deviation from the reality. The real behaviour of the catalyst's bed is affected by mass and heat transfer internal and external limitations. In this section, the validation of the taken assumptions and the validation of the whole modelling are developed. All the calculations referring to the mass and heat transfer internal and external constraints are shown in the Appendix at the end of the thesis.

Internal limitations of the catalyst:

1. **Diffusion limitations:** The internal diffusion in the pores of the catalyst (pellet) limits the reaction rate.
2. **Heat transfer limitations:** Temperature gradients inside the catalyst pellet

External limitations of the reactor:

3. **Diffusion limitations:** The mass transfer from the bulk gas to the catalyst surface limits the reaction rate.
4. **Heat transfer limitations:** Temperature gradients between the bulk gas and the surface of the catalyst pellet

Internal diffusion limitations:

The diffusion of the gas through the pore of the catalyst can limit the reaction rate if the velocity of the reaction is much higher than the velocity of diffusion. In the eggshell catalyst the thin layer of catalyst allows to neglect this effect. In order to validate of this hypothesis the Weisz-Prater criterion was applied to estimate the influence of diffusion mechanism through the catalyst pore on the reaction rates [33]:

$$C_{WP} = \frac{-r'_{CO}(obs) \cdot \rho_c \cdot R^2}{D_{eff,CO} \cdot C_{CO}} \quad (4.37)$$

where $r'_{CO}(obs)$ is the rate observed of the CO, ρ_c is the density of the catalyst (Co density= $8 \cdot 10^6$ g/m³), R is the catalyst sphere radius, $D_{eff,CO}$ is the effective diffusion coefficient of CO into the paraffins (as a reference n-octacaine was taken C₂₈H₅₈) and C_{CO} is the concentration at the particle surface. If the value of $C_{WP} \ll 1$ the diffusion limitation can be neglected. It is important to mention that CO is taken reactant and not H₂. CO is regarded as rate-limiting reactant for the kinetic expression herein applied [34].

The radius of the catalyst is not coincident with the radius of the pellet because in the eggshell catalyst the cobalt is located only on the surface and a characteristic length L_{cat} was calculated as [22] :

$$L_{cat} = \left(\frac{R}{3}\right) * \left[1 - \left(1 - \frac{\delta}{R}\right)\right] \quad (4.38)$$

The effective diffusion coefficient of the CO was obtained as a function of the porosity of the catalyst $\varepsilon_{catalyst}$ and the tortuosity τ :

$$D_{eff,CO} = D_{CO,WAX} \cdot \left(\frac{\varepsilon_{catalyst}}{\tau}\right) \quad (4.39)$$

the diffusion coefficient $D_{CO,WAX}$ as a function of the temperature was taken from the one of CO into a large chain wax (n-C₂₈H₅₈), which would represent the case of C⁵⁺ [35]:

$$D_{CO,WAX} = 5.584 e^{-7} * \exp\left(-\frac{1786.29}{T}\right) \quad (4.40)$$

The GHSV is the main factor that influences the final value of C_{WP} (Table 7). Increasing the GHSV the diffusion limitations become considerable. In the range used the criterion is fulfilled and the assumption done is valid.

Table 7 – Parameters for internal diffusion limitations

P (bar)	T (°C)	r _{CO} (mol/s gcat)	L _{cat} (m)	GHSV (NmL/h gcat)	C _{wp}
10	200	1.90E-06	0.0006	1320	0.194
10	220	2.37E-06	0.0006	1320	0.233
20	210	1.44E-06	0.0006	993	0.064

Internal heat transfer limitations:

The internal temperature gradient inside the pellets occur when the thermal conductivity of the catalyst is very low and when diffusion limitation occurs. The presence of temperature gradient changes the value of the rate that is calculated at the surface temperature of the catalyst. If the following criteria, taken from the literature [36], is satisfied it is possible to neglect the temperature gradient and consider the temperature of the pellet homogeneous.

$$\gamma \cdot \beta_i \cdot C_{WP} = \left(\frac{E_A}{RT}\right) \cdot \left(\frac{(-\Delta H_r) \cdot D_{eff,CO} \cdot C_{CO}}{\lambda_{cat,eff} \cdot T}\right) \cdot \left(\frac{R_{CO} \cdot \rho_c \cdot L_{cat}^2}{D_{eff,CO} \cdot C_{CO,s}}\right) < 0.015 \quad (4.41)$$

where γ is the dimensionless activation energy, β_i is the Prater number, T is the reaction temperature, $\lambda_{cat,eff}$ is the effective thermal conductivity of the catalyst.

The value obtained from the analysis are much lower than the limit of the criteria (Table 8). Thus, it is possible to consider the temperature homogeneous inside the pellets at the condition adopted.

Table 8 - Parameters for internal heat transfer limitations

P (bar)	T (°C)	GHSV (NmL/h g _{cat})	C _{wp}	γ	β	$\gamma * \beta * C_{wp}$
10	200	1320	0.194	25.429	6.29E-10	3.11E-09
10	220	1320	0.233	24.397	6.63E-10	3.77E-09
20	210	993	0.064	24.902	1.45E-09	2.32E-09

External diffusion limitation:

Mass transport from the bulk gas to the catalyst surface limits the reaction rate if the diffusion mechanism is faster than the reaction mechanism. However, adopting the appropriate velocity and particle diameter, the mass transfer limitation can be neglected. The criteria used to verify the assumption is the Mears criterion [37]:

$$MR_{diff} = \frac{-r'_A(obs) \cdot \rho_b \cdot L_{cat}}{k_c \cdot C_{CO}} < 0.15 \quad (4.42)$$

where ρ_b is the bulk density of the bed, k_c is the mass transport coefficient obtained from the following correlation [23]:

$$k_c = \left[\frac{U \cdot d_p \cdot \rho_b}{\mu \cdot (1 - \varepsilon_{bed})} \right]^{\frac{1}{2}} \cdot \left[\frac{\mu}{\rho \cdot D_{AB}} \right]^{\frac{1}{3}} \cdot \left[\frac{D_{AB} \cdot (1 - \varepsilon_{bed})}{d_p \cdot \varepsilon_{bed}} \right] \quad (4.43)$$

where U is the superficial gas velocity through the bed, ρ is the fluid viscosity, D_{AB} is the gas-phase diffusivity.

In (Table 9) there are the results of the calculation. The criterion is respected for each condition validating the proposed hypothesis.

Table 9 – Mears number parameters for external diffusion limitation

P (bar)	T (°C)	r _{CO} (mol/s g _{cat})	ρ_b (g/m ³)	K _c (m/s)	C _{CO} (mol/m ³)	MR _{diff}
10	200	1.90E-06	2.17E+06	2.38E-03	95.5	1.09E-02
10	210	2.37E-06	2.17E+06	2.50E-03	91.6	1.35E-02
20	220	1.44E-06	2.17E+06	1.06E-03	187.0	9.47E-03

External heat transfer limitation:

In experimental fixed bed reactors with heat exchange at the wall, the temperature between the external surface of the pellets and the adjacent fluid can be different due to the high exothermic reaction. The intrusion of gradients can cause variation of the kinetic behaviour respect to the ideal isothermal. Consequently, the system requires criteria to determine heat transport limitations in the reactor domain. A criterion to analyze this effect was developed by Mears [38]:

$$MR_{heat} = \left| \frac{\Delta H_r \cdot (-r_A(obs)) \cdot \rho_b \cdot L_{cat} \cdot E_A}{h \cdot T^2 \cdot R_g} \right| < 0.15 \quad (4.44)$$

Where ΔH_r is the heat of the reaction, h is the heat transfer coefficient estimated by the Reynold and Nusselt numbers (...) referred to the liquid phase, R_g is the gas constant and E_A is the activation energy of the reaction.

$$Nu = h \cdot \frac{L_{cat}}{\lambda_{liq}} \quad Re = \frac{\rho_{liq} \cdot d_{cat} \cdot v_{liq}}{\mu_{liq}} \quad (4.45)$$

Re was 0.241 and the following Nu correlation was used:

$$Nu = 1.31 \cdot Re^{\frac{1}{3}} \cdot \frac{Pr^{\frac{1}{3}}}{\varepsilon_{bed}} \quad Pr = \frac{c_{p,liq} \cdot \mu_{liq}}{\lambda_{liq}} \quad (4.46)$$

(Table 10) shows the parameters used for the Mears criterion calculation as well as the estimated values to evaluate heat transfer limitations. The absence of heat transfer limitations was confirmed by the calculation.

Table 10 - Mears number parameters for heat transfer limitations

P (bar)	T (K)	r _{co} (mol/s g _{cat})	ΔH _r (kJ/mol)	E _a (kJ/mol)	h (kW/m ² K)	MR _{heat}
10	473	1.90E-06	165	100	1.077	2.04E-02
10	493	2.37E-06	165	100	1.077	2.34E-02
20	483	1.44E-06	165	100	1.077	1.48E-02

Variation of the temperature, pressure and GHSV in the FEM model:

(Figure 65) shows the trend of the selectivity and conversion of the model in comparison with the experiment changing the operating temperature. In the range of 200-210 °C the behaviour is similar. At 220 °C it is observed a deviation from the experiment, especially in the selectivity that in the model remain high respect to the reality. This effect can be associated with the generation of CO₂ via WGS reaction that in the model was not considered and becomes important at high temperature. In fact, observing the experimental data, a significant amount of CO₂ was produced at 220 °C.

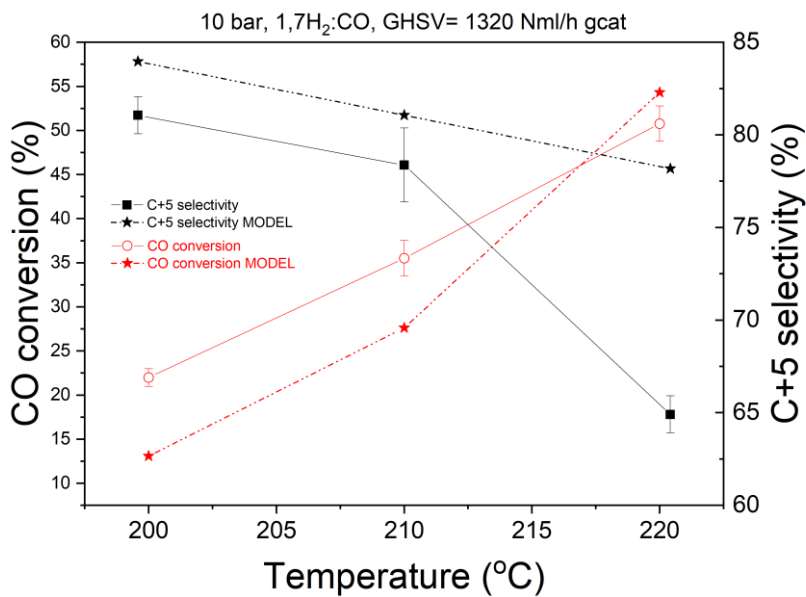


Figure 65 – comparison model-experiment changing the temperature (200-220 °C)

(Figure 66) shows a bar plot of conversion and selectivity of the model in comparison with the experiment varying the operating pressure from 10 to 20 bar. The values are very similar with no significant error, a part from the conversion at 10 bar that in the experiment is 36 ± 3 % and in the model is 29%.

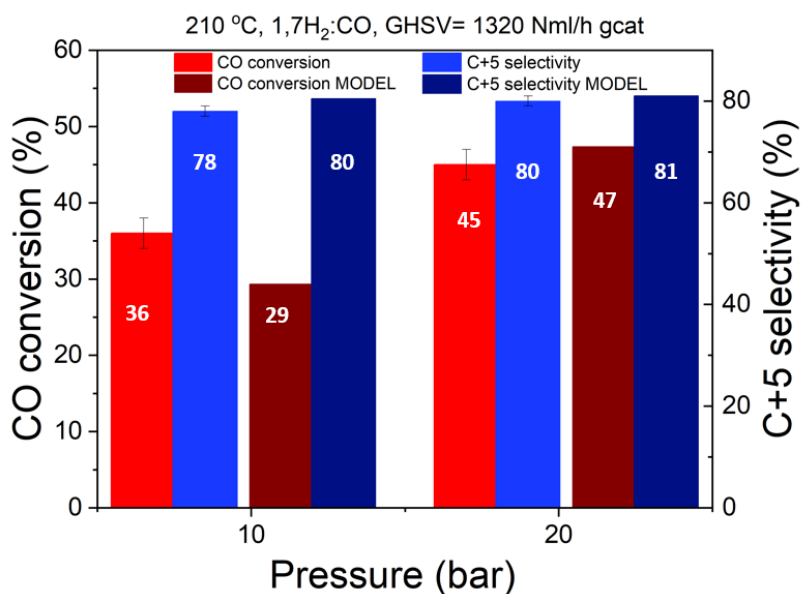


Figure 66 - comparison model-experiment changing the pressure

(Figure 67) shows a bar plot of conversion and selectivity of the model in comparison with the experiment changing the operating GHSV from 993 to 1320 Nml/(h*g_{cat}). The values are in agreement with the experiment.

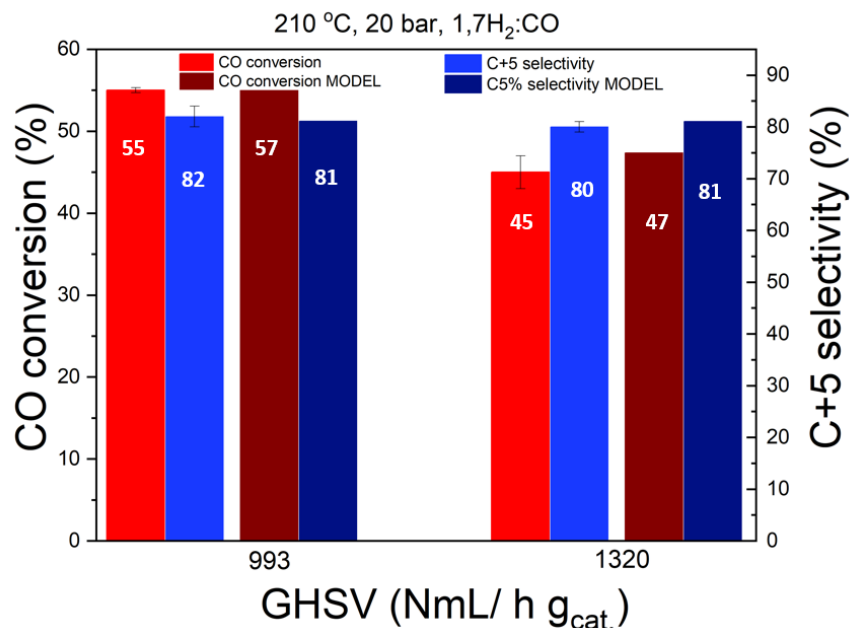


Figure 67 - comparison model-experiment changing the GHSV

4.4.4 Conclusions

The performance of the catalyst was tested inside a fixed bed reactor. Tailoring the parameters such as the temperature, the pressure, and the inlet flow allowed finding suitable conditions for conversion of CO over 50 % and selectivity of C⁵⁺ in the range of 80 %. An optimized condition was obtained at 210 °C, 20 bar, and a gas hourly space velocity (GHSV) of 933 NmL/(h*g_{cat.}) with a conversion of 55 % and a selectivity of 81%. The high production of water favors long-chain hydrocarbon formation with a 90 % production of n-paraffin. Successively, the effect of the parameters on the kinetic behavior was adequately studied. If the temperature increases, the production of methane becomes significantly higher, producing a large consumption of carbon monoxide and a reduction of the selectivity of C⁵⁺. High pressure in the reactor (20 bar) has a positive effect on the conversion and reduction of methane formation. Moreover, it favors a better heat removal, so better control of the temperature. Decreasing the GHSV, the high residence time of the reactants inside the reactor delivers less mass and heat transfer limitation, and higher conversion of CO. It was also found that there is no significant variation of the selectivity, which usually has a different behavior respect to the conversion. Finally, the hypothesis done for the development of the FEM model were verified by applying internal and external mass and heat transfer criteria. The eggshell catalyst configuration design applying a novel 3D-printing technique (SLA) and a traditional impregnation method show the potential to obtain efficient catalyst configurations *via* additive manufacturing.

5 CONCLUSIONS AND PROSPECTS

The purpose of this work was to optimize the design of Co based catalyst for FT synthesis taking advantage of the 3D-printing technology (SLA). In order to reach a trade-off between the effectiveness of the catalyst and the conditions to evaluate the catalyst in a fixed bed reactor (FBR), an eggshell of Co promoted by Re supported by 3D-printed α -Al₂O₃ with a diameter of about 1 mm and an active catalytic layer of 20 μ m was designed. The printing strategy applied allowed the production of a suitable shape of the α -Al₂O₃ support and the possibility to print a big amount of them at the same time (about 15 g). Nevertheless, the printing process has still some limitations such as the cleaning procedure for small pieces of about 300 μ m and holes with diameter less than 750 μ m. This means that the cleaning process adopted is not valid for any geometry and need further study to tune the geometry with more freedom. Preparation and impregnation of the catalyst provided a good attachment between catalyst and support. Moreover, the milling process favoured the dispersion of cobalt in the mixture and reduced the particle size. XRD results after the reduction showed the presence of FCC phase of active metal cobalt Co⁰ with nanometric crystalline sizes. However, HCP phase has much higher intrinsic activity and prefers different reaction route [27]. The Co HCP phase can be obtained by changing of the precursor, as for instance using cobalt nitrate hexa-hydrate. The phase composition, microstructure of the α -Al₂O₃ and the thin deposited oxide layer improve the active sites of Co and its catalytic activity. In fact, from the TPR analysis it was observed an improvement in the reducibility of the cobalt oxide into metal cobalt and lower reduction temperature in about 50 °C respect to the starting material). Rhenium promotes the availability of active Co⁰. From TPO analyses it was discovered an increase of 14 % of active species by adding just 0.5 wt.% of Re. However, no significant variation in the reduction temperature was observed owing to the small amount of Re added. It would be part of a future work to try different Re loading to see the influence in the reduction behavior and find its optimum amount.

The eggshell catalyst showed high performance in the fixed bed reactor with a conversion of 81% and selectivity of 55% at 210 °C, 20 bar and GHSV of 933 Nml/(h*g_{cat}). It also gives the possibility to avoid mass and heat transfer limitations that reduce the reaction rate and destroy the catalyst in short time due to the difficulty of the liquid product to go out from the pore of the catalyst. Moreover, it allowed to build a simplified model to study the kinetic behaviour of the reactor keeping realistic conditions. The model can be implemented by adding almost all the principle reactions that occur, especially the WGS that takes place at high temperature. In this way it can be used to optimize the system studying the effects of each parameter.

Finally, further work is required to try to impregnate the catalytic precursor during the 3D-printing process avoiding the impregnation step and reaching more efficient surface in terms of larger surface area and approaching to a more complex geometry just utilizing additive manufacturing.

6 REFERENCES

- [1] D. S. A. Simakov, *Renewable Synthetic Fuels and Chemicals from Carbon Dioxide Fundamentals, Catalysis, Design Considerations and Technological Challenges*. 2017.
- [2] A. Delparish and A. K. Avci, "Intensified catalytic reactors for Fischer-Tropsch synthesis and for reforming of renewable fuels to hydrogen and synthesis gas," *Fuel Process. Technol.*, vol. 151, pp. 72–100, 2016, doi: 10.1016/j.fuproc.2016.05.021.
- [3] E. Rytter, N. E. Tsakoumis, and A. Holmen, "On the selectivity to higher hydrocarbons in Co-based Fischer-Tropsch synthesis," *Catal. Today*, vol. 261, pp. 3–16, 2016, doi: 10.1016/j.cattod.2015.09.020.
- [4] A. P. Steynberg, M. E. Dry, B. H. Davis, and B. B. Breman, *Fischer-Tropsch reactors*, vol. 152. Elsevier B.V., 2004.
- [5] J. C. Ruiz-Morales *et al.*, "Three dimensional printing of components and functional devices for energy and environmental applications," *Energy Environ. Sci.*, vol. 10, no. 4, pp. 846–859, 2017, doi: 10.1039/c6ee03526d.
- [6] R. Xu *et al.*, "Effects of Ag promotion for Co/Al₂O₃ catalyst in Fischer-Tropsch synthesis," *Catal. Today*, vol. 342, no. January, pp. 111–114, 2020, doi: 10.1016/j.cattod.2019.04.004.
- [7] T. K. Das, G. Jacobs, P. M. Patterson, W. A. Conner, J. Li, and B. H. Davis, "Fischer-Tropsch synthesis: Characterization and catalytic properties of rhenium promoted cobalt alumina catalysts," *Fuel*, vol. 82, no. 7, pp. 805–815, 2003, doi: 10.1016/S0016-2361(02)00361-7.
- [8] T. Kim *et al.*, "(12) United States Patent (10) Patent No .:," vol. 2, no. 12, 2014.
- [9] P. Eur and M. Kгаа, "Ficha de Datos de Seguridad," *Toxicology*, vol. 2006, no. 1907, pp. 1–5, 2007.
- [10] F. Road and G. Town, "Product Data Sheet Type CZ Material Safety Data Type CZ," pp. 1–2, 2019.
- [11] L. Alexander and H. P. Klug, "Determination of crystallite size with the x-ray spectrometer," *J. Appl. Phys.*, vol. 21, no. 2, pp. 137–142, 1950, doi: 10.1063/1.1699612.
- [12] J. Jepsen *et al.*, "Fundamental material properties of the 2LiBH₄-MgH₂ reactive hydride composite for hydrogen storage: (I) Thermodynamic and heat transfer properties," *Energies*, vol. 11, no. 5, 2018, doi: 10.3390/en11051081.
- [13] M. Thommes *et al.*, "Physisorption of gases, with special reference to the evaluation of surface area and pore size distribution (IUPAC Technical Report)," *Pure Appl. Chem.*, vol. 87, no. 9–10, pp. 1051–1069, 2015, doi: 10.1515/pac-2014-1117.
- [14] S. Brunauer, P. H. Emmett, and E. Teller, "Adsorption of Gases in Multimolecular Layers," *J. Am. Chem. Soc.*, vol. 60, no. 2, pp. 309–319, 1938, doi: 10.1021/ja01269a023.
- [15] P. a Webb, "Introduction to Chemical Adsorption Analytical Techniques and their Applications to Catalysis," *MIC Tech. Publ.*, vol. 13, no. January, pp. 1–4, 2003.
- [16] E. P. Barrett, L. G. Joyner, and P. P. Halenda, "The Determination of Pore Volume and Area Distributions in Porous Substances. I. Computations from Nitrogen Isotherms," *J. Am. Chem. Soc.*, vol. 73, no. 1, pp. 373–380, 1951, doi: 10.1021/ja01145a126.
- [17] C. I. Méndez, J. Ancheyta, and F. Trejo, "Modeling of Catalytic Fixed-Bed Reactors for Fuels Production by Fischer-Tropsch Synthesis," *Energy and Fuels*, vol. 31, no. 12, pp. 13011–13042,

- 2017, doi: 10.1021/acs.energyfuels.7b01431.
- [18] N. M. Taher, M. Mahmoudi, and S. S. Sajjadivand, "Cobalt Catalysts Preparation and Characterization over Alumina Support for Fischer Tropsch Synthesis," *Biofuels Eng.*, vol. 2, no. 1, pp. 51–61, 2018, doi: 10.1515/bfuel-2017-0004.
- [19] V. G. Tsirelson, M. Yu. Antipin, R. G. Gerr, R. P. Ozerov, and Y. T. Struchkov, "Ruby structure peculiarities derived from X-ray diffraction data localization of chromium atoms and electron deformation density," *Phys. Status Solidi*, vol. 87, no. 2, pp. 425–433, 1985, doi: 10.1002/pssa.2210870204.
- [20] E. Rytter, Ø. Borg, B. C. Enger, and A. Holmen, "Alumina as catalyst support in Co Fischer-Tropsch synthesis and the effect of added water; encompassing transient effects," *J. Catal.*, vol. 373, pp. 13–24, 2019, doi: 10.1016/j.jcat.2019.03.013.
- [21] S. Goto and O. Matsubayashi, "Relations between the thermal properties and porosity of sediments in the eastern flank of the Juan de Fuca Ridge," *Earth, Planets Sp.*, vol. 61, no. 7, pp. 863–870, 2009, doi: 10.1186/BF03353197.
- [22] M. Mandić, B. Todić, L. Živanić, N. Nikačević, and D. B. Bukur, "Effects of Catalyst Activity, Particle Size and Shape, and Process Conditions on Catalyst Effectiveness and Methane Selectivity for Fischer-Tropsch Reaction: A Modeling Study," *Ind. Eng. Chem. Res.*, vol. 56, no. 10, pp. 2733–2745, 2017, doi: 10.1021/acs.iecr.7b00053.
- [23] N. Varde and H. S. Fogler, *Elements of Chemical Reaction Engineering*, vol. 35, no. 4. 2001.
- [24] E. Peluso, C. Galarraga, and H. De Lasa, "Eggshell catalyst in Fischer-Tropsch synthesis intrinsic reaction kinetics," *Chem. Eng. Sci.*, vol. 56, no. 4, pp. 1239–1245, 2001, doi: 10.1016/S0009-2509(00)00345-6.
- [25] E. Iglesia, S. L. Soled, J. E. Baumgartner, and S. C. Reyes, "Synthesis and catalytic properties of eggshell cobalt catalysts for the Fischer-Tropsch synthesis," *Top. Catal.*, vol. 2, no. 1–4, pp. 17–27, 1995, doi: 10.1007/BF01491952.
- [26] E. Rytter and A. Holmen, "On the support in cobalt Fischer-Tropsch synthesis—Emphasis on alumina and aluminates," *Catal. Today*, vol. 275, pp. 11–19, 2016, doi: 10.1016/j.cattod.2015.11.042.
- [27] J. X. Liu, H. Y. Su, D. P. Sun, B. Y. Zhang, and W. X. Li, "Crystallographic dependence of CO activation on cobalt catalysts: HCP versus FCC," *J. Am. Chem. Soc.*, vol. 135, no. 44, pp. 16284–16287, 2013, doi: 10.1021/ja408521w.
- [28] R. C. Reuel and C. H. Bartholomew, "The stoichiometries of H₂ and CO adsorptions on cobalt: Effects of support and preparation," *J. Catal.*, vol. 85, no. 1, pp. 63–77, 1984, doi: 10.1016/0021-9517(84)90110-6.
- [29] R. D. Jones and C. H. Bartholomew, "Improved flow technique for measurement of hydrogen chemisorption on metal catalysts," *Appl. Catal.*, vol. 39, no. C, pp. 77–88, 1988, doi: 10.1016/S0166-9834(00)80940-9.
- [30] C. G. Giovanni Chabot, Richard Guilet, Patrick Cognet, "A mathematical modeling of catalytic milli-fixed bed reactor for Fischer-Tropsch synthesis: Influence of tube diameter on Fischer Tropsch selectivity and thermal behavior," *J. Clean. Prod.*, vol. 87, pp. 303–317, 2015, doi: 10.1016/j.jclepro.2014.09.032.
- [31] Z. Guo, Z. Sun, N. Zhang, X. Cao, and M. Ding, "Mean porosity variations in packed bed of monosized spheres with small tube-to-particle diameter ratios," *Powder Technol.*, vol. 354, pp. 842–853, 2019, doi: 10.1016/j.powtec.2019.07.001.
- [32] S. Storsæter, Borg, E. A. Blekkan, and A. Holmen, "Study of the effect of water on Fischer-

- Tropsch synthesis over supported cobalt catalysts," *J. Catal.*, vol. 231, no. 2, pp. 405–419, 2005, doi: 10.1016/j.jcat.2005.01.036.
- [33] P. B. Weisz and C. D. Prater, "Interpretation of Measurements in Experimental Catalysis," *Adv. Catal.*, vol. 6, no. C, pp. 143–196, 1954, doi: 10.1016/S0360-0564(08)60390-9.
- [34] I. C. Yates and C. N. Satterfield, "Intrinsic Kinetics of the Fischer-Tropsch Synthesis on a Cobalt Catalyst," *Energy and Fuels*, vol. 5, no. 1, pp. 168–173, 1991, doi: 10.1021/ef00025a029.
- [35] Y. N. Wang, Y. Y. Xu, H. W. Xiang, Y. W. Li, and B. J. Zhang, "Modeling of catalyst pellets for Fischer-Tropsch synthesis," *Ind. Eng. Chem. Res.*, vol. 40, no. 20, pp. 4324–4335, 2001, doi: 10.1021/ie010080v.
- [36] D. Vervloet, F. Kapteijn, J. Nijenhuis, and J. R. Van Ommen, "Fischer-Tropsch reaction-diffusion in a cobalt catalyst particle: Aspects of activity and selectivity for a variable chain growth probability," *Catal. Sci. Technol.*, vol. 2, no. 6, pp. 1221–1233, 2012, doi: 10.1039/c2cy20060k.
- [37] D. E. Mears and M. Boudart, "The dehydrogenation of isopropanol on catalysts prepared by sodium borohydride reduction," *AIChE J.*, vol. 12, no. 2, pp. 313–321, 1966, doi: 10.1002/aic.690120220.
- [38] D. E. Mears, "Diagnostic criteria for heat transport limitations in fixed bed reactors," *J. Catal.*, vol. 20, no. 2, pp. 127–131, 1971, doi: 10.1016/0021-9517(71)90073-X.

Appendix

Calculations for mass and heat transfer internal and external constraints in FBR

Design: Eggshell Co-promoted Re-3D-Printed support $\alpha\text{-Al}_2\text{O}_3$

Test: Fixed bed reactor with ID: 9 mm and H_{bed} : 60 mm

Assumptions

internal

- First order reaction
- Eggshell pellets with a thin catalytic layer to neglect the internal diffusion effects
- Homogeneous temperature inside the pellets

external

- Appropriate velocity and particle diameter to enhance the external mass transfer
- External heat transfer limitation (fluid-solid) are small (uniform temperature gradient)

The modeled and tested temperatures are: 200 °C (473 K), 210 °C (483 K) and 220 °C (493 K).

Internal limitations criteria:

Diffusion limitation

$$C_{WP} = \frac{-r'_{CO(obs)} \cdot \rho_{Co} \cdot R^2}{D_{eff,CO} \cdot C_{CO}} \ll 1 \quad \text{Weisz-Prater criterion}$$

Effective diffusion coefficient:

$$D_{eff,CO} = D_{CO,WAX} \cdot \left(\frac{\varepsilon_{catalyst}}{\tau} \right) \quad D_{CO,WAX} = 5.584 e^{-7} * \exp\left(-\frac{1786.29}{T}\right)$$

Porosity of the catalyst:

- Volume of pores = 0.011 $\left[\frac{\text{cm}^3}{\text{g}}\right]$ (from BET measurement)
- Total volume = $\frac{1}{\rho_{Co}}$ $\rho_{Co} = 8.9 \left[\frac{\text{g}}{\text{cm}^3}\right]$ (crystal density of Co)
- $\varepsilon_{catalyst} = \frac{\text{Volume of pores}}{\text{Total volume}} = 0.1$

Tortuosity calculation with a correlation taken from Wijngaarden, R. J.; Kronberg, A.; Westerterp, K. R. *Industrial Catalysis: Optimizing Catalysts and Processes*; Wiley: New York, 1998; page 54-56.

Taking the value of porosity, we are in the **group D** of the following table so the value of the **exponential factor m** is **1.05**. The **tortuosity** is **4.2**.

$$\frac{\epsilon_p}{\gamma_p} = \frac{\epsilon_p^m}{(2 - \epsilon_p)^{m+1}}$$

Tortuosity

Porosity

Group	Recommended m	Range of m	Range of ϵ_p	Range of ϵ_p/γ_p
A	1.5	1.43-3.10	0.20-0.85	0.12-0.80
B	1	0.74-1.01	0.20-0.50	0.02-0.18
C	1.8	1.4-2.2	0.35-0.70	0.05-0.35
D	1.05	0.70-1.65	0.05-0.65	0.02-0.35

In the condition applied the diffusion coefficients are:

T (°C)	$D_{CO,WAX}$ (m ² /s)	Porosity/tortuosity	$D_{eff,CO}$ (m ² /s)
200	1.27887E-08	0.023923445	3.0595E-10
210	1.38288E-08	0.023923445	3.30832E-10
220	1.49061E-08	0.023923445	3.56605E-10

Characteristic length L_c :

R in the Weisz-Prater criterion represents the catalyst (pellet) sphere radius, but in this case, for the eggshell catalyst, it is a characteristic length L_c .

$$L_{cat} = \left(\frac{R}{3}\right) * \left[1 - \left(1 - \frac{\delta}{R}\right)\right]$$

δ = thickness of the catalytic layer (20 $\mu\text{m} \equiv 0.02 \text{ mm}$)

R = Radius of the spherical pellet (0.6 mm)

$$L_c = 1.93 \times 10^{-5}$$

Concentration of CO:

It is calculated with the ideal gas equation, considering the T and P conditions, and the mol fraction of CO in the syngas.

P (bar)	T (°C)	Fraction 1.7 H ₂ :1CO	C_{CO} (mol/m ³)
10	200	0.37037037	95.5
10	210	0.37037037	91.6
20	220	0.37037037	187.0

Reaction rate of CO:

It is obtained from the experimental data. Each value is calculated as an average of the 5 last concentrations taken from the chromatography analyses.

P (bar)	T (°C)	GHSV (NmL/h gcat)	r _{CO} (mol/s g _{cat})
10	200	1320	1.90E-06
10	210	1320	2.37E-06
20	220	993	1.44E-06

Criterion calculation:

P (bar)	T (°C)	GHSV (NmL/h gcat)	C _{wp}
10	200	1320	0.194
10	220	1320	0.233
20	210	993	0.064

Heat transfer limitation

$$\gamma \cdot \beta_i \cdot C_{WP} = \left(\frac{E_A}{RT} \right) \cdot \left(\frac{(-\Delta H_r) \cdot D_{eff,CO} \cdot C_{CO}}{\lambda_{cat,eff} \cdot T} \right) \cdot \left(\frac{R_{CO} \cdot \rho_{CO} \cdot L_{cat}^2}{D_{eff,CO} \cdot C_{CO}} \right) < 0.015$$

- $E_A = 100 \left[\frac{kJ}{mol} \right]$
- $\Delta H_r(FT_{synthesis}) = -165 \left[\frac{kJ}{mol} \right]$

Effective thermal conductivity:

$$\lambda_{cat,eff}(T) = \varepsilon_{bed} \cdot \lambda_{syngas} + (1 - \varepsilon_{bed}) \cdot \lambda_{AL_2O_3}(T)$$

- λ_{syngas} (63% H₂, 36% CO) = 0.087 $\left[\frac{W}{m \cdot K} \right]$
- $\lambda_{AL_2O_3}(T)$ calculated experimentally

P (bar)	T (°C)	GHSV (NmL/h gcat)	C _{wp}	γ	β	$\gamma \cdot \beta \cdot C_{wp}$
10	200	1320	0.194	25.429	6.29E-10	3.11E-09
10	220	1320	0.233	24.397	6.63E-10	3.77E-09
20	210	993	0.064	24.902	1.45E-09	2.32E-09

External limitations criteria:

Diffusion limitations

$$MR_{diff} = \frac{-r'_A(obs) \cdot \rho_b \cdot L_{cat}}{k_c \cdot C_{CO}} < 0.15 \quad \text{Mears criterion (diffusion)}$$

- $\rho_{Al_2O_3} = 3.1 \left[\frac{g}{cm^3} \right]$ (experimental)
- Bulk density of the bed: $\rho_b = (1 - \varepsilon_{bed}) \cdot \rho_{Al_2O_3} = 2.17 * 10^6 \left[\frac{g}{cm^3} \right]$
- $\varepsilon_{bed} = 0.32$

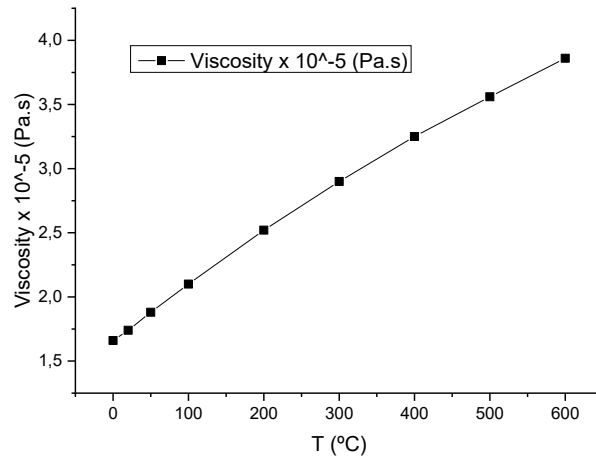
Mass transfer coefficient:

$$k_c = \left[\frac{U \cdot d_p \cdot \rho_b}{\mu_{CO} \cdot (1 - \varepsilon_{bed})} \right]^{\frac{1}{2}} \cdot \left[\frac{\mu_{CO}}{\rho_{fluid} \cdot D_{H_2-CO}} \right]^{\frac{1}{3}} \cdot \left[\frac{D_{H_2-CO} \cdot (1 - \varepsilon_{bed})}{d_p \cdot \varepsilon_{bed}} \right]$$

- Particle diameter: $d_p = 1.2 \text{ mm}$
- Superficial gas velocity through the bed: $U = \frac{V_o}{A_c} \left[\frac{m}{s} \right]$
- Cross-sectional area: $A_c = \pi \cdot \left(\frac{ID^2}{4} \right)$ $ID = 0.0009 \text{ [m]}$

P (bar)	T (°C)	GHSV (NmL/h g _{cat})	Vo (m ³ /s)	U (m/s)
10	200	1320	1.1959E-07	1.88E-03
10	210	1320	1.24647E-07	1.96E-03
20	220	993	4.55469E-08	7.16E-04

- Density of the fluid: $\rho_{fluid} = \frac{(n_{CO} \cdot MM_{CO} + n_{H_2} \cdot MM_{H_2}) \cdot P}{(n_{CO} + n_{H_2}) \cdot RT}$
- Diffusion coefficient H₂-CO: $D_{H_2-CO} = D_0 \cdot \left(\frac{T}{T_0} \right)^\alpha \cdot \left(\frac{P_0}{P} \right) \left[\frac{cm^2}{s} \right]$
- $\alpha = 1.75$ $D_0(1 \text{ atm}, 273 \text{ K}) = 0.651 \left[\frac{cm^2}{s} \right]$
- Viscosity of CO μ_{CO} : Engineering ToolBox, (2014). *Gases - Dynamic Viscosity* (https://www.engineeringtoolbox.com/gases-absolute-dynamic-viscosity-d_1888.html)



P (bar)	T (°C)	D_{H_2-CO} (m ² /s)	ρ_{fluid} (kg/m ³)	$\mu_{CO} \times 10^{-5}$ (kg/m s)	Kc (m/s)
10	200	1.70E-05	3.00	2.52	2.83E-03
10	210	1.83E-05	2.88	2.70	2.50E-03
20	220	8.83E-06	5.87	2.55	1.06E-03

P (bar)	T (°C)	GHSV (NmL/h g _{cat})	MR _{diff}
10	200	1320	1.09E-02
10	210	1320	1.35E-02
20	220	993	9.47E-03

Heat transfer limitations:

$$MR_{heat} = \left| \frac{\Delta H_r \cdot (-r_{CO}(obs)) \cdot \rho_b \cdot L_{cat} \cdot E_A}{h \cdot T^2 \cdot R_g} \right| < 0.15 \quad \text{Mears criterion (heat transfer)}$$

- R_g = gas constant
- T = operating temperature

Heat transfer coefficient h:

- $\rho_{liq} = 700 \left[\frac{kg}{m^3} \right]$
- $v_{liq} = 0.02 \left[\frac{m}{s} \right]$
- $d_{cat} = 0.0012 [m]$
- $\mu_{liq} = 2.5 \cdot 10^{-3} \left[\frac{kg}{m \cdot s} \right]$
- $c_{p,liq} = 2.2 \left[\frac{kJ}{kg \cdot K} \right]$
- $\lambda_{liq} = 0.15 \left[\frac{W}{m \cdot K} \right]$

$$Re = \frac{\rho_{liq} \cdot d_{cat} \cdot v_{liq}}{\mu_{liq}} = 2.41 \cdot 10^{-1}$$

$$Pr = \frac{c_{p,liq} \cdot \mu_{liq}}{\lambda_{liq}} = 3.92 \cdot 10^1$$

Nusselt correlation:

$$Nu = 1.31 \cdot Re^{\frac{1}{3}} \cdot \frac{Pr^{\frac{1}{3}}}{\varepsilon_{bed}} = 9.23$$

$$Nu = h \cdot \frac{L_{cat}}{\lambda_{liq}} \rightarrow h = 1.077 \left[\frac{kW}{m^2 \cdot K} \right]$$

P (bar)	T (°C)	MR _{heat}
10	200	2.04E-02
10	210	2.34E-02
20	220	1.48E-02

Acknowledgements

Vorrei ringraziare tutto il gruppo di persone conosciute durante lo sviluppo di questo lavoro presso l'istituto di ricerca ed energia IREC in Catalonia, Barcellona. In particolare ringrazio i miei supervisori Julià Puzkiel e Marc Nuñez Eroles che mi hanno supportato durante il lavoro, prontamente risolto ogni mio dubbio e favorito la mia crescita professionale. Ringrazio altresì il mio relatore, professor Federico Smeacetto, che mi ha dato questa splendida opportunità. Ringrazio tutti gli amici conosciuti a Torino e Barcellona con i quali ho condiviso dei momenti stupendi. Un ringraziamento speciale va al mio collega, coinquilino, amico, fratello Roberto con il quale ho condiviso questi 5 anni di studi, superato ogni difficoltà e senza il quale ora non sarei qui a scrivere queste parole. Ringrazio infine la mia famiglia che mi ha permesso di affrontare questa avventura all'età di 18 anni lasciando la mia cara e amata terra, la Sicilia. Li ringrazio per aver supportato ogni mia scelta senza avermi mai vietato niente e incoraggiato sempre nei momenti più difficili. Spero che il futuro mi riservi un'avventura bella come questa, non dimenticherò mai ciò che il Politecnico di Torino mi ha dato.